UNIVERSITY OF CALIFORNIA,
IRVINE

Sensitive, multiplexed molecular profiling with nanomaterial probes for cancer diagnostics

DISSERTATION

submitted in partial satisfaction of the requirements
for the degree of

DOCTOR OF PHILOSOPHY

in Biomedical Engineering

by

Maha Karim Rahim

Dissertation Committee:
Assistant Professor Jered B. Haun, Chair
Professor Enrico Gratton
Associate Professor Jennifer A. Prescher

2017

DEDICATION

To

my parents for their unconditional support

TABLE OF CONTENTS

LIST OF FIGURES

LIST OF EQUATIONS

ACKNOWLEDGMENTS

I would like to express my deepest gratitude to my advisor and committee chair, Professor Jered Haun, for his continuous guidance and support. His encouragement and belief in my ability to succeed carried me through the trials and tribulations of graduate school.

I would like to thank my other committee members, Professors Enrico Grattion and Jennifer Prescher, for their expertise, enthusiasm, and insights on my project. I would like to thank all the Haun Lab members for their camaraderie and friendship over the years.

I would like to thank the post doctoral fellows, graduate students, and undergraduate students who collaborated on work presented in the following chapters: Dr. Rajesh Kota (Chapter 1 and 2), Tina Chu (Chapter 2), Jasmin Guerrero (Chapter 2), and Irma Fernandez (Chapter 2).

I also thank American Chemical Society for permission to include Chapter 2, which was originally published in Bioconjugate Chemistry in the following article:

Rahim, M.K., Kota, R., & Haun, J.B. Enhancing Reactivity for Bioorthogonal Pretargeting by Unmasking Antibody-Conjugated trans-Cyclooctenes. Bioconjugate Chem. 2015, 26(2), 352-360.

CURRICULUM VITAE

Maha Karim Rahim

Education

2017 PhD in Biomedical Engineering
University of California, Irvine

2014 M.S. in Biomedical Engineering
University of California, Irvine

2011 B.S. in Chemical Engineering
University of California, Los Angeles

Publications

1. **Rahim, M.K.**, Kota, R., & Haun, J.B. Enhancing Reactivity for Bioorthogonal Pretargeting by Unmasking Antibody-Conjugated *trans*-Cyclooctenes. *Bioconjugate Chem.* **2015**, *26(2)*, 352-360.

2. Wang, M., Ravindranath, S.R., **Rahim, M.K,,** Botvinik, E.L., & Haun, J.B. Evolution of Multivalent Nanoparticle Adhesion Dynamics via Specific Molecular Interactions. *Langmuir*, **2016**, *32(49)*, 13124-136.

3. McWhorter, F.Y., Smith, T.D., Luu, T.U., **Rahim, M.K.,** Haun, J.B. ,& Liu, W.F. Macrophage secretion heterogeneity in engineered microenvironments revealed using a microwell platform. *Integr. Biol*, **2016**, *8*, 751-760.

4. **Rahim, M.K.**, Kota, R., Lee, S., & Haun, J.B. Bioorthogonal Chemistries for Nanomaterial Conjugation and Targeting *Nanotechnology Reviews*. **2013**, *2(2)*, 215-227.

5. Lei, Y., **Rahim, M.**, Ng, Q. & Segura, T. Incorporation of Active DNA/PEI Polyplexes into Hyaluronic Acid and Fibrin Hydrogels Using Caged Nanoparticle Encapsulation, CnE. *Journal of Controlled Release*. **2011**, *153*, 255-261.

ABSTRACT OF THE DISSERTATION

Sensitive, multiplexed molecular profiling with nanomaterial probes for cancer diagnostics

By

Maha Karim Rahim

Doctor of Philosophy in Biomedical Engineering

University of California, Irvine, 2017

Assistant Professor Jered B. Haun, Chair

Cancer is complex and heterogeneous. Molecular profiling can richly characterize this tumor heterogeneity, uncovering diverse cell types and functional states for improved cancer diagnostics. In particular, extensive protein profiling can provide functional and spatial information, such as biomarker distribution, dynamic cell signaling pathways, and tissue morphology. Nanomaterial-based probes (NPs) are uniquely suited for molecular profiling applications due to their signal strength, narrow emission windows, and tunable fluorescence lifetime properties. The goal of this work is to develop a nanomaterial-based platform for molecular profiling that offers sensitive, multiplexed detection of functional molecules, while maintaining cellular resolution.

The ability to directly detect low-level expression biomarkers requires exquisitely sensitive molecular analysis. In order to achieve a high degree of sensitivity, we employ the rapid bioorthogonal reaction between *trans*-cyclooctene (TCO) and tetrazine (Tz). In this two-step procedure, TCO-modified antibodies bind to biomarker targets, followed by covalent attachment of numerous Tz-NPs, resulting in chemical amplification. Despite the improved sensitivity, we demonstrated that the majority of TCOs conjugated to antibodies

via standard amine-coupling are non-reactive, masked by hydrophobic interactions with the antibody. We engineered linkers that restore the reactivity of antibody-bound TCO by increasing solubility and physically preventing burying within the antibody. Consequently, these TCO-modified antibodies support a higher degree of chemical amplification, resulting in greater than 5-fold signal enhancement, which can facilitate direct detection of even low-level expression markers. We further optimized linkers to maximize reactivity of a wide range of bioorthogonal reactants after antibody bioconjugation.

In addition to improving detection sensitivity, we also explored the fluorescence lifetime properties of NPs. The phasor approach to fluorescent lifetime imaging (FLIM) utilizes a simple graphical representation to resolve distinct fluorescent lifetimes. Utilizing phasor analysis, we uncovered unique lifetime features of NPs that were leveraged for enhanced multiplexed detection. We performed FLIM and phasor analysis using four different fluorescent probes, which emit light within the same emission window but have unique fluorescent lifetimes, for simultaneous detection of functional molecules. The resulting phasor map displayed lifetimes corresponding to all four fluorescent probes, and can be readily resolved. Future work will focus on expanding this approach to other spectral windows.

Chapter 1

Introduction

1.1 Tumor heterogeneity

Tumors are complex and heterogeneous, with considerable variation not only between individuals, but also within the same tumor. This disease complexity drives tumor progression and influences clinical decisions. Intratumor heterogeneity arises from genetically distinct subclonal populations of tumor cells, as well as from phenotypic variation among subclones.[1] The genetic diversity in tumors likely follows a branching evolution, where multiple clones with unique driver mutations coexist.[2] Each subclone has distinctive progression trajectories and therapeutic response,[3] and therefore this genetic heterogeneity is clinically consequential. Functional heterogeneity within subclones may be attributed to the presence of rare subpopulations of cancer stem cells that drive tumor growth and progression through epigenetic changes.[4,5] Intratumor heterogeneity extends even beyond the tumor cells. A diverse ecosystem of cell types dynamically interacts with the tumor and contributes to the overall diseased state.[6–9] For example, infiltrating immune cells and their paracrine signaling are instrumental in promoting tumor growth.[10–12] There is also rich research revealing the prominent role of stroma in metastasis.[13–15] Owing to the significance of this cellular heterogeneity within tumors, analyzing this diversity will be important for clinical diagnostics.

1.2 Molecular profiling of cancer

Molecular information aids the fundamental understanding of tumor biology and elucidates complex differences that occur in diseased states. It can expose the different cell types that compose a heterogeneous tissue and uncover dynamic signaling pathways that

drive specific cellular functions. Knowledge of the molecular mechanisms that drive diseased states can be leveraged for improved patient care.

Molecular profiling of cancer could enable earlier diagnoses, more accurate prognoses, and identification of patient-specific treatments. To date, clinical molecular diagnostics and treatment focuses on identifying key drivers of tumor growth and then directly targeting these pathways.[16–19] While clinically beneficial, this approach does not account for the profound impact of tumor heterogeneity. For example, classical subdivisions of breast cancer based on hormone receptor and HER2 expression were further classified based on gene expression profiles with clinical value.[20] Even the extent of heterogeneity itself can be used as a clue into the tumor state.[21,22] Thus, diagnostic technologies capable of distinguishing key molecular drivers within cellular subpopulations of the tumor will be incredibly impactful.

1.3 Molecular profiling technologies

Within a clinical setting, histological analysis is currently the primary diagnostic resource. Histology relies on morphological features that are a proxy for proliferation and differentiation to grade malignancy.[23] It utilizes a majority of the biopsied tissue, providing some tissue context and spatial information, but is not coupled with any information of the molecular basis of the cancer. Immunohistochemistry (IHC) and fluorescence in situ hybridization (FISH) provide some molecular analysis. These techniques also keep tissue intact; allowing spatial and cellular information to be retrieved. Unfortunately, these techniques have limited multiplexing capacity; they frequently characterize only 2-3 biomarkers in practice.[24] This is insufficient for the desired detailed molecular profiling of tumors necessary to examine heterogeneity.

Gene expression profiling technologies have advanced tremendously in recent decades to meet the demands of molecular diagnostics. These technologies, such as microarray and next generation gene sequencing, provide an unprecedented level of molecular detail from biological samples. In microarray technology, an array of DNA copies, which correspond to large library of mRNA, are immobilized onto a solid surface. Fluorescent-labeled targets from biological samples can hybridize with the immobilized fragments, producing signal corresponding to mRNA levels of genes. In this manner, thousands of genes can be examined at once. The most popular use of this technology is to uncover gene expression profiles of cancer as an approach to molecularly characterize tumors.[25] Indeed, microarray analysis has been used to study a wide variety of cancers such as breast,[26,27] lung,[28] and colon cancers.[29] Comprehensive analysis of cancer genomes and transcriptomes can also be done in a high-throughput manner using next-generation gene sequencing technologies.[30] With these techniques, uncovering whole genomes is feasible, and has consequently led to improved tumor classification,[31] stratifying subgroups with different therapy response[32]. Combining data from multiple platforms enabled reclassification of tumors from 12 tissues-of-origin into 11 molecular subtypes, from convergence or further classification of initial groups.[33] However, these strategies require interrogation of a population of cells in bulk. Thus, they sacrifice spatial resolution and the ability to assess tumor heterogeneity. Tumor populations are reduced to averages. This makes it difficult to detect rare subpopulations of cancer cells driving growth.

To address the limitations of bulk sequencing, single cell genomics techniques are advancing rapidly. The feasibility of characterizing intratumor heterogeneity at the single cell level came to fruition with advancements in gene expression profiling that enabled

whole transcriptome analysis of single cells,[34–36] as well as single cell isolation techniques that permit thousands of cells to be sequenced rapidly.[37] These approaches have been powerful for dissecting the contribution of rare subpopulations to tumor evolution and metastasis.[38–43]

In addition to the insights gleaned from individual cells' role in overall tumor behavior, single cell analysis techniques also make it clear that tissue context is still very critical to understanding heterogeneity. The microenvironment influences cellular decisions; consequently, the pervasive information at the single cell level should be contextualized with spatial resolution.[44] Spatial information and phenotypic analysis can capture distinct neighborhoods of tumor and stromal cells in their microenvironment,[45,46] whose dynamic and reciprocal communication likely influence disease states. Moreover, it may also be more valuable to assess protein expression in their cellular context because some abnormal protein expression is only apparent after cell activation or as a part of a dynamic signaling pattern.[47]

In this vein, highly multiplexed tissue-based imaging techniques are interesting solutions that connect histopathological characteristics with extensive genotypic and phenotypic analysis. Traditional immunofluorescence achieves protein detection with nanometer resolution, and acquires cellular morphology and microenvironment features,[48,49] but this technique cannot fully characterize the complexity of the tumor due to multiplexing limitations. Minimizing spectral overlap of probes by utilizing narrow emission quantum dots in lieu of broader emission organic fluorophores can extend multiplexing capacity to 5 colors simultaneously.[50,51] Hyperspectral fluorescence imaging can further extend multi-color tissue analysis,[52] although gains in multiplicity typically

come with the trade-off of reduced dynamic range.[44] To mitigate this challenge, cyclic immunofluorescence undergoes several rounds of staining followed by deactivation,[24,53,54], but tissue is subject to epitope degradation with each cycle. Multiplex ion beam imaging (MIBI)[55] and imaging mass cytometry (IMC)[40] depart from fluorescence techniques and utilize mass spectrometry instead; the detection of metal isotopes facilitates resolution of over 32 species with impressive dynamic range. Despite these advanced techniques, there are no tissue imaging strategies that offer high multiplicity without the requirement of expensive instrumentation or large time costs.

1.4 Fluorescence lifetime imaging microscopy

Fluorescence lifetime (τ) refers to the duration following excitation of fluorescence light emission to decay to $1/e$ of the initial intensity. Thus, a monoexponential fluorescence decay profile can be described as follows:

$$I(t) = I_0 e^{-\frac{t}{\tau}} \quad (1)$$

where I_0 is the intensity at time zero.[56] If the decay is multiexponential, or there are multiple fluorescent species present, the fluorescence decay profile can be described as follows:

$$I(t) = \sum_{i=1}^{N} C_i e^{-\frac{t}{\tau_i}} \quad (2)$$

where N is the number of components and C_i is the pre-exponential amplitude. If fluorescent species have sufficiently distinct fluorescent lifetimes, this property can be leveraged to resolve fluorescent probes not only spectrally, but based on their lifetimes as well. Essentially, time-resolved fluorescence would enable probes within the same spectral window to be distinguished, dimensionally increasing the multiplexing capacity of

fluorescence imaging. In fact, several studies have shown that two species can be resolved in this manner.[57,58]

There are several approaches to measuring the fluorescence lifetime of a sample. In the time domain, popularly employed using time-correlated single-photon counting (TCSPC), a short pulse of light illuminates the fluorophores and a histogram of the delayed emission photons is collected over time.[59] The adaptation of this technique for laser scanning microscopes[60] facilitated the translation of fluorescence lifetime imaging microscopy (FLIM) for many biological applications. However, single photon detection dictates the maximum counting rate and therefore limits acquisition speed for imaging.[56,61] In the classic analog frequency domain approach, sinusoidally modulated light excites the sample, and the corresponding fluorescence emission frequency is phase-delayed and amplitude-modulated. The phase shift and modulation ratio depend on the fluorescence lifetime and consequently can be utilized to recover intensity decay.[62] To provide the highest sensitivity to changes in lifetime, modulation frequencies, f, should match decay of fluorescent species as follows:

$$f = \frac{1}{2\pi\tau} \tag{3}$$

Digital frequency domain fluorescence lifetime (DFD-FLIM) advances on traditional analog frequency domain technique to minimize the modifications necessary to adapt lifetime imaging for commercial microscopes. Instead of a sinusoidal signal, DFD-FLIM employs the harmonic content from a fast repetition laser source.[63] The FLIMBox used in DFD-FLIM digitally modulates signal and generates phase bins for arriving photons, analogous to the time-binned photons collected in TCSPC. This approach efficiently collects photons, and therefore makes high-speed FLIM feasible.

Analyzing experimental fluorescence lifetime decays is inherently challenging. In fact, the difficulty associated with deconvolving fluorescence lifetime decay curves has limited the widespread use of FLIM. Nonlinear iterative fitting methods, such as the method of least squares[64] or Laplace transformation[65] can approximate exponential decay curves to the experimental data. However, resolving complex multiexponential decay curves in this manner requires a high number of detected photons to be able to measure the decay with accuracy. FLIM magnifies this challenge, since only a small number of photons per pixel are collected.[66] Moreover, goodness of fit measurements can be misleading; a two-component decay can be fit with 5-15 exponentials and conversely a complex set of exponentials can be explained by a simpler decay expression.[67] Alternative approaches such as stretched exponential function[68] and pattern-matching[69] tend to be computationally expensive.

The phasor approach to fluorescence lifetime imaging greatly simplifies lifetime analysis. Instead of fitting complicated exponential functions, the phasor approach transforms histograms of time delays at each image pixel.[66] These sine and cosine transforms are represented as the g and s coordinates of the polar plot, termed the phasor plot (Figure 1.1). This method of analysis is independent of the measurement technique used. In the case of FLIM measurements in the time domain, the corresponding g and s coordinates are given by:

$$g_{i,j}(\omega) = \frac{\int_0^\infty I_{i,j}(t)\cos(\omega t)dt}{\int_0^\infty I_{i,g}(t)dt} \tag{4}$$

$$s_{i,j}(\omega) = \frac{\int_0^\infty I_{i,j}(t)\sin(\omega t)dt}{\int_0^\infty I_{i,g}(t)dt} \tag{5}$$

where i and j refer to the pixel of an image and ω is to the laser repetition angular frequency. For FLIM measurements taken inthe frequency domain, the corresponding g and s coordinates are given by:

$$g_{i,j}(\omega) = m_{i,j} \cos \varphi_{i,j} \tag{6}$$

$$s_{i,j}(\omega) = m_{i,j} \sin \varphi_{i,j} \tag{7}$$

where $m_{i,j}$ and $\varphi_{i,j}$ refer to the modulation and phase shift of the emission with respect to the excitation.

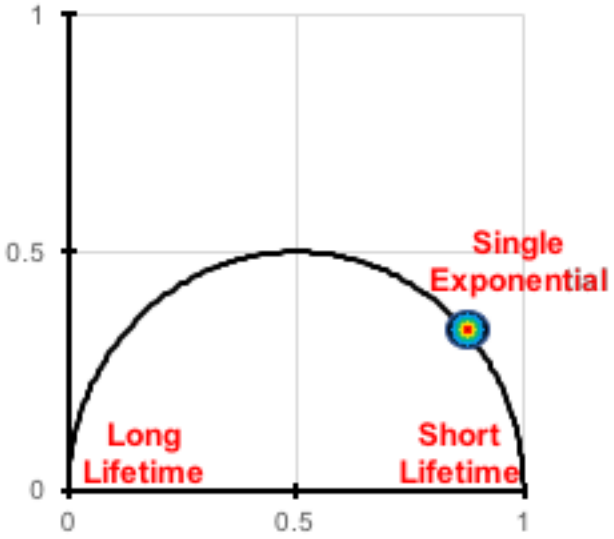

Figure 1.1 Phasor analysis of fluorescence lifetime. Schematic of the phasor diagram depicting location of cluster corresponds to lifetime decay curves. Longer lifetime values fall near coordinates (0,0), while shorter lifetime values fall near (1,0). Single exponential decay fall along the line of the universal circle, and more complex decays are located inside the circle.

With this phasor analysis approach, intricate decay curves are replaced with a simple graphical representation. Separate lifetimes are easily distinguished by the cluster of pixel values in distinct locations in the plot for each fluorescent species.[66,70] As depicted in Figure 1.1, the phasor location on the phasor plot correlates with magnitude of fluorescence lifetime, as well as complexity of the decay curves. Short lifetime values will

fall near the coordinates (1,0) of the plot, while long lifetime values will lie near (0,0). Thus, different fluorescent materials have a unique position on the phasor plot that can be easily resolved from others. In fact, using this approach, as many as 10 endogenous fluorescent species have been resolved (Figure 1.2A).[70] Every point in the phasor can also be mapped back to the corresponding pixel in the image. Thus, this analysis tool allows not only the identification of unique fluorescent species based on lifetime, but also couples spatial information by identifying the regions of the image with specific lifetime values (Figure 1.2B). Moreover, with knowledge of the relative brightness of the fluorescent species present, concentration can easily be extracted.[71] This phasor approach makes fluorescent lifetime analysis more approachable as a molecular diagnostic strategy.

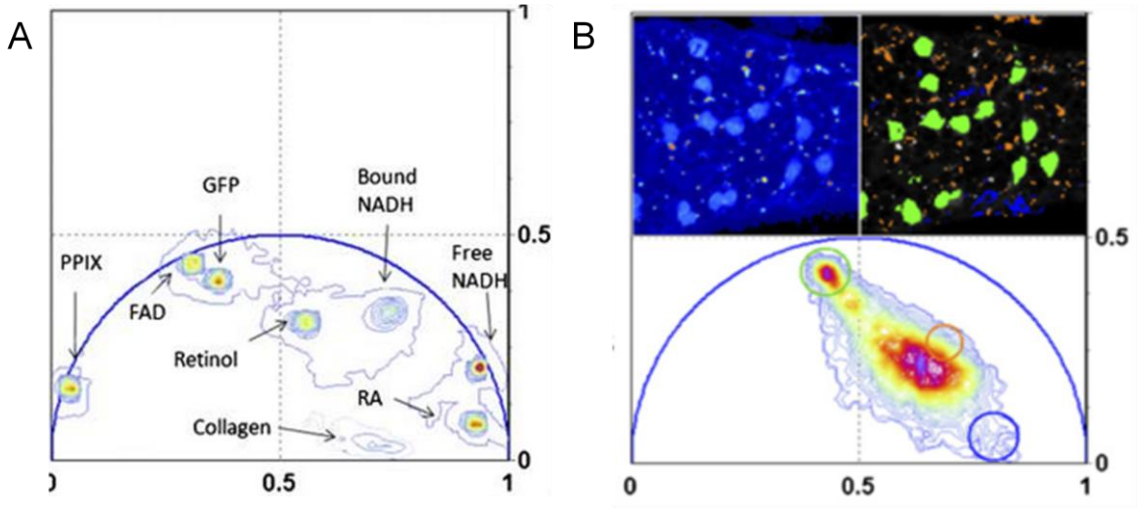

Figure 1.2 Phasor approach to FLIM identifies tissue components. (A) Phasor diagram depicting the unique location of the fluorescence lifetime for numerous endogenous fluorescent species. (B) Intensity image in upper left corner of GFP expressing cells, with its corresponding phasor plot below. The green cluster identified in the phasor plot is the lifetime location of GFP. The phasor color map (upper right corner) paints pixels with GFP lifetime value in green, revealing the GFP expressing cells and demonstrating reciprocal nature of phasor approach to FLIM. Reproduced from [70].

The phasor approach to FLIM follows simple vector addition. If two fluorescent species coexist in a single pixel, the phasor location will fall along the straight line whose endpoints are the locations of the two pure species. The exact location along the line depends on the intensity-weighted fraction of each species present in the pixel. Similarly, if a pixel contains three fluorescent species, the phasor location will fall within the triangle whose vertices are the phasor locations of the three pure species (Figure 1.3) This simple geometry facilitates quantitative analysis of several fluorescent species.

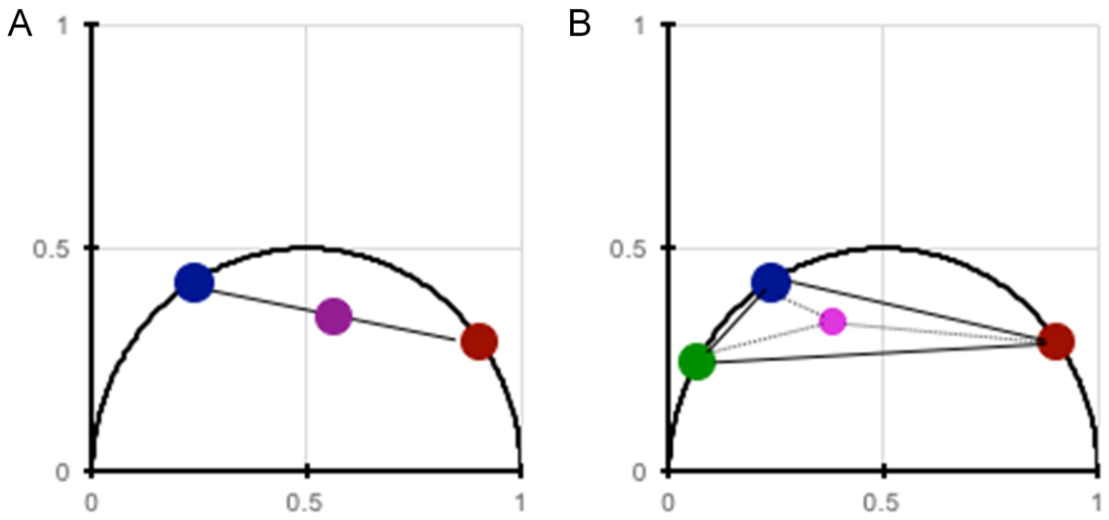

Figure 1.3 Multi-component analysis using the phasor approach to FLIM. (A) If a pixel contains a mixture of two fluorescent species, the phasor location will fall along the line that joins the phasor location of the two pure species. (B) If a pixel contains a mixture of three fluorescent species, the phasor location will fall within the triangle, whose vertices are the phasor locations of the three pure species.

1.5 Nanomaterial probes

With the phasor approach to FLIM, the parallel detection of many targets for meaningful molecular profiling is possible. However, fluorescent probes must be well-separated in phasor space to successfully use this approach. Most molecular fluorophores exhibit fluorescence lifetimes on the order of a few nanoseconds.[50] These relatively short

lifetimes are sufficient for the temporal resolution of two fluorophores,[72,73] however are too short for the discrimination of several fluorophores simultaneously present, without utilizing additional fluorescent properties.[69] Nanomaterial-based probes are an attractive alternative based on their unique features. For example, semi-conductor quantum dots have lifetime decays on the order of tens of nanoseconds.[58] Prior to the development of the phasor analysis technique, the multiexponential decay behavior of quantum dot lifetimes made temporal separation challenging.[74] However, in phasor space, these long lifetime values can be easily distinguished from shorter lifetime species. Additionally, the long lifetime of quantum dots can be readily separated from cellular autofluorescence, potentially enhancing detection sensitivity.[50] Thus, their use as probes for molecular profiling could enhance the power of lifetime-based multiplexing.

Nanomaterial probes have several other advantageous features that uniquely qualify them for highly multiplexed molecular profiling. Nanomaterials are extremely bright, exhibiting high molar absorption coefficients, and photostable;[75] both these attributes are critical for accurate quantitative signal analysis in molecular imaging. Moreover, because material composition, size, and shape influence their optical properties, nanomaterial probes are also exceptionally tunable.[76,77] Owing to these attractive qualities, quantum dots have been successfully employed for biological staining,[75,78,79] including spectral multiplexing techniques.[24,80–82] Harnessing their tunable lifetime properties will build on their successful achievements in multiplexed molecular profiling.

1.6 Bioorthogonal chemistries for nanoparticles

Biomolecules can be conjugated to the surface of nanomaterial probes to impart efficient and multivalent adhesion for molecular targets. Traditional bioconjugate

chemistries used for fluorophore-antibody conjugation, such as carbodiimide crosslinking, are not ideal for nanoparticle bioconjugation. They lead to low coupling efficiencies and lack controlled display of biomolecules.[83,84] To maximally exploit the potential of nanomaterials for diagnostics, bioorthogonal chemistries have been translated for bioconjugation strategies. This class of reactions is fast, has a small footprint, and is suitable for complex biological environments. It has been shown that employing bioorthogonal chemistries for nanoparticle bioconjugation improves avidity relative to traditional techniques, which directly increases binding efficiency to molecular targets.[84] More recently, the rapid bioorthogonal cycloaddition between *trans*-cyclooctene (TCO) and tetrazine (Tz) was adapted to create antibody-nanoparticle direct conjugates for *in situ* molecular targeting.[85,86] Importantly, this catalyst-free bioorthogonal chemistry mitigates the irreversible fluorescence quenching accompanying copper-catalyzed chemistries.[87] The fast reaction speed between TCO and Tz also supports *in situ* signal amplification. For example antibodies modified with TCO were pretargeted to biomarkers on live cells followed by subsequent attachment of numerous Tz-modified nanoparticles (Figure 1.4).

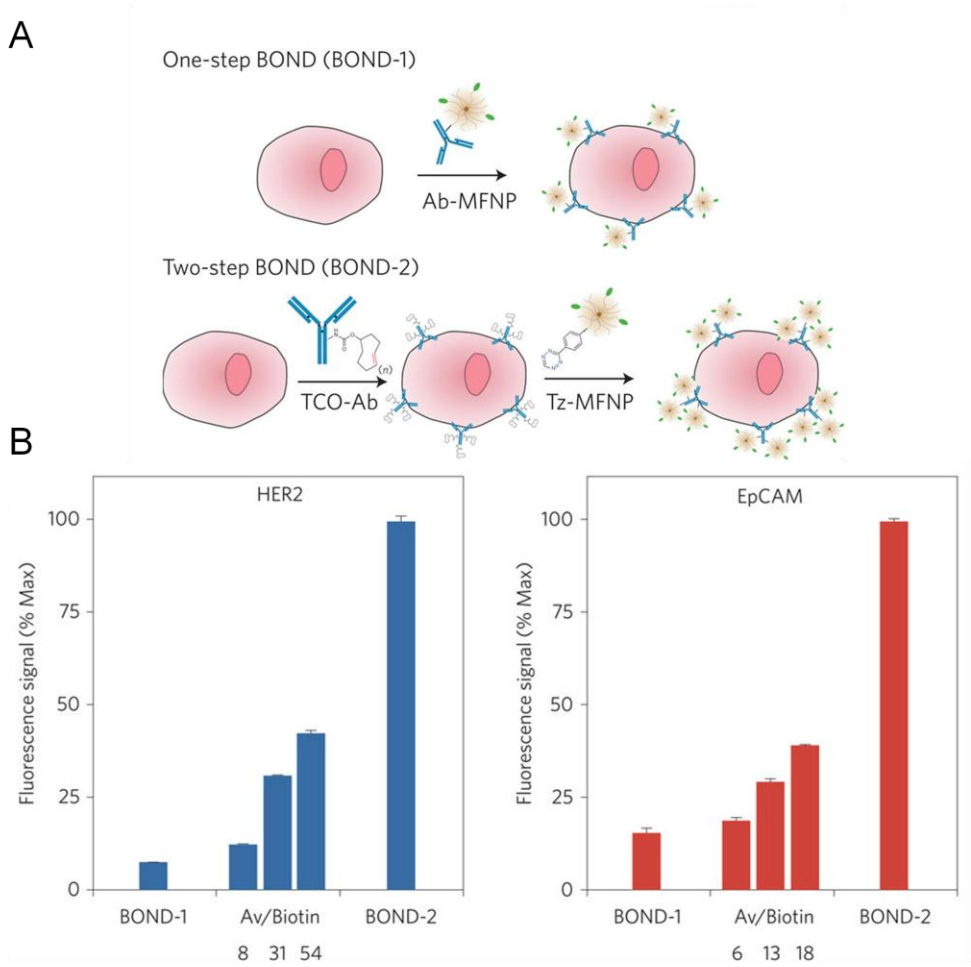

Figure 1.4 Overview of two-step nanoparticle detection strategy. (A) A biomarker of interest is targeted a monoclonal antibody modified with a nanoparticle (BOND-1), or with TCO (BOND-2). In BOND-2, multiple Tz-modified nanoparticles are then coupled to TCO-modified antibodies for amplified nanoparticle binding. (B) Fluorescence intensity of labeled cells has the highest signal using BOND-2 compared to avidin/biotin two-step labeling and BOND-1. Reproduced from [85].

In this two-step approach, greater than 10-fold signal enhancement is feasible. This bioorthoognal chemistry-based amplification strategy is even superior to avidin-biotin amplification, owing to the small size and high valency of the bioorthogonal reactants.[85] Despite the power of this technique, further improvements are desired to detect relevant low-expression level protein biomarkers.

1.7 Overview of dissertation research

The goal of this study was to develop novel approaches to amplify and multiplex the signal from nanomaterial probes for molecular profiling technologies suitable for characterizing heterogeneous tumors. To achieve these goals, novel bioorthoognal linkers were engineered that support a high degree of nanoparticles for increasingly sensitive molecular detection of tumor cells. These linkers were further optimized to maximize reactivity after bioconjugation for a wide range of bioorthogonal reactants. In an effort to expand multiplexing capabilities of fluorescence imaging, the lifetime properties of nanomaterial probes during molecular targeting were studied. The unique features uncovered in this work informed the development of a lifetime-based multiplexed detection strategy. Utilizing the phasor approach to FLIM, parallel detection of three spectrally-matched fluorescent probes was resolved on live cells utilizing only temporal information. This detection platform dimensionally increases the multiplexing capabilities of fluorescence imaging, while maintaining morphological features and spatial information that are critical in cancer diagnostics.

Chapter 2

Unmasking antibody-conjugated *trans*-cyclooctenes to enhance reactivity for bioorthogonal pretargeting applications

2.1 Introduction

There is currently strong interest in utilizing bioorthogonal chemistries to augment the detection of diseases both inside and outside of the body.[88–91] These works utilize the concept of pretargeting, where a chemically tagged affinity molecule such as a monoclonal antibody is first applied to mark the target site, followed by covalent attachment of the contrast agent.[92,93] Due to poor *in vivo* pharmacokinetics or other limitations of a traditional direct conjugates, pretargeting has been shown to improve imaging capabilities under different modalities in animal models.[94–99] Moreover, the small size of bioorthogonal reactants enable antibodies to act as scaffolds for the attachment of numerous nanomaterial probes to cells and microvesicles, leading to dramatic signal amplification for *in vitro* cultures and *ex vivo* human clinical specimens.[85,86,100–104]

Bioorthogonal pretargeting applications have predominantly employed the catalyst-free inverse-electron-demand Diels–Alder cycloaddition between 1,2,4,5-tetrazine and *trans*-cyclooctene (TCO) due to its high selectivity and unprecedented speed.[105,106] Specifically, the reaction between tetrazine/TCO is several orders of magnitude faster than tetrazine with other dienophiles such as norbornene and methyl-cyclopropene or alternative catalyst-free chemistries such as the strain-promoted azide/cyclooctyne reaction.[89,107–109] The rapid kinetics is critical to success in pretargeting scenarios. The hydrophobic TCO is typically attached to monoclonal antibodies via standard amine-reaction to lysine residues, and TCO decorated antibodies have been shown to retain

aqueous stability and binding affinity even at high modification levels.[85,86,95,96,106] However, there is a large discrepancy in the literature with respect to the number of TCO attachments that can be obtained, and results diverge depending on the method of analysis. Specifically, total TCO conjugations measured by mass spectrometry have been reported to be as high as 10–20,[85,100] whereas functional TCOs assessed by tetrazine reaction have been usually fewer than 6.[95,96,106] A potential explanation for these results is that a significant proportion of TCO attachments have been rendered nonreactive. Several mechanisms could be involved with TCO inactivation, including (1) conversion of TCO to the *cis* isoform that is orders of magnitude less reactive with tetrazine, (2) steric hindrance of the bulky cycloaddition reaction near the antibody surface, and (3) interaction of the hydrophobic TCO with external or even internal domains of the antibody. *Trans*–*cis* isomerizaton has been shown to occur on the order of hours in the presence of catalysts such as free thiols or transition metals bound to serum proteins *in vivo*,[108–110] although neither of these routes is expected for antibody conjugates directly after preparation. The tetrazine/TCO cycloaddition reaction results in a large, bulky dihydropyrazine product that could be sterically hindered by the antibody surface. Steric effects have been noted to reduce the reaction rate of TCO with tetrazines containing bulky substituents, such as a *tert*-butyl group, and these effects were not observed for smaller cyclopropenes.[111] Finally, the hydrophobic TCO may simply bury within interior domains of the antibody to avoid the aqueous solvent. Further investigation into these potential inactivation mechanisms and overall TCO reactivity after attachment to monoclonal antibodies is needed to ensure that the remarkable speed and power of the tetrazine/TCO cycloaddition reaction translate to applications employing complex biomolecules. Placing the less hydrophobic tetrazine on

the antibody could potentially alleviate some of these issues, but stability of TCO-modified secondary agents could be a major challenge, particularly for nanoparticles. We believe the focus should instead be on retaining TCO reactivity following bioconjugation, thereby maximizing the power of bioorthogonal pretargeting applications such as *in vivo* imaging and *ex vivo* nanoparticle amplification for cellular diagnostics.

A simple and straightforward strategy to increase TCO solubility and physically prevent interactions with the antibody is to append TCO via a hydrophilic polymer linker. Poly(ethylene glycol) (PEG) has a long history of use with antibodies for reducing immunogenicity and improving pharmacokinetics.[112] Furthermore, it is well-known that PEG can improve the solubility of hydrophobic molecules such as drugs, fluorophores, and biotin. For the hydrophobic fluorophore indocyanine green (ICG), short PEG linkers have been shown to reduce aggregation of antibody conjugates and prevent ICG quenching by aromatic amino acids.[113,114] Finally, it was recently demonstrated that attaching TCO via a PEG linker increased the rate of *trans–cis* isomerization in serum, presumably by making the TCO more accessible to protein-bound transition metals that can catalyze the conversion.[110] The PEG linker did not affect the reaction rate with tetrazine; however, the number of reactive TCOs attached to the antibody was not characterized. Thus, the activity of bioorthogonal reactants immediately after antibody conjugation has not been investigated to date. A potential drawback is that PEG linkers can block antibody binding, although this appears to be less of an issue for shorter PEGs less than 1000 Da.[115,116]

Herein, we characterize TCO reactivity on the surface of different monoclonal antibodies following standard amine-conjugation procedures. Surprisingly, we find that up to 90% of antibody-associated TCOs are nonfunctional. We present evidence that suggests

TCOs are neither inactivated by *trans–cis* isomerization nor sterically hindered from cycloaddition reaction near the antibody surface; thus, we believe that inactive TCOs are masked by interactions with the antibody. Most importantly, we successfully restore reactivity by appending TCO using both short and long hydrophilic PEG linkers. We attach the PEG–TCO linkers via bioorthogonal reaction between azide and dibenzylcyclooctyne (DBCO), which is mutually orthogonal to the tetrazine/TCO chemistry.[117]

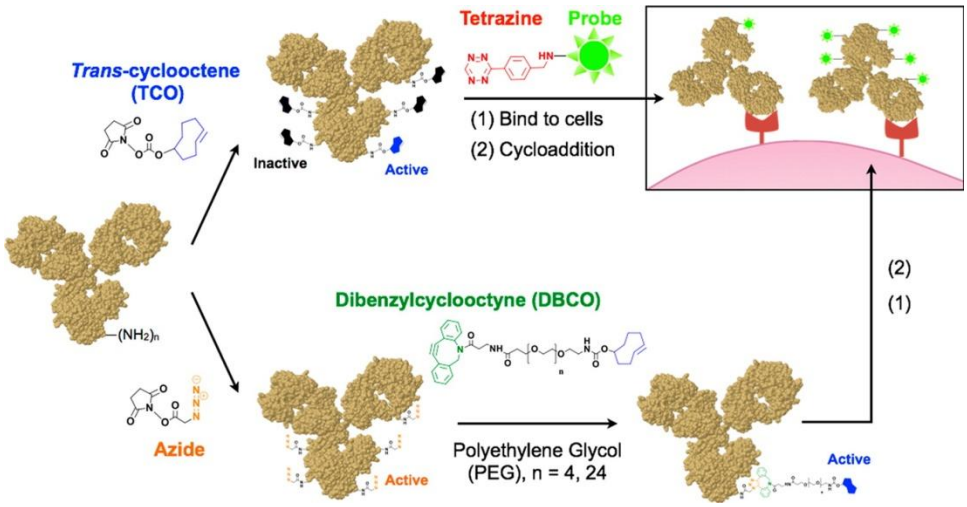

Figure 2.1. Schematic of dual, bioorthogonal antibody modification. Direct conjugation of TCO to antibodies via standard amine-reaction results in both active (blue) and inactive (black) moieties. We report that hydrophilic PEG linkers can fully preserve TCO reactivity. TCO–PEGs were introduced by initially modifying the antibody with azides followed by reaction with heterobifunctional DBCO–PEG*n*–TCO (*n* = 4 or 24). The improved reactivity obtained with the PEG linker will directly enhance binding of tetrazine-modified probes.

This novel dual bioorthogonal approach involves first decorating the antibody with varying amounts of azide followed by cycloaddition reaction with heterobifunctional DBCO–PEG–TCO molecules (Figure 2.1). Overall improvements in functional TCO density are more than 10-fold in total and 5-fold without significant loss of antibody binding activity. Enhanced detection signals are also demonstrated for tetrazine-modified fluorophores and quantum dots (QD) using flow cytometry and confocal imaging. This work should significantly expand the power of bioorthogonal pretargeting applications

such as *in vivo* molecular imaging and cell-based diagnostics utilizing chemical amplification of nanoparticle binding.

2.2 Methods

2.2.1 Synthesis of DBCO–PEG–TCO linkers

Heterobifunctional DBCO–PEG$_n$–TCO linkers were synthesized from a carboxylic acid–PEG$_n$–amine (Thermo Fisher Scientific): 100 mg of carboxylic acid–PEG$_n$–amine reacted with 2 equivalents of TCO–NHS (synthesized as previously reported[106,107]) in 2 mL of DCM containing 1.5 equivalents of triethylamine for 16 hours on ice. This reaction mixture was purified using silica column chromatography with a DCM/methanol gradient. The product reacted with *N*,*N*′-disuccinimidyl carbonate in triethylamine overnight to form NHS–PEG$_n$–TCO. After evaporation, DBCO was coupled by reacting NHS–PEG$_n$–TCO with 1.5 equivalents of amine-DBCO (Click Chemistry Tools) in 2 mL DCM containing 1.5 equivalents of triethylamine overnight. The final DBCO–PEG$_n$–TCO was purified using silica column chromatography with a DCM/methanol gradient for the PEG$_4$ linker, or using Sephedex G-10 desalting media (GE Healthcare) for the PEG$_{24}$ linker. DBCO–PEG$_4$–TCO was verified by proton NMR. Both linkers where characterized by HR MS with ESI-LC-TOF. Purified product was dissolved in methanol and loaded into a Waters LCT Premier system and analyzed by Waters MassLynx (Version 4.0).

2.2.2 Anti-EGFR antibody production from hybridomas

Monoclonal mouse antibody specific for human EGFR (IgG2$_a$, clone Mab 108) was produced from hybridoma HB-9764 obtained from ATCC. Hybridoma cells were grown in RPMI media containing 10% fetal bovine serum, 5% penicillin/streptomycin, 5% L-

glutamine, and 1% sodium pyruvate and subcultured by dilution of the non-adherent cells. For antibody production, 500 mL hybridoma cell cultures were grown for 7 days from an initial seeding density of 5 × 10^5cells/mL. The media was collected, centrifuged at 3000*g* for 10 min to remove cell debris, concentrated, buffer-exchanged into PBS using a Labscale tangential flow filtration system fitted with a Pellicon XL cassette (both from Millipore), and purified using a HiTrap Protein G column (GE Healthcare).

2.2.3 Antibody modifications

Anti-EGFR, anti-EpCAM ($IgG2_b$, clone 158206, R&D Systems), anti-TfR (IgG1, clone 29806, R&D Systems), and nonbinding control antibodies (mouse IgG1, clone MOPC-21, Biolegend) were buffer-exchanged into PBS using Zeba spin desalting columns (Thermo Fisher Scientific) prior to modification. Direct TCO conjugates was prepared by reacting 200 μg of antibody with 10, 100, or 1000 equivalents of NHS–TCO in 0.2 mL PBS containing 10% DMF and 0.1 M $NaHCO_3$ (pH 8.5) for 3 hours at room temperature. Azide and Oregon Green 488A conjugates were prepared in a similar manner using 10, 30, or 100 equivalents of NHS-azide (Thermo Fisher Scientific) or 10 equivalents of NHS–Oregon Green 488 (Thermo Fisher Scientific), with DMF omitted from the solvent. To study the effect of DMF on total TCO conjugation, direct TCO conjugates were also prepared in PBS containing <1% or <5% DMF for reaction with 100 or 1000 equivalents of NHS–TCO, respectively. TCO, azide, and Oregon Green 488-modified antibodies were purified using Zeba spin desalting columns. PEG–TCO conjugates were prepared by reacting the different azide-modified antibodies with DBCO–PEG–TCO molecules containing 4 or 24 PEG subunits. Reactions were carried out using 10-fold excess relative to the number of azide moieties for 4 hours at room temperature. TCO–PEG–antibodies were purified into PBS using Amicon Ultra-4

centrifugal filtration systems (Millipore). Antibody concentration was determined by absorption measurement recorded on a Thermo Scientific NanoDrop 2000 spectrophotometer. Oregon Green 488 density was also measured by absorption to be 2 dyes/antibody.

2.2.4 Cell culture

Human epidermoid cancer cell line A431 and hybridoma HB-9764 producing mouse anti-human EGFR antibody clone MAb108 were obtained from ATCC. A431 cells were selected for antibody labeling studies due to high-level expression of EGFR and EpCAM biomarkers as well as moderate expression of TfR. Cells were cultured in flasks at 37 °C with 5% CO_2. A431 cells were grown in DMEM media containing 10% fetal bovine serum, 5% penicillin/streptomycin, and 5% L-glutamine and subcultured after reaching confluence by treatment with trypsin–EDTA.

2.2.5 MALDI-TOF analysis of modified antibodies

Total TCO and azide densities were determined based on changes in mass using matrix-assisted laser desorption/ionization time-of-flight, MALDI-TOF, mass spectrometry. The matrix was prepared using 1 mg of sinapinic acid dissolved in 100 μL of 70:30 acetonitrile/water with 0.1% trifluororacetic acid. Unmodified control and TCO-, TCO-PEG-, and azide-modified antibodies were buffer-exchanged into water and concentrated to greater than 1 mg/mL using Amicon Ultra-4 centrifugal filters. Concentrated antibody solutions were combined with sinapinic acid matrix in a 2:1 ratio, and 1 μL of the solution was dried on a sample plate. The sample was loaded onto a AB SCIEX TOF/TOF 5800 MALDI-TOF spectrometer to obtain an average molecular weight for each antibody. Data

was acquired using AB SCIEX Analyst software and exported to MatLab (MathWorks). The number of modifications per antibody was then calculated based on the difference in molecular weight compared to the unmodified antibody and assuming a specific net mass added depending on the modification. Direct azide and TCO modifications had expected masses of 83.0 and 152.2 g/mol, respectively. TCO–PEG linker modifications with 4 and 24 PEG subunits had expected masses of 758.2 and 1639.9 g/mol, respectively.

2.2.6 Measurement of TCO and azide reactivities on antibodies

Functional TCO loadings were measured for direct TCO-modified antibodies using tetrazine–Oregon Green 488 (synthesized as previously reported.[106,107] Azide-modified antibodies were similarly assessed using DIBO–Alexa Fluor 488 (Thermo Fisher Scientific). Reactions were performed using 100 μg of antibody and 50 μM reactive dye in PBS containing 5% DMF at room temperature for 4 hours. To study the mechanism of TCO inactivation, reaction of direct TCO-modified antibodies with tetrazine–Oregon Green 488 were also performed in PBS containing 10% DMF or PBS containing 5% DMF and 5% DMSO. All samples were purified into PBS using Zeba spin desalting columns, and the number of fluorophores per antibody was determined by absorption measurements.

2.2.7 Analysis of antibody binding

A431 cells (500, 000 cells/sample) were fixed using 4% formaldehyde in PBS and washed using PBS. Binding experiments involved an indirect assay since secondary antibodies may no longer recognize the modified antibodies, particularly for the TCO–PEG cases. This involved labeling cells with unmodified and azide-, TCO-, and TCO–PEG-modified antibodies at concentrations ranging from 0.6 to 200 nM in 100 μL of PBS

containing 1 mg/mL bovine serum albumin (PBS+) for 30 minutes at room temperature. After washing 3 times with ice-cold PBS+ by centrifugation, samples were incubated with Oregon Green 488-modified antibody at 10 μg/mL in 100 μL of PBS+ for 30 minutes on ice and again washed 3 times. Finally, fluorescence was assessed using an LSRII flow cytometer (BD Biosciences) and analyzed using FlowJo software. The ability of the first antibody to block the Oregon Green 488-labeled antibody is representative of binding activity. Fully blocked conditions were indicated by the signal obtained for the unmodified antibody, and the fully unblocked condition was represented by cells treated only with the Oregon Green 488-labeled antibody. Specifically, the mean fluorescence intensity was subtracted from values obtained for cells incubated only with Oregon Green 488–antibody, and all samples were then normalized to the unmodified control (100%). Kinetic binding analyses were performed using GraphPad Prism.

2.2.8 Preparation of quantum dots

Synthesis of tetrazine–amine and NHS–tetrazine were as previously reported.[107] Amine-terminated quantum dots (Thermo Fisher Scientific) were modified with NHS–tetrazine. Briefly, quantum dots were first buffer-exchanged into PBS using Amicon Ultra-4 centrifugal devices. The reaction was performed using 0.8 nmoles of quantum dots and 500 equivalents of NHS–tetrazine in PBS containing 5% DMF and 0.01 M $NaHCO_3$ for 3 hours at room temperature. Tetrazine–quantum dots were purified into PBS using centrifugal filters. To prepare quantum dot immunoconjugates, 200 μg of antibody was modified with 10 equivalents of TCO–NHS, buffer-exchanged using a Zeba spin desalting column, and reacted with 0.15 nmoles of tetrazine–quantum dots in 1 mL of PBS+ for 3 hours at room temperature. Quantum dot immunoconjugates were purified with Sephacryl S-400 (GE

Healthcare) in PBS using an AKTA Pure FPLC (GE Healthcare). Final concentrations were determined by absorption measurements using the quantum dot stock solution for calibration.

2.2.9 Quantification of cell labeling using flow cytometry

A431 cells (500,000 cells/sample) were labeled with TCO- or TCO–PEG-modified antibodies at saturating or near-saturating concentrations (10–30 μg/mL) in 100 μL of PBS+ for 30 minutes at room temperature. Cells were then washed 3 times by centrifugation with PBS+, reacted with 50 μM tetrazine–Oregon Green 488 or 10 nM tetrazine–quantum dots for 30 minutes at room temperature, and washed 3 times by centrifugation with ice-cold PBS+. Fluorescence intensities were assessed by flow cytometry and analyzed using FlowJo software. Cells treated with no primary antibody, TCO-modified nonbinding control, or TCO–PEG24-modified nonbinding control antibodies were used for controls. The number of reactive TCOs for the TCO–PEG-modified antibodies was determined based on fluorescence intensity of the Oregon Green 488, relative to the signal from the TCO-modified antibodies that were directly assessed for TCO reactivity previously. Adjustments were made for antibody binding level to obtain true representations of the number of reactive TCOs per antibody.

2.2.10 Confocal imaging

A431 cells were grown on Lab-Tek glass chamber slides. Prior to experiments, samples were washed with PBS+ and labeled with TCO-, TCO–PEG, or azide-modified antibodies under saturating or near-saturating concentrations (10–30 μg/mL) for 30 minutes at room temperature. After washing with PBS+, cells were labeled with tetrazine–

Oregon Green 488 or DIBO–Alexa Fluor 488 (Thermo Fisher Scientific) at 50 nM or tetrazine–quantum dots at 10 nM for 30 minutes at room temperature. Cells were then washed and imaged using an inverted laser scanning confocal microscope (FV1000, Olympus) with a 60× water immersion lens, and data was acquired with Fluoview software (Olympus).

2.3 Results

We first set out to explore TCO reactivity using a mouse monoclonal antibody that is specific for the cancer biomarker EGFR. Total TCO modification levels were measured using matrix-assisted laser desorption/ionization time-of-flight (MALDI-TOF) mass spectrometry (Figure 2.2), whereas TCO reactivity was determined based on absorbance readings after complete reaction with tetrazine–Oregon Green 488.

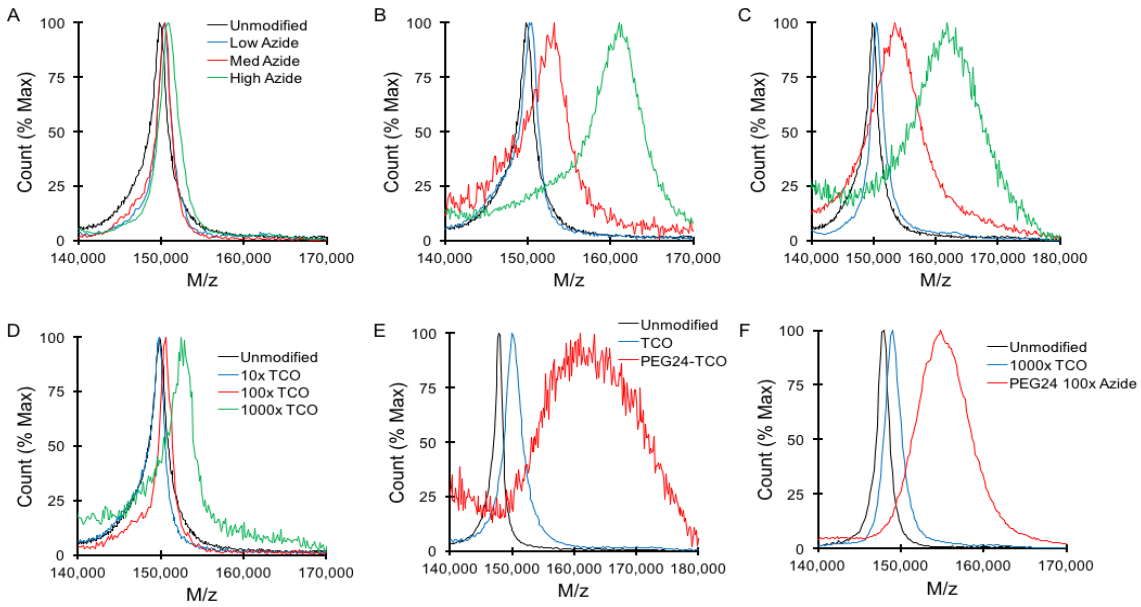

Figure 2.2. Representative MALDI-TOF results. (A-C) Anti-EGFR antibody conjugated with azide and measured (A) directly or after reaction with (B) PEG_4-TCO or (C) PEG_{24}-TCO. (D) Anti-EGFR antibody conjugated after conjugation with TCO. (E-G) Conjugation of TCO and PEG_{24}-TCO to (E) anti-EpCAM, and (F) anti-TfR

We found that TCO conjugation was efficient (Figure 2.3A), but, remarkably, only 10% of the moieties were functional (Figure 2.3B). Reactivity was identical when measured immediately following conjugation and after waiting up to 24 h (Figure 2.3C). This suggests that TCO was not inactivated by *trans–cis* isomerization, as this conversion has been shown to require significant amounts of time even in the presence of a catalyst. For example, 6 h or more is needed for full isomerization in the presence of free thiols at high concentrations and elevated temperatures or transition metals in serum.[108,110]

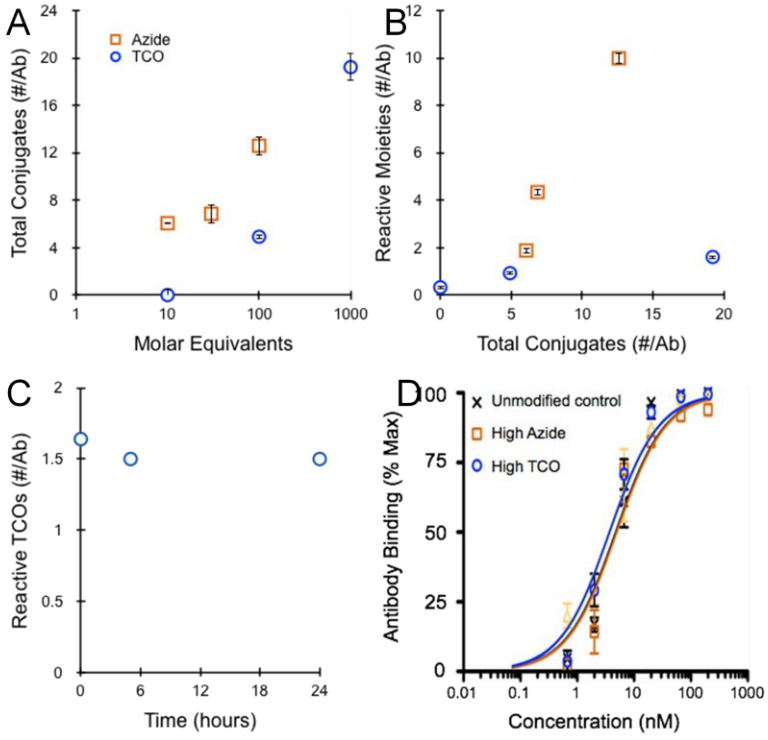

Figure 2.3. Conjugation of TCO and azide to an anti-EGFR antibody using standard amine-reaction procedures. (A) Total attachment levels determined by MALDI-TOF versus the number of reaction equivalents, showing that modification efficiencies are similar. (B) Reaction of the TCO-antibodies with tetrazine-fluorophore revealed that only 10% of the TCOs were functional. In contrast, nearly all azide modifications were reactive to DIBO-fluorophore. (C) Functional TCO level was similar on the anti-EGFR antibody immediately after treatment with NHS-TCO or after being maintained 5 and 24 hours at room temperature, suggesting that TCOs were not inactivated by trans-cis isomerization. (D) Antibody binding affinity was not affected after modification with high levels of azide or TCO. Error bar represent the standard error of at least three independent experiments.

To explore steric hindrance, we employed the strain-promoted bioorthogonal reaction between azide and cyclooctyne that also yields a bulky cycloaddition product. Azide conjugation efficiency was similar to the TCO (Figure 2.3A), but nearly all moieties could be reacted with dibenzocyclooctyne (DIBO)–Alexa Fluor 488 (Figure 2.3B). Discrepancies at low loadings were likely due to the small size of azide groups, which makes mass changes difficult to distinguish by MALDI-TOF. We expect that this result should extend to tetrazine/TCO cycloaddition, although the smaller azide could be less sensitive to sterics, as noted for methyl-cyclopropene in relation to TCO.[111] Interestingly, neither TCOs nor azides interfered with antibody binding affinity even at high modification levels (Figure 2.3D). This was determined using an indirect competitive binding assay with A431 epidermoid cancer cells. Fitting the binding data indicated equilibrium dissociation constants (K_D) were all close to 5 nM. On the basis of the above evidence, we speculated that hydrophobic TCOs were interacting with external or even internal domains of the antibody, masking it from tetrazine reaction. Internal burying could explain how an antibody decorated with almost 20 hydrophobic TCOs can remain stable in aqueous solution. To explore whether the presence of a polar solvent during conjugation procedures influenced TCO masking, we decreased the concentration of dimethylformamide (DMF) to <1%, but this had no effect on total modification levels and only slightly decreased reactive sites (Figure 2.4A). Increasing DMF concentration or adding dimethyl sulfoxide (DMSO) during the reaction with tetrazine–Oregon Green 488 did reveal 30% more reactive TCOs (Figure 2.4B). However, the majority remained inactive, and further increases in solvent destabilized the antibody. Further access to the masked TCOs could potentially be obtained using a more hydrophobic tetrazine conjugate such as a bodipy fluorophore.

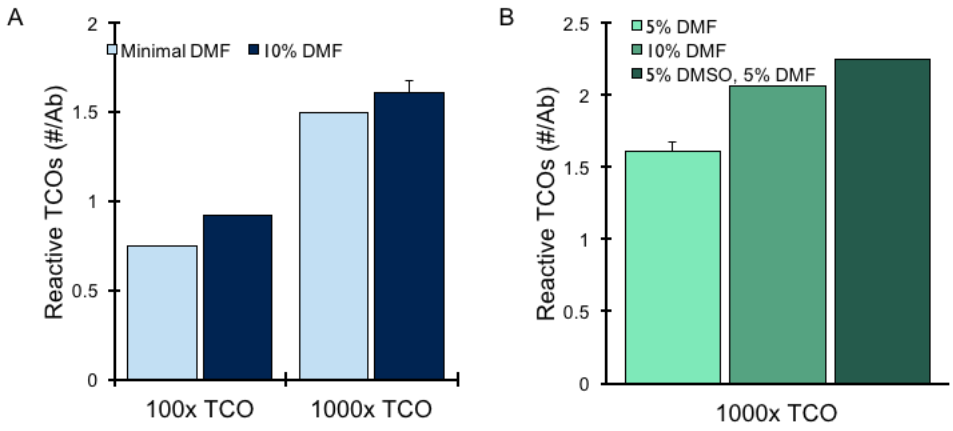

Figure 2.4. Effect of solvent concentration during antibody conjugation with TCO and tetrazine reaction. (A) Increasing DMF concentration did slightly enhance TCO reactivity, however. (B) Adding more DMF or DMSO during the reaction of the TCO-antibody with tetrazine-Oregon Green 488 revealed up to 30% more TCOs, but most modifications still remained non-functional. Error bars represent the standard error of at least three independent experiments.

We next explored whether introduction of TCO using hydrophilic PEG linkers could maintain reactivity. We chose to incorporate PEG–TCO onto the antibody using the mutually orthogonal azide/DBCO reaction to improve control over coupling density, as we have already established that azide is an ideal reactant on the antibody at varying densities (Figure 2.3B). We created heterobifunctional DBCO–PEG–TCO molecules with 4 and 24 polymer subunits by sequentially reacting amine–PEG–carboxylic acid with the same amine-reactive TCO employed for direct antibody conjugations. The carboxylic acid was then modified with amine-DBCO via *N*-hydroxysuccinimide (NHS) ester activated chemistry, and the resulting DBCO–PEG–TCO was reacted with azido-antibodies (Figure 2.1).

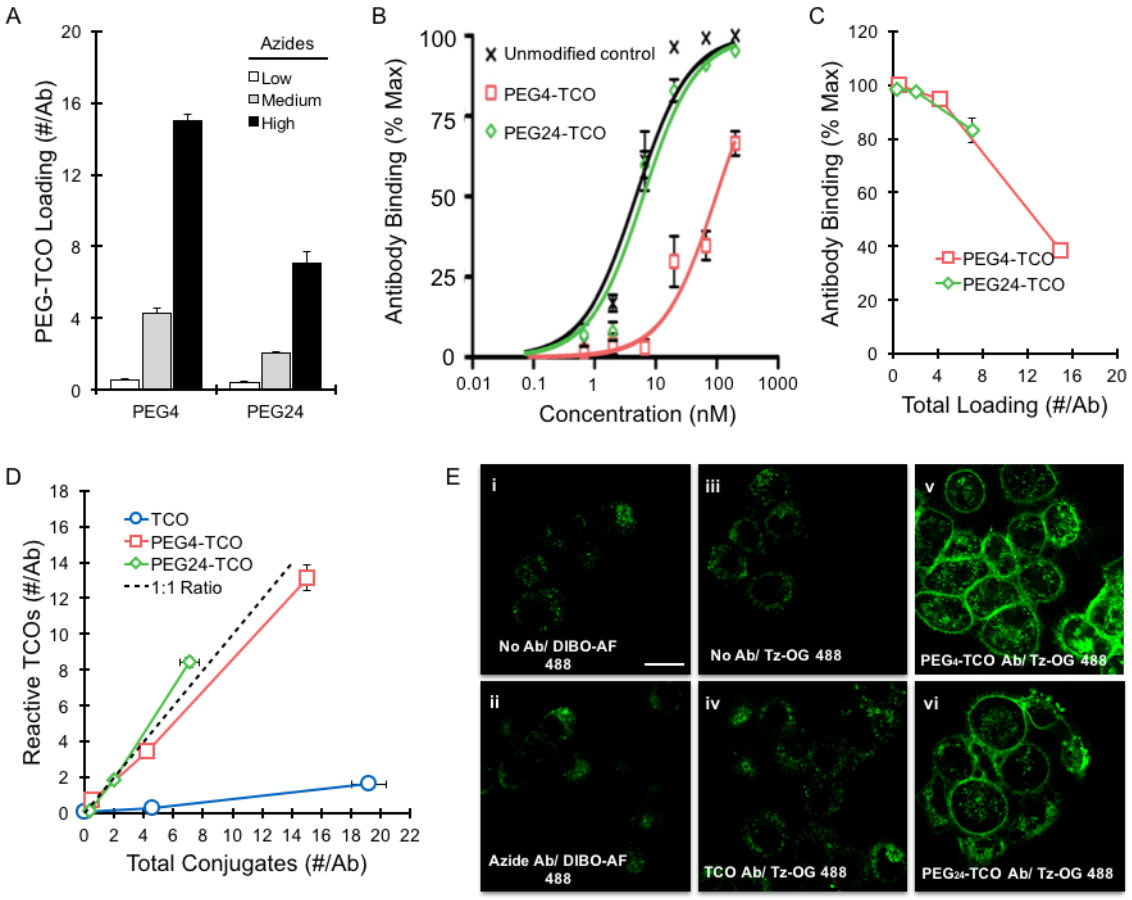

Figure 2.5. Introduction of TCO via PEG linkers using azide/DBCO reaction. (A) Attachment of heterobifunctional DBCO-PEG_n-TCO (n = 4 or 24) to azide-modified anti-EGFR antibodies. (B) Kinetic binding curves after modification with PEG-TCOs. Binding affinity was unaffected for the PEG_{24} (K_D = 6 nM), but significantly reduced for the PEG_4 (K_D =100 nM). (C) Relative antibody binding at 10 μg/mL concentration showing that binding activity is retained for <8 linkers. (D) TCOs introduced via PEG linkers are fully reactive, determined for live A431 cells labeled with modified antibodies and reacted with tetrazine-Oregon Green 488 by flow cytometry. (E) Confocal images of live A431 cancer cells labeled with (i,iii) no antibody or the anti-EGFR antibody modified with (ii) azide, (iv) TCO, (v) PEG_4-TCO, and (vi) PEG_{24}-TCO at the highest levels. Cells were then probed with (i-ii) DIBO-Alexa Fluor 488 or (iii-vi) tetrazine-Oregon Green 488 at 50 nM for 30 min. Scale bar: 20 μm. Error bars represent the standard error of at least three independent experiments.

Total loadings of the PEG_4 and PEG_{24} linkers were assessed by MALDI-TOF (Figure 2.5) and varied in a dose-dependent manner with the initial azide density. Attachment levels for the PEG_4–TCO were higher in all cases, with a maximum valency of 15 that was close to the 13 azides that were directly measured by MALDI-TOF. Conjugation of the

PEG_{24}–TCO was less efficient, with values approximately one-half that of the PEG_4–TCO. It is unclear whether lower conjugation levels for the PEG_{24} were due to physical crowding or the presence of unreacted DBCO-amine in the preparation. Increasing linker concentration in the reaction did not affect results, however.

We next determined whether the PEG–TCO linkers interfered with antibody binding again using the indirect competitive assay with A431 cells. We found that binding at 10 μg/mL concentration was unaffected for both the PEG linkers until attachment levels exceeded 8 (Figure 2.5B). Further analysis of full binding profiles confirmed that affinity was close to control for 8 PEG_{24}–TCOs (K_D = 6 nM), but it was dramatically reduced for 15 PEG_4–TCOs (Figure 2.5C). Reduced binding in the latter case can be attributed either to decreased affinity or a population of permanently inactivated antibody, but, in either case, binding was almost fully recovered by increasing the antibody concentration to 30 μg/mL (Figure 2.6). Importantly, TCO moieties introduced via both PEG linkers were fully functional (Figure 2.5D). This was determined under pretargeting conditions, in which A431 cells were labeled with TCO–PEG–antibodies, reacted with tetrazine–Oregon Green 488 at 50 μM for 30 min in the presence of BSA, and analyzed by flow cytometry. The TCO–antibodies prepared by direct amine reaction were also evaluated and used to convert raw fluorescence signals (Figure 2.6) into the number of functional TCOs per antibody, after adjusting for antibody binding levels. These results were highly specific, as background signals from a nonbinding control antibody conjugated with TCO and PEG_{24}–TCO were similar to autofluorescence (Figure 2.6).

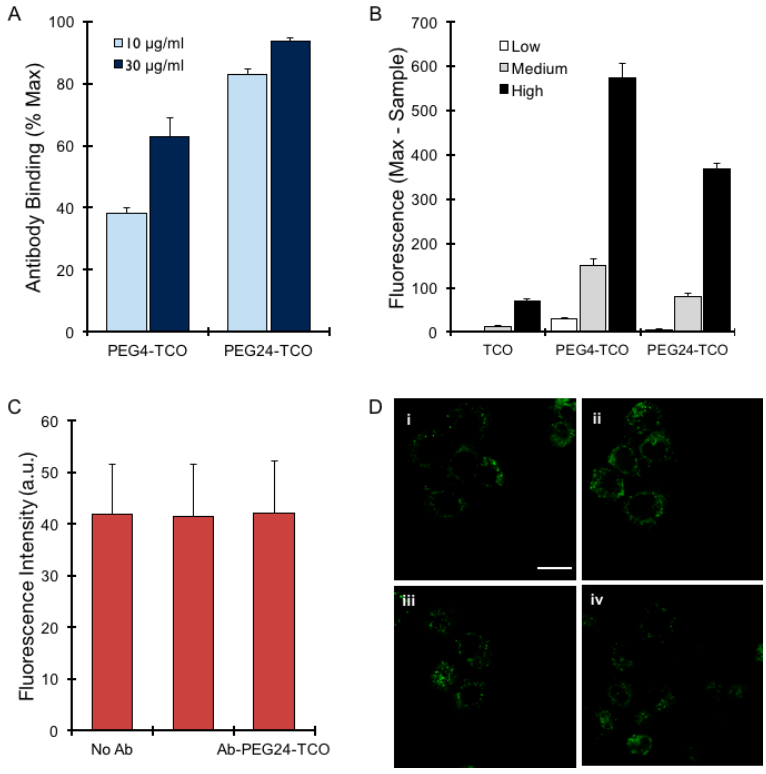

Figure 2.6. Binding and background levels for TCO-PEG-modified anti-EGFR antibody. (A) Increasing antibody concentration to 30 µg/mL helped recover reduced binding. (B) Raw fluorescence signals measured by flow cytometry after reacting tetrazine-Oregon Green 488, after background subtraction. (C) Background signal levels of tetrazine-Oregon Green 488 were identical using no antibody and a non-bonding control antibody modified with TCO and PEG_{24}-TCO. (D) Confocal images of live A431 cancer cells labeled with (i,ii) no antibody or non-bonding control antibody modified with (iii) TCO or (iv) PEG_{24}-TCO. Cells were then (i) left untreated to show autofluorescence or probed with (ii-iv) tetrazine-Oregon Green 488 at 50 nM for 30 min. Scale bar: 20 µm. Error bars represent the standard error of at least three independent experiments.

In total, antibody reactivity enhancements were more than 10- and 5-fold for the 4 and 24 subunit PEGs, respectively. To illustrate these improvements, we performed confocal imaging of A431 cells labeled with TCO- or TCO–PEG-modified antibodies, followed by reaction with an extremely low concentration (50 nM) of tetrazine–Oregon Green 488 for 30 min at room temperature in the presence of 1 mg/mL BSA (Figure 2.5). We similarly tested the anti-EGFR antibody modified with 15 azides followed by reaction with DIBO–Alexa Fluor 488. The TCO–PEG–antibodies yielded dramatically higher

fluorescent signals than the TCO and azide cases, which were indistinguishable from autofluorescence. Thus, the PEG linkers effectively prevented TCO inactivation after antibody conjugation, presumably by increasing solubility and preventing interactions with the antibody while maintaining faster reaction kinetics than azide/DIBO. The PEG linkers should also be advantageous for *in vivo* applications by reducing antibody immunogenicity. A potential drawback is that higher rates of TCO inactivation by *trans–cis* isomerization have been reported in serum when using PEG linkers.[110] However, this study used a linker containing a phenyl group (benzyl ether) in between the TCO and a 12 subunit PEG. Therefore, it is possible that inactivation may not be as extensive for our carbonate linker that is more hydrophilic and 4 subunit PEG that is shorter.

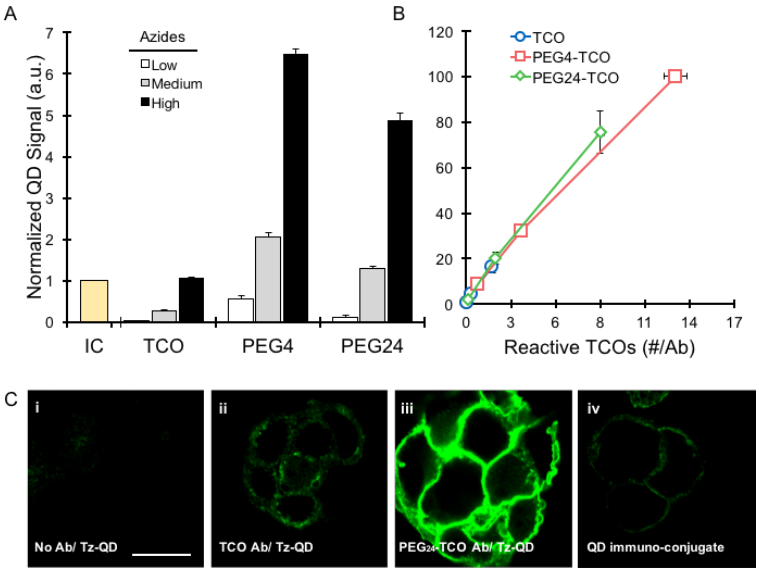

Figure 2.7. Amplification of QD binding. (A) QD signal determined by flow cytometry following cycloaddition reaction to modified anti-EGFR antibodies on A431 cancer cells. The TCO-PEG-antibodies had higher binding levels, by as much as 6-fold for the PEG_4. The QD immuno-conjugate was similar to the TCO-antibody/Tz-QD. (B) QD binding levels correlated directly with the number of reactive TCOs, showing no influence of PEG length. (C) Confocal images of A431 cells labeled with (i,iv) no antibody or the anti-EGFR antibody conjugated with (ii) TCO or (iii) PEG_{24}-TCO. Cells were then probed with (i-iii) tetrazine-QD or (iv) QD immuno-conjugate at 50 nM for 30 min. Scale bar: 20 μm. Error bars represent the standard error of at least three independent experiments.

A powerful application of tetrazine/TCO pretargeting is to amplify nanomaterial binding to cells and microvesicles.[85,86,100,102,104] Therefore, we labeled A431 cells with the TCO- and PEG–TCO-modified anti-EGFR antibodies and reacted with tetrazine-modified quantum dots (QD) at 10 nM concentration for 30 min. A QD immunoconjugate was also prepared and incubated under identical conditions. Fluorescence intensities measured by flow cytometry were similar for the QD immunoconjugate and TCO–antibody/tetrazine–QD cases (Figure 2.7). Signals from both TCO–PEG–antibodies/tetrazine–QD cases were greater by as much as 6-fold. It should be noted that chemical amplification levels can increase further over immunoconjugates at higher nanoparticle concentrations.[85] (Haun 2010) These results were again entirely specific, and PEG length did not affect QD binding levels (Figure 2.7B). Improved detection capacity of the PEG_{24}–TCO was confirmed using confocal microscopy (Figure 2.7C).

Finally, we modified monoclonal antibodies specific for transferrin receptor (TfR) and EpCAM with TCO and PEG_{24}–TCO using the highest valency conditions. Functional and total modification levels were similar to the anti-EGFR antibody, and TCO reactivity was enhanced 3- to 4-fold using the PEG linker (Figure 2.8A). Binding of the TCO–PEG_{24}-modified anti-TfR antibody was slightly diminished. Similar 5-fold signal enhancements were observed by flow cytometry for both TCO–PEG_{24}–antibodies after reaction with tetrazine-modified QDs (Figure 2.8B). Improved detection capabilities were also demonstrated by confocal imaging using tetrazine-modified Oregon Green 488 and QDs (Figure 2.8C). These results confirm that TCO masking after conjugation to monoclonal antibodies is not a rare phenomenon and that reactivity can reliably be improved by introducing via PEG linkers and our dual bioorthogonal coupling strategy.

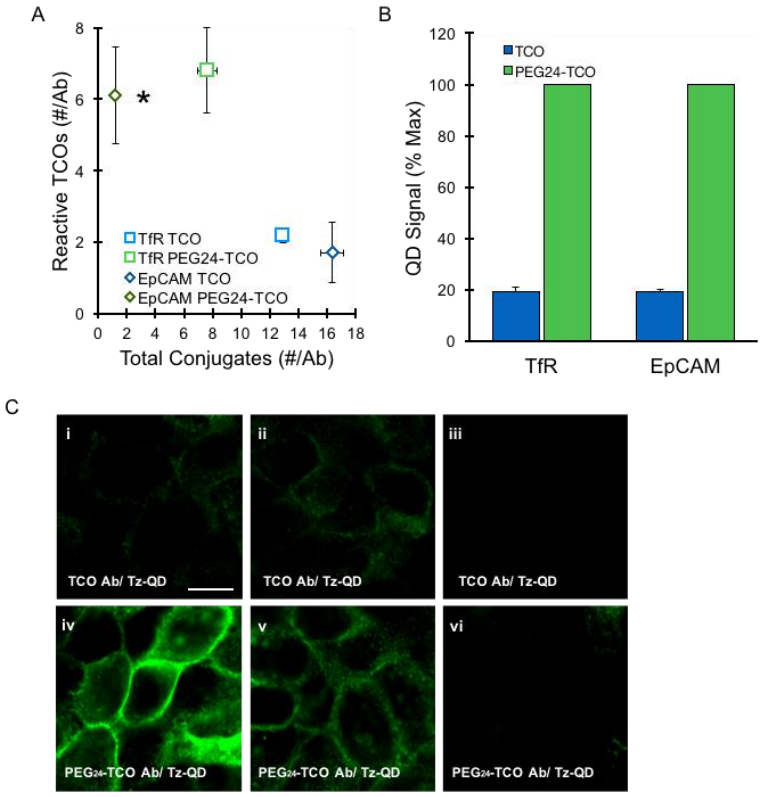

Figure 2.8. Extension to different antibodies. (A) Anti-TfR and EpCAM antibodies had low TCO reactivity (12-15%) after direct amine-conjugation, but the PEG_{24}-TCO increased reactive TCO density 3 to 4-fold. *MALDI-TOF analysis of the TCO-PEG_{24}-modified anti-EpCAM antibody was limited by difficulties with desorption. (B) Tetrazine-QD signals after reaction with TCO- and TCO-PEG_{24}-modified anti-EpCAM and TfR antibodies on A431 cancer cells at 10 nM for 30 minutes. Similar to the anti-EGFR antibody, 5-fold signal enhancements were observed using the PEG_{24}-TCO in both cases. (C) Confocal images of A431 cells labeled with (i, iv) anti-EpCAM, (ii, v) anti-TfR, or (iii, vi) non-binding control antibodies. The antibodies were modified with (i-iii) TCO or (iv-vi) PEG_{24}-TCO at the highest densities, and reacted with tetrazine-QD at 10 nM for 30 min. Scale bar: 20 μm. Error bars represent the standard error of at least three independent experiments.

2.4 Discussion

In this work, we have discovered that the majority of TCOs conjugated to antibodies using standard amine-coupling procedures are nonreactive. To address this issue, we introduced TCO via hydrophilic PEG linkers, which fully preserved reactivity and improved detection signals for tetrazine-modified fluorophores and quantum dots. Taken together with other evidence presented, we believe that nonfunctional TCOs are buried within the antibody. This likely occurs during conjugation procedures, as TCO reactivity is later

maintained in the presence of cells and high concentrations of BSA protein. We believe this work establishes a new method to prepare TCO-modified antibodies that will significantly advance bioorthogonal pretargeting studies such as *in vivo* imaging and chemical amplification of nanoparticle binding. Additionally, this technique could be useful for signal amplification of activatable fluorochromes.[118–120] Although we utilized azide/DBCO cycloaddition reaction to couple PEG–TCO to antibodies, we expect that direct amine-reaction or alternative chemistries should provide similar results. Future work could explore whether similar masking effects occur for different hydrophobic reactants such as DBCO, norbornene, and methyl-cyclopropene, alternative linkers directly distal to the TCO such as those containing bulky phenyl groups,[99] or new bicyclic TCO derivatives that have faster reaction rates, greater stability, and, for the dioxolane-fused TCO, potentially greater hydrophilicity.[121,122] Expanding these investigations to different types of proteins or biological molecules, including site-specific methods that involve genetic encoding,[123–125] would also be of interest.

Chapter 3

One-step antibody conjugation for preserved bioorthogonal reactivity

3.1 Introduction

Bioorthogonal "click" chemistries are increasing in popularity for pretargeting strategies in molecular detection of tumor cells[91,126–128] Studies employing bioorthogonal pretargeting have predominantly used the catalyst-free inverse-electron-demand Diels-Alder cycloaddition between 1,2,4,5-tetrazine (Tz) and *trans*-cyclooctene (TCO) due to its high selectivity and unprecedented speed, which is critical to success in pretargeting scenarios[94,108,110].These attributes enable selective labeling of molecules in complex biological environments for sensitive imaging applications. Despite the utility, we recently reported that the majority of TCOs conjugated to monoclonal antibodies via standard amine-coupling are non-reactive. We observed that *trans-cis* isomerization was not the cause of initial non-functionality, nor does steric hinderance contribute to non-reactive TCO moieties. Instead, antibody-bound TCO moieties are likely interacting with hydrophobic regions of the antibody, rendering the moieties inaccessible. We restored the reactivity of antibody-bound TCO using a novel, dual bioorthogonal approach in which heterobifunctional dibenzocyclooctyne(DBCO)–PEG–TCO molecules reacted with azido-antibodies. A 5-fold signal enhancement from pretargeting can be achieved as a result. (Chapter 2)

While this improvement in TCO-reactivity achieved with the two-step approach was impressive, the mechanism remained unclear, as both the hydrophilic PEG polymer and hydrophobic triazole product could have been involved in deterring hydrophobic interactions between the TCO and antibody that would otherwise render the TCO

inaccessible. Obtaining this insight could be helpful in establishing a one-step coupling strategy that could retain all TCO moieties in a fully functional form.

While the reaction between TCO and Tz displays unprecedented speed, alternative bioorthogonal chemistries possess other beneficial traits for molecular targeting. For example, though norbornene (NB) and cyclopropene (CP) react with Tz at relatively slower rates,[129] they are more stable overtime, compared to TCO. New bicyclic derivatives of TCO, bicyclononene (BCN), have faster reaction rates, greater stability, and, potentially, greater hydrophilicity than TCO[121,122]. Additionally, CP may be preferred over other bioorthogonal reactants because of its small size that enables specific targeting with minimal perturbation to target molecules.[109,111] DBCO, CP and TCO are also mutually orthogonal with certain pairs, and can therefore be used in tandem for multi-target imaging.[117,130] Though the suite of bioorthgonal chemistries has utility in numerous applications, it is unclear to what extent these hydrophobic bioorthogonal reactants undergo similar masking effects to those observed with TCO.

In this study, we investigate whether other strained alkenes become nonreactive after antibody conjugation. Surprisingly, we find that all dienophiles tested undergo some degree of masking likely attributed to burying. Based on previous insights, we explore various linkers in an effort to restore dienophile reactivity in a one-step coupling technique (Figure 3.1). We create a panel of amine-reactive TCO moieties containing hydrophilic, hydrophobic, and amphiphilic distal linkers, and test their ability to retain TCO reactivity after conjugation to the humanized monoclonal antibody, Trastuzumab.

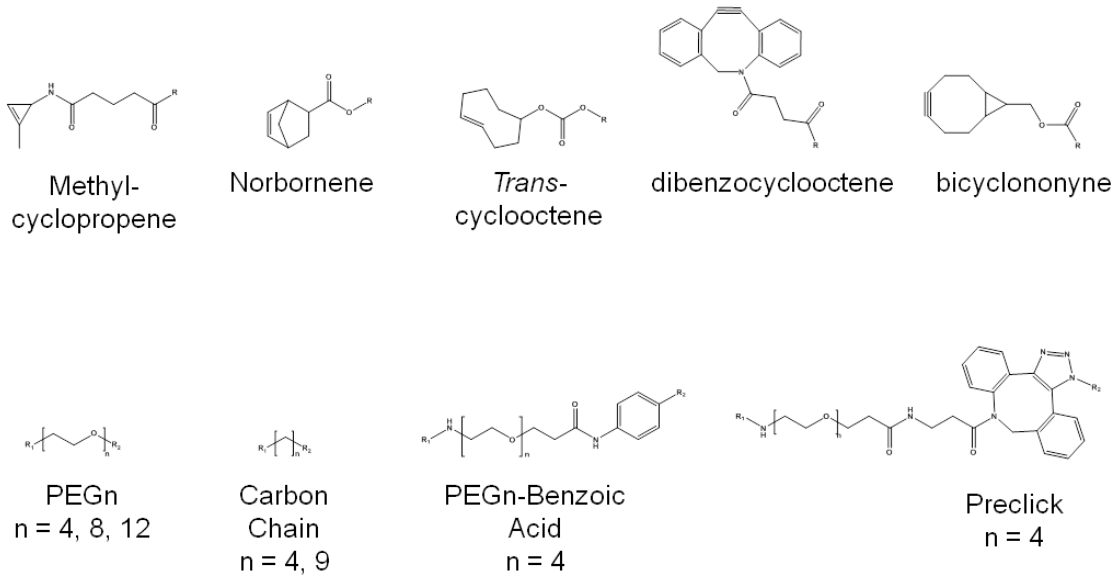

Figure 3.1 Schematic of bioorthogonal reactants and linkers

The dual, bioorthogonal two-step modification approach, established in Chapter 2, expectedly yields high TCO reactivity. We find that short, amine-reactive PEG linkers alone are not sufficient to fully preserve TCO reactivity. Gains in TCO reactivity with increased PEG subunits are paired with diminished antibody binding. Interestingly, amphiphilic linkers containing PEG and either the triazole product, a benzene ring, or a short alkyl chain perform as poorly as the standard carbamate linker, with TCO reactivity at approximately 10%. Instead, reactivity is improved to greater than 60% by simply using a short alkyl chain distal to the TCO.

3.2. Methods

3.2.1 Linker synthesis

The synthesis of DBCO-PEG-TCO linkers is detailed in Chapter 2. NHS-PEG$_n$-dienophile linkers were synthesized from a carboxylic acid-PEG$_n$-amine: 10 mg of carboxylic acid-PEG$_n$-amine (1 equivalent) reacted with 1.2 equivalents of either TCO-NHS

or NB-NHS (synthesized as previously reported[106,107]) in 2 mL of DCM containing 1.5 equivalents of triethylamine for 16 hours on ice. The reaction was concentrated, and the crude material reacted with N,N'-disuccinimidyl carbonate in triethylamine overnight to make the corresponding NHS-PEG_n-dienophile. This reaction mixture was purified using silica gel chromatography with a DCM/methanol gradient. NHS-PEG_n-dienophiles were verified by proton NMR.

TCO–alkyl–NHS linkers (valeric acid or decanoic acid) were synthesized from a carboxylic acid–alkyl–amine: 10 mg of carboxylic acid–alkyl–amine (1 equivalent) reacted with 1.2 equivalents of TCO–NHS in 2 mL of DCM containing 1.5 equivalents of triethylamine for 16 hours on ice. The reaction was concentrated, and the crude material reacted with N,N′-disuccinimidyl carbonate in triethylamine overnight to make the corresponding NHS–alkyl–TCO. This reaction mixture was purified using silica gel chromatography with a Hex/EtOAc gradient. TCO-alkyl-NHS linkers were verified by proton NMR.

3.2.2 Antibody modifications

Trastuzumab (Genentech) was buffer-exchanged into PBS using Zeba spin desalting columns (Thermo Fisher Scientific) prior to modification. DBCO-NHS, DBCO-PEG_4-NHS, and TCO-PEG_{12}-NHS were purchased from Click Chemistry Tools. BCN-NHS and BCN-PEG_4-NHS were purchased from Conju-Probe. The synthesis of all other linkers is detailed above. For antibody modifications, 200 μg of antibody reacted with 5-100 equivalents of amine-reactive linker in 0.2 mL PBS containing 10% DMF and 0.1 M $NaHCO_3$ (pH 8.5) for 3 hours at room temperature. Azide and Oregon Green 488A conjugates were prepared in a similar manner using 5, 10, or 30 equivalents of NHS-azide (Thermo Fisher Scientific) or 10

equivalents of NHS–Oregon Green 488 (Thermo Fisher Scientific), with DMF omitted from the solvent. TCO, azide, and Oregon Green 488-modified antibodies were purified using Zeba spin desalting columns. PEG–TCO conjugates were prepared by reacting the different azide-modified antibodies with DBCO–PEG4–TCO. Reactions were carried out using 10-fold excess relative to the number of azide moieties for 4 hours at room temperature. TCO–PEG–antibodies were purified into PBS using Amicon Ultra-4 centrifugal filtration systems (Millipore). Antibody concentration was determined by absorption measurement recorded on a Thermo Scientific NanoDrop 2000 spectrophotometer. Oregon Green 488 density was also measured by absorption to be 2 dyes/antibody.

3.2.3 *MALDI-TOF analysis of modified antibodies*

Total linker densities were determined based on changes in mass using matrix-assisted laser desorption/ionization time-of-flight, MALDI-TOF, mass spectrometry. The matrix was prepared using 1 mg of sinapinic acid dissolved in 100 μL of 70:30 acetonitrile/water with 0.1% trifluororacetic acid. Modified antibodies were buffer-exchanged into water and concentrated to greater than 1 mg/mL using Amicon Ultra-4 centrifugal filters. Concentrated antibody solutions were combined with sinapinic acid matrix in a 2:1 ratio, and 1 μL of the solution was dried on a sample plate. The sample was loaded onto a AB SCIEX TOF/TOF 5800 MALDI-TOF spectrometer to obtain an average molecular weight for each antibody. Data was acquired using AB SCIEX Analyst software and exported to MatLab (MathWorks). The number of modifications per antibody was then calculated based on the difference in molecular weight compared to the unmodified antibody and assuming a specific net mass added depending on the modification.

3.2.4 Measurement of dienophile reactivity on antibodies

Functional dieneophile loadings were measured using tetrazine–Oregon Green 488. Reactions were performed using 100 μg of antibody and 200 μM reactive dye in PBS containing 5% DMF at room temperature for 3 hours for BCN and TCO containing linkers, or 24 hours for remaining dienophiles. All samples were purified into PBS using Zeba spin desalting columns, and the number of fluorophores per antibody was determined by absorption measurements.

3.2.5 Cell labeling

SK-BR-3 cells (250, 000 cells/sample) were washed using PBS containing 1 mg/mL BSA (PBS+). Binding experiments involved an indirect assay since secondary antibodies as detailed in Chapter 2. Briefly, cells were labeled with unmodified or linker-modified antibodies at 1 μg/mL in 100 μL of PBS+ and incubated for 30 minutes at room temperature. After washing 3 times with ice-cold PBS+ by centrifugation, samples were incubated with Oregon Green 488-modified antibody at 2 μg/mL in 100 μL of PBS+ for 30 minutes on ice and again washed 3 times. Finally, fluorescence was assessed using an Attune NxT flow cytometer (Thermo Fisher Scientific) and analyzed using FlowJo software. The ability of the first antibody to block the Oregon Green 488-labeled antibody is representative of binding activity. Fully blocked conditions were indicated by the signal obtained for the unmodified antibody, and the fully unblocked condition was represented by cells treated only with the Oregon Green 488-labeled antibody. Specifically, the mean fluorescence intensity was subtracted from values obtained for cells incubated only with Oregon Green 488–antibody, and all samples were then normalized to the unmodified control (100%).

3.2.6 AlogP and length measurements for linkers

AlogP values of NHS-dienophiles and NHS-PEG_n-TCO linkers were calculated using ALOGPS 2.1 software. Length of NHS-PEG_n-TCO linkers was approximated using Chem3D.

3.3 Results

Recently, we uncovered masking of TCO modifications on several different antibodies after bioconjugation, though the extent of burying varied with antibody (Chapter 2). In this work, we first investigated whether TCO masking occurred after reaction to human monoclonal antibody, Trastuzumab (Figure 3.2A) Total modification levels were measured using MALDI-TOF, and reactive modifications were assessed by measuring absorbance readings after complete reaction with Tz-Oregon Green 488A. We found that for TCO modifications introduced via NHS-TCO, approximately 30% of total modifications were reactive, which is similar to previous observations. We also employed two-step, dual, bioorthogonal coupling to introduce TCO linkers onto antibodies, which restored reactivity of most TCO modifications; over 80% of total modifications were functional (Figure 3.2A). These results confirm that TCO masking after antibody conjugation is not uncommon, and that reactivity can reliably be uncovered by our two-step dual, bioorthogonal coupling strategy.

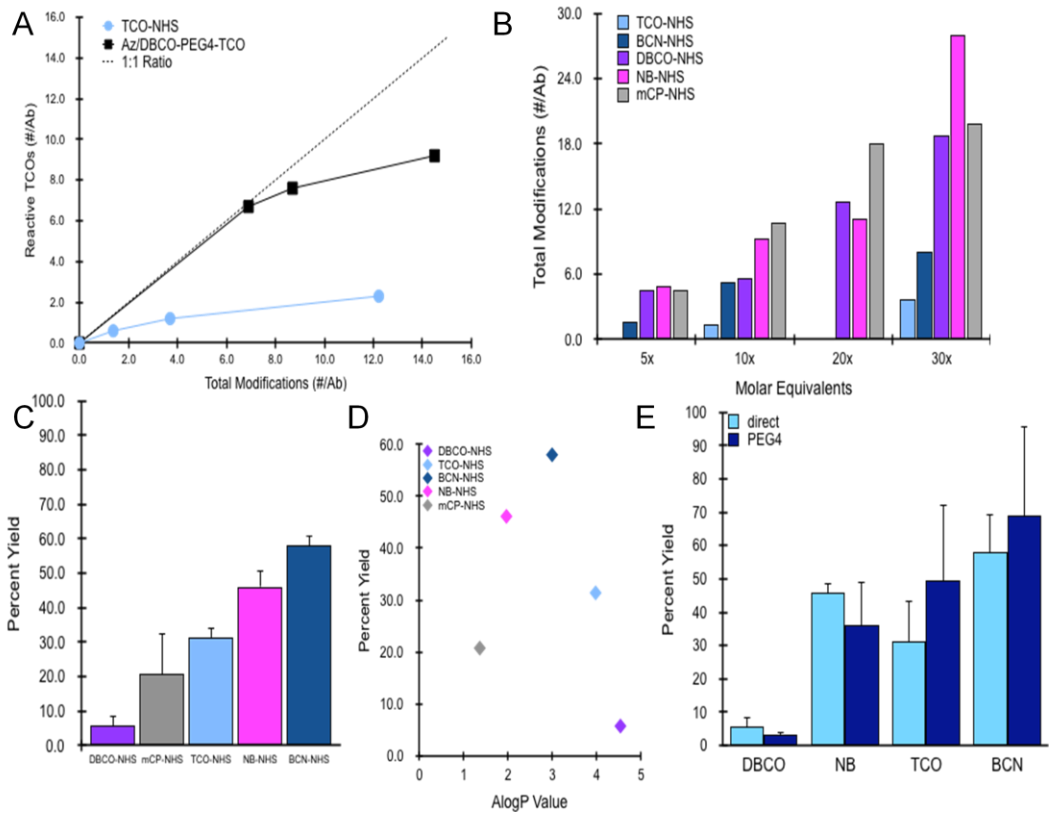

Figure 3.2 Conjugation of bioorthogonal dienophiles to Trastuzumab. (A) Total attachment levels determined by MALDI-TOF versus the number of functional attachments determined by reaction with Tz-fluorophore reveal TCOs directly coupled to antibodies are mostly nonreactive,. Introducing TCO via two-step bioorthogonal coupling preserves their reactivity. (B) Total attachment levels of amine-reactive dienophiles to Trastuzumab for given molar equivalents. (C) Percent reactive moieties out of total attachments for various dienophiles modified to antibodies via amine-reactive chemistry. (D) Percent reactive moieties out of total attachments as a function of AlogP values. (E) Perent reacive moieties out of total attachments for PEG4-dienophiles compared to direct amine-reactive counterparts.

Next, we explored whether other biooorthogonal reactants, (DBCO, NB, CP, and BCN) are also rendered non-functional after antibody conjugation. Antibody modifications for each amine-reactive dienophile were efficient, determined by measurement of total antibody loadings (Figure 3.2B). To study reactivity of dienophiles, we measured antibodies with low, medium, and high level modifications for a complete picture of antibody bioconjugation with each dienophile. Interestingly, we found that all dienophiles,

to some extent, yielded nonfunctional reactive groups upon bioconjugation. (Figure 3.2C) Importantly, when testing reactivity of antibody-bound dienophiles, functional assays were performed at saturating conditions to ensure that differences in the amount of nonfunctional moieties was related to accessibility of the bioorthogonal reactant, and not inherent differences in reaction rate with Tz-dye. We speculated that the degree of nonfunctional modifications for each strained alkene tested was related to the hydrophobicity of the molecule, which could encourage more hydrophobic burying in some reactants compared to others; thus, explaining the variation in the extent of this phenomenon across dienophiles. To study this theory, we calculated AlogP values for each bioorthogonal reactant. AlogP values are an estimate of the logarithim of the 1-octanol/water partition coefficient for a given molecule, and are a measure of the molecules hydrophobicity.[131] High AlogP values indicate higher molecular hydrophobicity. To determine whether molecular hydrophobicity could explain the degree of nonfunctional modifications, we measured the percent yield of functional-to-total modifications as a function of AlogP values. (Figure 3.2D) We find that these values did in fact negatively correlate; increases in molecular hydrophobicity translated to decreased percent of reactive functional groups, suggesting that the broad range of dienophiles test were rendered nonfunctional at least partially due to hydrophobic burying. In an effort to restore the functionality of antibody-bound modification in a one-step approach, we utilized amine-reactive PEG_4-dienophiles for conjugation. Surprisingly, PEG_4 linkers did not enhance the percent of reactive groups for DBCO or NB conjugations, and resulted in only marginal improvements for TCO and BCN. This directly-coupled PEG linker did not have the same capacity to restore reactivity as its two-step counterpart (Figure 3.2A). This

finding suggests that hydrophilicity alone may not fully explain the benefits provided with the two-step modification technique, and that the nature of a two-step reaction or the hydrophobic triazole reaction product is also at play to prevent TCO burying.

In an effort to fully preserve reactivity of antibody-bound bioorthogonal groups with a one-step coupling technique, we rationally designed a panel of linkers that could maximize reactivity (Figure 3.1). We increased the length of the PEG linker from four subunits to eight or twelve subunits to investigate the role of PEG linker in improving reactivity.

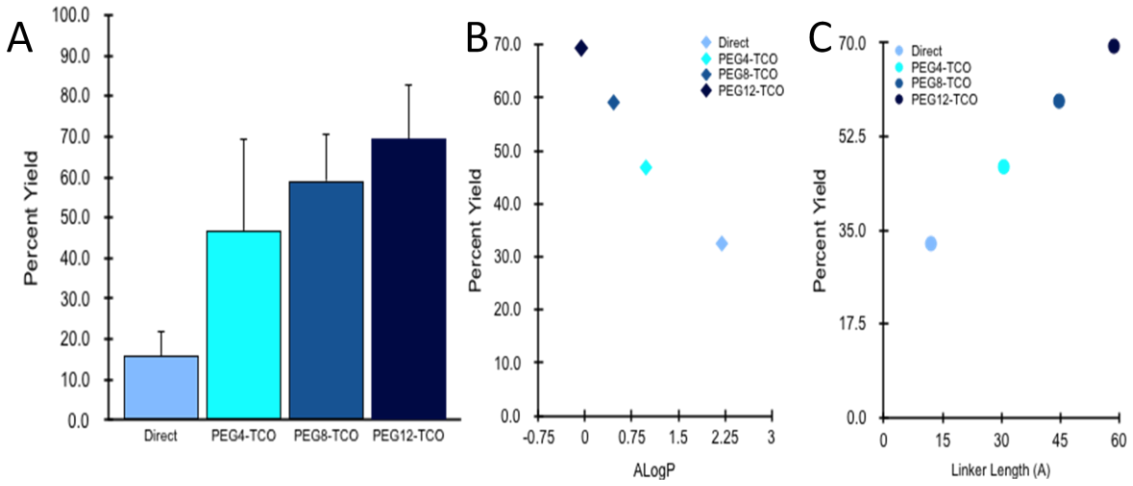

Figure 3.3 Antibody conjugation with NHS-PEGn-TCO linkers. (A) Percent reactive moieties out of total attachments for PEGn-TCO linkers, for n = 4, 8, and 12. (B) Percent reactive moieties out of total attachments as a function of AlogP values. (C) Perent reacive moieties out of total attachments as a function of linker length.

Longer PEG length resulted in an increased percent of functional modifications, greater than 70%. (Figure 3.3A) Moreover, the increase in reactivity correlated with the increased hydrophilicity (Figure 3.3B) as well as with increased linker length (Figure 3.3C). The hydrophilic PEG increases linker solubility which could result in more accessible moieties. Additionally, the PEG linker may provide a physical extension to increase accessibility of

the bioorthogonal reactant. The two features are not independent, so it is unclear if one or both components were responsible for the enhanced reactivity.

We also tested an amine-reactive valeric acid linker, whose alkly chains provide both linker length and a hydrophobic region to interact with antibody. TCO reactivity is enhanced to almost 60% when introduced in this manner (Figure 3.4A). Further increasing the hydrophobic region of this linker with decanoic acid-TCO does not result in further improvements in reactivity.

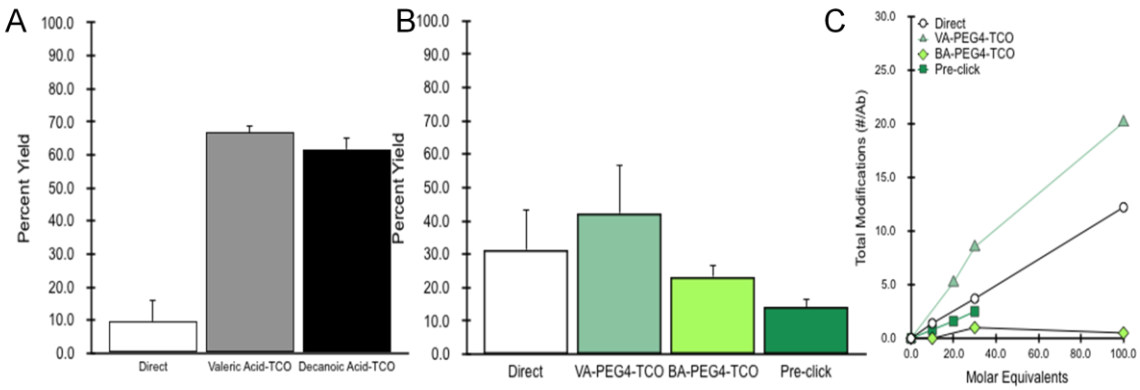

Figure 3.4 Antibody conjugation with alkyl chain and amphiphilic linkers. (A) Percent reactive moieties out of total attachments for valeric-acid TCO and decanoic-acid TCO linkers. (B) Percent reactie moieties out of total attachments for amphiphilic linkers. (C) Total attachment levels of amphiphilic linkers for given molar equivalents.

Neither PEG linkers nor alkyl chains enhanced reactivity of TCO to the same extent as the two-step coupling technique. It is possible that both hydrophobic and hydrophilic regions of the linker are necessary to achieve 100% TCO reactivity. To further investigate this hypothesis, we tested a series of amphiphilic linkers with a hydrophilic component distal to the TCO and a hydrophobic portion adjacent to the amine-reactive NHS, which mimic features of the original approach. The linkers included a valeric acid-PEG_4-TCO , benzoic acid-PEG_4-TCO, and a "pre-clicked" linker where amine-reactive azide and DBCO-

PEG_4-TCO were coupled in solution prior to antibody modification. Amazingly, this class of linkers performed as poorly or worse than the original carbamate linker (Figure 3.4B) However, these linkers had low modification efficiencies (Figure 3.4C), so it is possible that low measured reactivities are not reflective of linker function, but rather overall low number of total modifications. Their amphiphilic nature may influence low modification efficiencies; hydrophobic ends of the linker may interact to prevent antibody coupling.

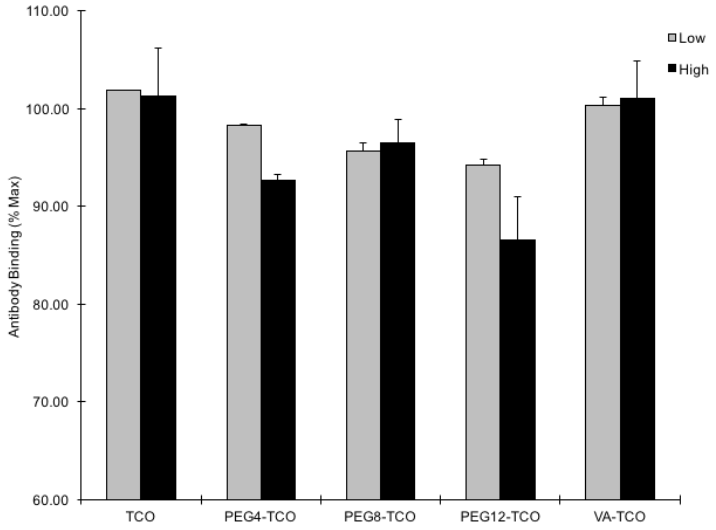

Figure 3.5 Relative binding of linker-modified antibodies. Antibody binding at 1 μg/mL, of linker-modified antibodies at low modification densities (2-3 attachments) and high modification densities (6-8 attachments), normalized to unmodified antibody at 1 μg/mL.

Finally, we tested to what extent these linkers interfered with antibody binding. Balancing enhanced reactivity with diminished antibody binding will be crucial for successful molecular detection strategies. We used an indirect competitive binding assay with SK-BR-3 cells to test binding. The binding of each linker-modified antibody was measured at low (2-3) and high (6-8) attachment levels. We previously determined that antibody binding is dramatically reduced when the number of reactive sites exceeds 8 (Chapter 2). We found that binding at 1 μg/mL, antibody concentration was unaffected for

most modified antibodies, retaining greater than 90% on binding compared to an unmodified antibody, even at high modification levels (Figure 3.5). Antibodies modified with PEG_{12}-TCO were the exception, with antibody binding reduced below 80% at high modification levels.

3.4 Discussion

In this work, we uncovered the extent of hydrophobic burying across several bioorthogonal reactants. We found that this problem was not specific to TCOs, but broadly applied to all bioorthogonal groups tested here. The degree of burying is likely related to hydrophobicity of the molecule. While the two-step, dual bioorthogonal coupling technique restores that majority of nonfunctional moieties, we explored one-step coupling strategies to prevent this inaccessibility. One-step modifications are less cumbersome and this simplicity would be beneficial for pretargeting strategies. While no one-step approach fully preserved functionality of modifications, both PEG and alkyl chain linkers distal to the reactant dramatically improved the percent of functional modifications. Importantly, while increases in linker length improved the number of reactive modifications, it also correlated with perturbed antibody binding. Thus, to enhance contrast in molecular detection strategies, both factors should be considered. However, not all hydrophobic burying may be bad. The extent of burying could be leveraged for stealth antibody-drug conjugates to cargo therapeutics into tumor cells.

Chapter 4

Exploring fluorescence lifetime properties of quantum dot-antibody conjugates for multiplexed molecular targeting

4.1 Introduction

Semiconductor nanocrystals, or quantum dots, are well-suited for multiplexed fluorescence imaging strategies because of their numerous advantageous properties. Quantum dots are brighter, more photostable, and display more narrow emission bands than organic fluorophores.[78] Consequently, quantum dots have the capacity to increase the number of simultaneous molecular targets and provide more quantitative reliable fluorescence signal than strategies that rely on organic dyes. In fact, the use of quantum dots as fluorescent labels for multi-target imaging has been widely explored,[24,80,132–134] successfully expanding the number of parallel detection channels possible. Quantum dot-based multiplexed imaging has been especially important for improving cancer diagnostic strategies, enabling simultaneous detection of multiple tumor microenvironment components[135] or clinically relevant cellular targets[136] to gain insight on key features associated with disease.

Quantum dots also exhibit long fluorescence lifetimes on the order of tens of nanoseconds[50], which is distinct from the lifetime of both organic fluorophores and cellular autofluorescence, typically 2-5 nanoseconds. It is possible to leverage the differences in lifetime to multiplex in the time domain. To date, lifetime multiplexing generally relies on the distinguishing different organic fluorophores, whose lifetimes are not sufficiently dissimilar to enable high-level multiplexing in the time domain. Though the long lifetime of quantum dots is attractive for fluorescence multiplexing, it has had limited adoption owing

to its complex multi-exponential decay kinetics[58] The phasor approach to fluorescence lifetime imaging (FLIM) simplifies lifetime analysis by transforming decay curves into its sine and cosine components for a graphical representation of lifetime.[66] Moreover, because this method is fit-free and does not rely on assigning exponentials to fluorescent species, multiplexing with quantum dots and other fluorescent probes is likely more straightforward. Quantum dot lifetimes are also tunable, varying with the material of its core and shell, as well as with shell thickness.[137] These features could be leveraged to dramatically increase the number of fluorescent species that can be time-resolved simultaneously.

To translate quantum dots for highly multiplexed fluorescence imaging, it will be necessary to first understand how the cellular environment influences quantum dot lifetime. For example, the multivalency of nanoparticle-antibody conjugates can drive receptor clustering and internalization[138–140] Additionally, conjugation to antibodies and localization to certain cellular compartments is known to alter lifetime behavior of some fluorescent species.[69]

In this work, we explore the fluorescence lifetime of quantum dots when used for molecular targeting. We find that quantum dot-antibody immunoconjugates exhibit characteristic long lifetimes in aqueous solution when analyzed using the phasor approach to FLIM. Interestingly, quantum dot immunoconjugates targeting cell surface receptors display slightly shorter lifetimes. We also uncover a fluorescent species inside cells as a consequence of targeting immunoconjugates to the cell surface, whose phasor location varies between the original quantum dot lifetime and a shorter, quenched lifetime depending on the laser excitation. The presence of this short lifetime species does not

depend on the surface marker targeted, nor the cell type labeled. This phenomenon occurs when utilizing quantum dots with different core properties, and with quantum dots emitting in different spectral windows. We suspect that this unique lifetime is a feature of quantum dot-quantum dot homoFRETing, and discuss ways to either mitigate this effect or leverage it to study certain biological processes.

4.2 Methods

4.2.1 Preparation of quantum dot immunoconjugates

Amine-terminated quantum dots emitting at 585 nm, 525 nm (Thermo Fisher Scientific), or 580 nm (Ocean NanoTech) were modified with NHS–tetrazine (Click Chemistry Tools) as described previously in Chapter 1. Briefly, quantum dots were first buffer-exchanged into PBS using Amicon Ultra-4 centrifugal devices. The reaction was performed using 0.8 nmoles of quantum dots and 500 equivalents of NHS–tetrazine in PBS containing 5% DMF and 0.01 M $NaHCO_3$ for 3 hours at room temperature. Tetrazine–quantum dots were purified into PBS using centrifugal filters. To prepare quantum dot immunoconjugates, 200 μg of anti-EpCAM (IgG_{2B}, clone 9C4, Biolegend), antiHER2 (Genentech), or non-binding control (mouse IgG1, clone MOPC-21, Biolegend) antibodies were first modified with 30 equivalents of amine-reactive *trans*-cyclooctene (TCO), (synthesized as previously reported[107]) in 0.5 mL PBS containing 10% DMF and 0.01 M $NaHCO_3$, buffer-exchanged using a Zeba spin desalting column, and reacted with 0.15 nmoles of tetrazine–quantum dots in 1 mL of PBS with 1 mg/mL BSA (PBS+) for 3 hours at room temperature. Quantum dot immunoconjugates were purified with Sephacryl S-400 (GE Healthcare) in PBS using an AKTA Pure FPLC (GE Healthcare). Final concentrations

were determined by absorption measurements using the quantum dot stock solution for calibration.

4.2.2 Characterization of fluorescence properties

Spectroscopic and lifetime characteristics of the QDot585-antibody conjugate were measured in solution at an approximate concentration of 100 nM. Emission spectra for QD585 was obtained using a FluoroMax-4 Spectrofluormeter. To determine the phasor position of the immunoconjugate, FLIM images of calibration solutions were captured with a laser scanning confocal microscope (FV1000, Olympus) at 20.0 μs/pixel acquisition speed, excited at an excitation wavelength of 534 nm. Emission between 550 nm and 660 nm was collected, and FLIM data was acquired using A320 FastFLIM FLIMbox. For calibrating the system, Rhodamine 110, with known lifetime of 4ns, was measured. The lifetime decay was transformed into phasor space using SimFCS software.

4.2.3 Cell culture

The following cancer cell lines were obtained from ATCC: SK-BR-3, NCI-H1650, A431, and PANC-1. Cells were cultured in flasks at 37 °C with 5% CO_2. SK-BR-3 cells were grown in McCoy's 5A media; NCI-H1650 cells were grown in RPMI-1640 media; and A431 and PANC1 cells were grown in DMEM. All media was supplemented with 10% fetal bovine serum, 5% penicillin/streptomycin, and 5% L-glutamine. Cells were subcultured after reaching confluency by treatment with trypsin–EDTA.

4.2.4 Cell labeling

Prior to imaging experiments, cells were seeded in Lab-Tek slide chambers and grown to 90% confluency. Quantum dot immunoconjugates were used for staining at saturating concentrations (as determined by kinetic analysis, see Chapter 5).

For live cell staining, cells were washed three times with PBS containing 1 mg/mL BSA (PBS+), incubated with quantum dot immunoconjugates for 30 minutes, and subsequently washed three times with ice cold PBS+.

For fixed and permeabilized staining, cells were washed three times with PBS, followed by addition of a 1:1 mixture of PBS and Fix Buffer 1 (BD Biosciences) and incubated at room temperature for 20 minutes. Cells were washed three times with Perm/Wash buffer containing 1% BSA (PW+, BD Bioscience), followed by a wash with PBS, not containing saponin to reverse some permeabilization. Cells were then incubated with quantum dot immunoconjugates for 30 minutes, and subsequently washed three times with ice cold PBS+.

For fixed cell staining, cells were washed three times with PBS. Next, cells were fixed with 4% paraformaldehyde incubated at room temperature for 20 minutes. After three washes with PBS, cells were targeted with quantum dot immunoconjugates, incubated for 30 minutes, and washed three more times with PBS+.

4.2.5 FLIM imaging

Cells were stained as described above. Fluorescence signal and lifetime images were obtained using a laser scanning confocal microscope with a 60x water immersion objective lens and 20 MHz Fianium laser, at a 20.0 μs/pixel acquisition speed, exciting at either an excitation wavelength of 470 nm or 534 nm. Emission was collected in one of the following emission windows: 505-525 nm, 505-605 nm, or 550 nm and 660 nm. Fluorescence images were captured using Fluoview software. FLIM data was acquired using A320 FastFLIM FLIMbox. For each image, 50 frames were collected for FLIM analysis. Rhodamine 110, with

known lifetime of 4 ns, was measured to calibrate the FLIM system. The lifetime decay was transformed into phasor space and analyzed using SimFCS software.

4.3 Results

We first identified the characteristic lifetime properties of quantum dots emitting at 585 nm, QD585, in aqueous solution (Figure 4.1). Analyzed using the phasor approach, QD585 displayed a long lifetime, which was expected for quantum dot probes. We utilized this lifetime phasor cluster as a reference to compare the measured lifetimes of subsequent cell-based measurements.

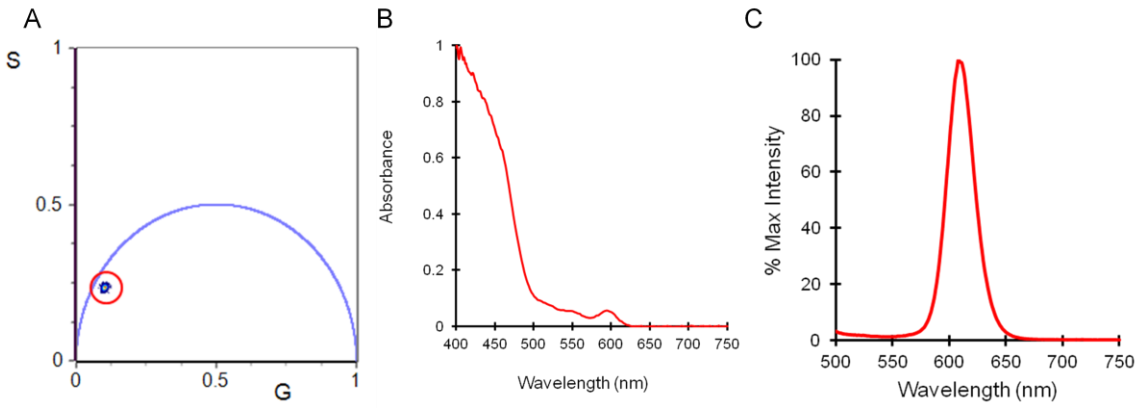

Figure 4.1 Spectroscopic properties of quantum dots. A. Lifetime value of QD585, displayed graphically via phasor analysis, with 20 MHz laser frequency. Absorbance (B) and emission (C) spectra of QD585.

Next, we targeted the surface receptor EpCAM on live SK-BR-3 breast cancer cells using a QD585 immunoconjugate to determine whether lifetime properties of QD585 are altered when used for molecular targeting. Owing to the broad absorption of QD585 at lower wavelengths (Figure 4.1B), we excited cells at 470 nm and measured intensity and lifetime via FLIM (Figure 4.2A-B). The resulting phasor map was similar to the phasor cluster of QD585 in solution, with noteworthy differences. Namely, several pixels display a slightly shorter lifetime.

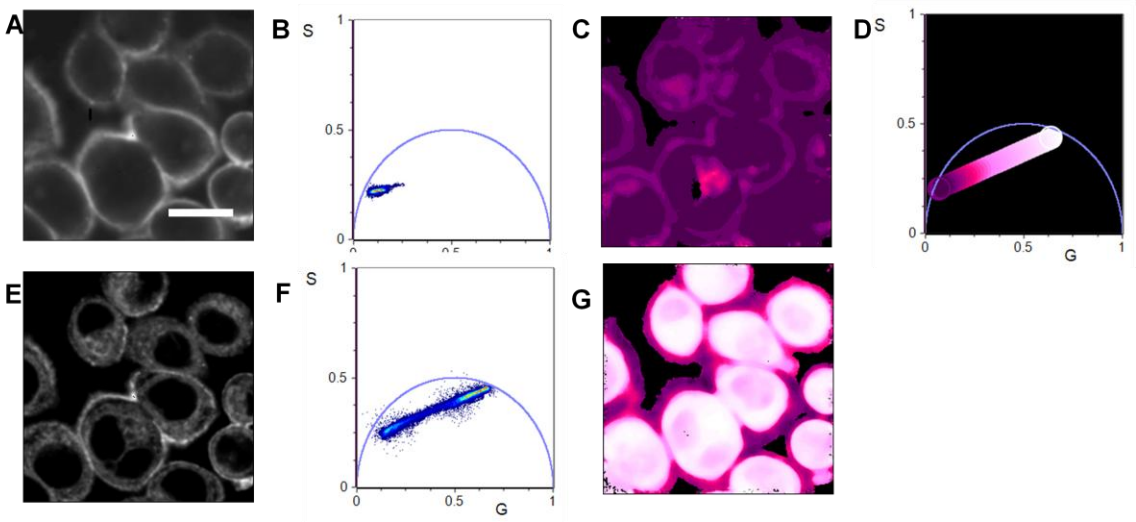

Figure 4.2 Live SK-BR-3 cells targeted with anti-EpCAM-QD585 immunoconjugates. SK-BR-3 cells targeted for cell surface EpCAM with a QD585 probe were excited at 470 nm (A-C) or 534 nm (E-G). Intensity images (A, E) and corresponding phasor plots at 20 MHz laser frequency (B, F) of labeled cells. (C, G) FLIM images painted according to relative fractional contribution of QD585 and short lifetime species, where the line from purple-to-white (D) corresponds to 100% QD585 (purple), 100% short lifetime species (white), and all possible mixtures in between. Scale bar = 20 µm. Laser frequency is 20 MHz.

For use of quantum dot probes in a lifetime-based multiplexing scenario with organic fluorophores will require excitation of sample at longer wavelengths. This is because the Stokes shift of organic fluorophores is not as large as the quantum dot shift. Thus, we also excited cells at 534 nm (Figure 4.2. D-E). The phasor plot corresponding to cells excited at 534 nm had a unique phasor map compared to the map generated at 470 nm excitation. The phasor approach to FLIM follows linear vector math; thus pixels containing two fluorescent species will fall along the line that joins the lifetime location of the two pure species. The exact location along the line depends on the intensity-weighted contribution of each species. It is apparent that when cells are excited at 534 nm, several pixels in the image contain a combination of two fluorescent species, the true QD585 conjugate lifetime and a shorter lifetime species (Figure 4.2E). We exploited the reciprocal

nature of the phasor approach to map points on phasor plot to their corresponding pixels in the image. This technique enabled visualization fluorescent lifetimes to their subcellular regions. We utilized a color map (Figure 4.2D) to paint the image according to the fractional contribution of both lifetime species. The majority of pixels containing high relative amount of shorter lifetime species are located inside the cell (Figure 4.2G). Interestingly, we observed these same pixels exhibit a high relative amount of long lifetime species at lower excitations (Figure 4.2C) Figure 4.3 highlights this feature.

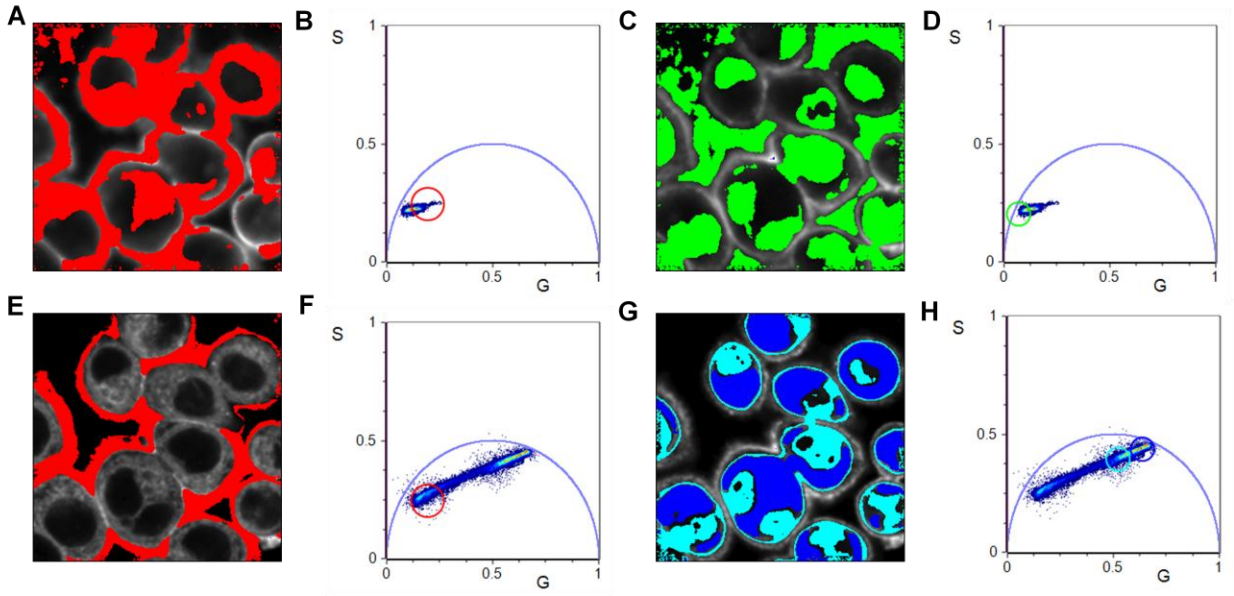

Figure 4.3 Phasor analysis of EpCAM-targeted SK-BR-3 cells. SK-BR-3 cells targeted for cell surface EpCAM with a QD585 probe were excited at 470 nm (A-C) or 534 nm (E-G). Phasor cluster corresponding to the lifetime of QD585 at the surface of cells is circled in red (B, F) and mapped back to the FLIM image (A,E) Pixels associated with intracellular regions of the cell map to a long lifetime cluster when excited at 470 nm, colored in green (C, D). However, same intracellular regions map to shorter lifetime values when excited at 534 nm, colored in cyan and blue (G, H). Laser frequency is 20 MHz.

When cells are excited at lower excitation wavelength, the positive surface receptor stain has a slightly shorter lifetime than the QD585 probe in solution (Figure 4.3 A-B), which is likely due high density of targeted EpCAM causing quantum dot quenching. Pixels corresponding to the true QD585 lifetime are mapped in green (Figure 4.3C-D) to regions

outside the cell (nonspecific background) and intracellular regions. For cells excited at longer excitation wavelengths, the lifetime value for surface marker stain was essentially unchanged (Figure 4.3E-F). However, pixels that once clustered at long lifetime locations at lower excitations, mapped closer toward shorter lifetime species, illustrated by cyan and blue clusters in Figure 4.3G-H).

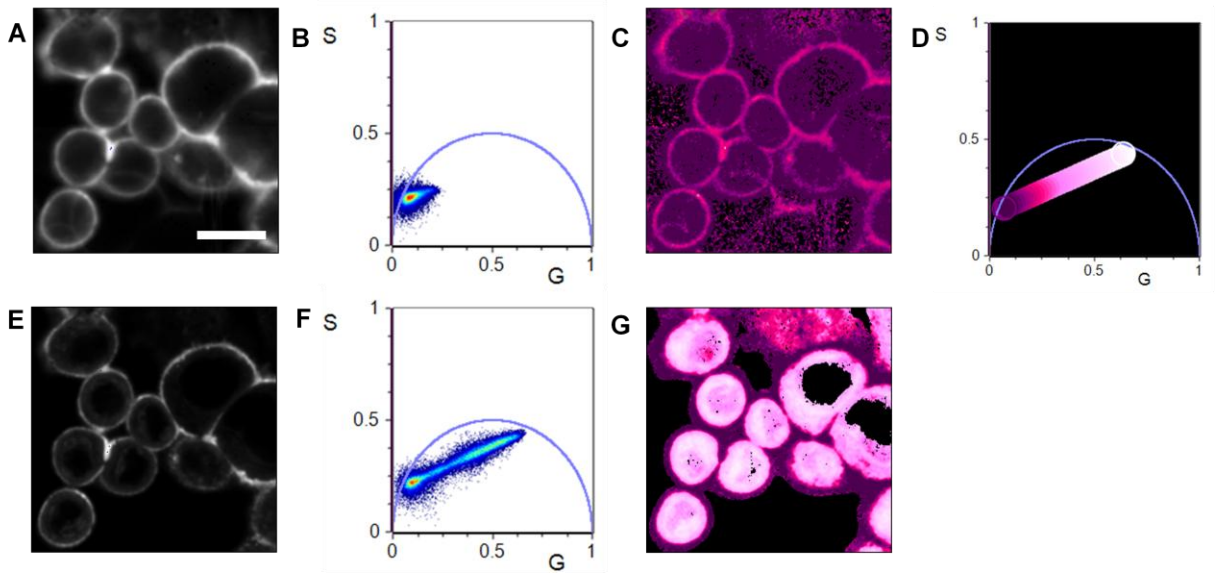

Figure 4.4 Live SK-BR-3 cells targeted with anti-HER2-QD585 immunoconjugates. SK-BR-3 cells targeted for cell surface HER2 with a QD585 probe were excited at 470 nm (A-C) or 534 nm (E-G). Intensity images (A, E) and corresponding phasor plots (B, F) of labeled cells. (C, G) FLIM images painted according to relative fractional contribution of QD585 and short lifetime species, where the line from purple-to-white (D) corresponds to 100% QD585 (purple), 100% short lifetime species (white), and all possible mixtures in between. Scale bar = 20 μm, laser frequency is 20 MHz.

To determine whether the presence of the shorter lifetime species was specific to EpCAM targeting, we created quantum dot immunoconjugates targeting HER2. However, as illustrated in Figure 4.4, this unique lifetime pattern persisted. Moreover, staining cells with a quantum dot conjugated to a nonbinding control antibody also resulted in a short lifetime species at 534 nm excitation (Figure 4.5), displaying minimal fractional contribution from the true QD585 lifetime, likely because the nonbinding control antibody

did not yield substantial surface targeting. To illustrate that this fluorescence lifetime is not related to cellular autofluorescence, we measured the intensity and lifetime of unstained cells excited at 534 nm (Figure 4.5 E-F). Unstained cells did not contain this shorter lifetime species, indicating that it may be specifically related to molecular targeting with quantum dot probes.

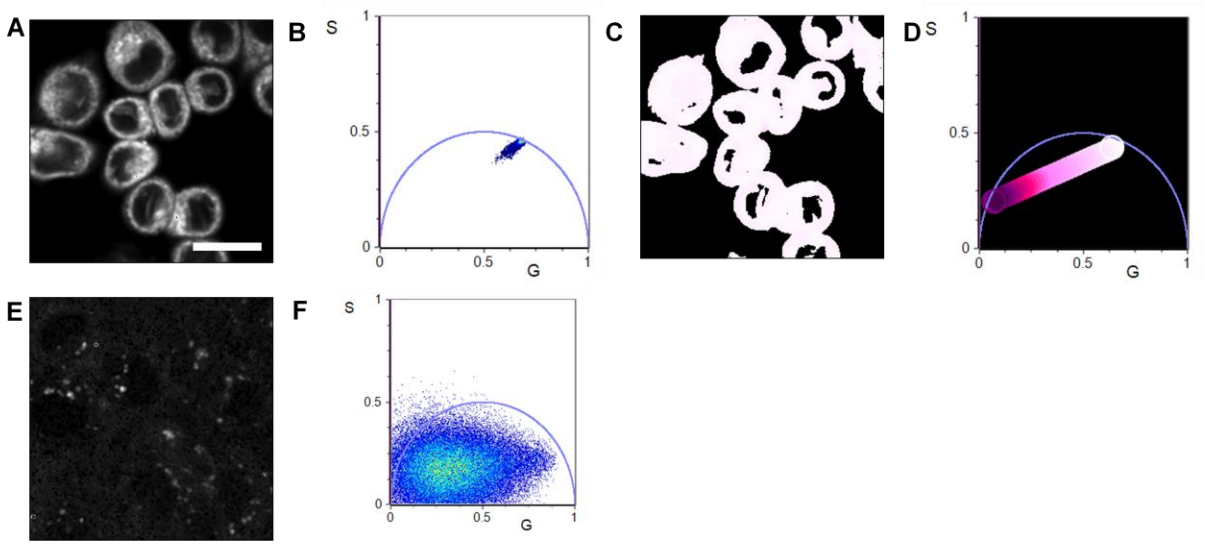

Figure 4.5 Live SK-BR-3 cells targeted with nonbinding control-QD585 immunoconjugates. SK-BR-3 cells targeted with a QD585 probe modified with nonbinding control antibody were excited at 534 nm. (A-C) Intensity images (A) and corresponding phasor plot (B) from cells. (C) FLIM image painted according to relative fractional contribution of QD585 and short lifetime species, where the line from purple-to-white (D) corresponds to 100% QD585 (purple), 100% short lifetime species (white), and all possible mixtures in between. (E) Intensity image and phasor plot (F) of live, unstained SK-BR-3 cells excited at 534 nm. Scale bar = 20 μm. Laser frequency is 20 MHz.

We supposed that this phenomenon could be related to nanoparticle internalization, as cellular uptake of functionalized quantum dots is known to occur, both from active and passive processes.[141] To discern whether this unique lifetime was a feature specific to receptor-mediated endocytosis, such as the distinct low pH environment of endosomes, or more general, we targeted EpCAM with QD585 immunoconjugates onto fixed, semi-permeabilized cells. Thus, immunoconjugates could feasibly enter intracellular regions, but

active internalization processes were mitigated. Despite fixation, we observed the presence of short lifetime species inside cells (Figure 4.6), suggesting active uptake is not necessary.

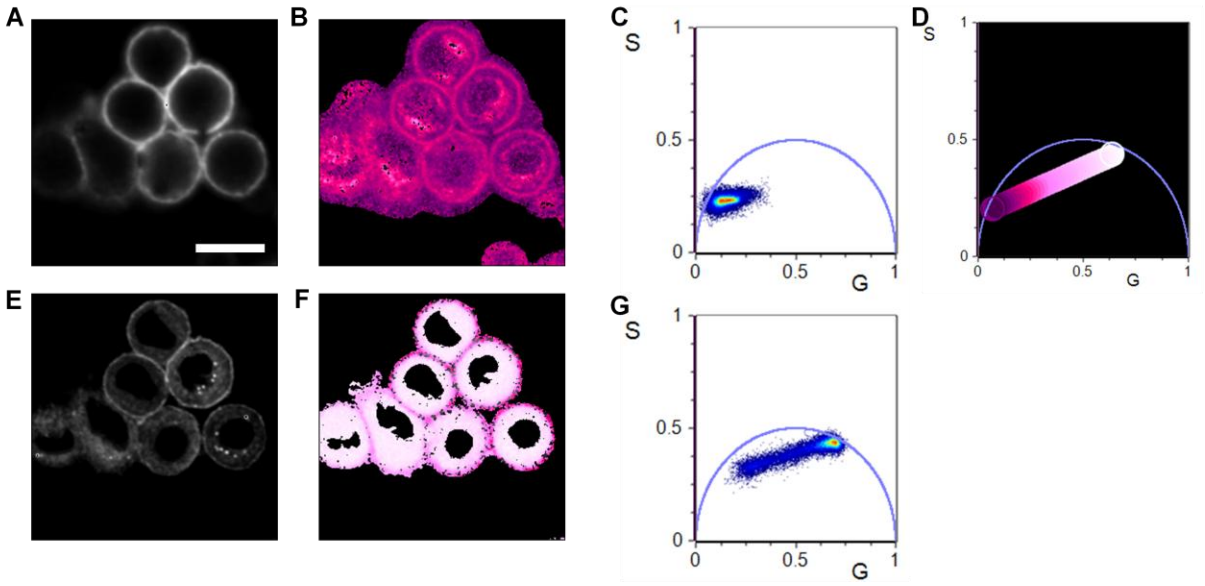

Figure 4.6 Fixed and permeabilized SK-BR-3 cells targeted with anti-EpCAM-QD585 immunoconjugates. SK-BR-3 cells targeted for cell surface EpCAM with a QD585 probe were excited at 470 nm (A-C) or 534 nm (E-G). Intensity images (A, E) and corresponding phasor plots (B, F) of labeled cells. (C, G) FLIM images painted according to relative fractional contribution of QD585 and short lifetime species, where the line from purple-to-white (D) corresponds to 100% QD585 (purple), 100% short lifetime species (white), and all possible mixtures in between. Scale bar = 20 µm. Laser frequency is 20 MHz.

Nanoparticle internalization can vary substantially between different cell types.[139] Thus, we targeted EpCAM on the surface of live NCI-H1650 cells to determine whether this observation was simply a product of inherent internationalization rates of SK-BR-3 cells. However, NCI-H1650 cells displayed similar lifetime patterns (Figure 4.7) as SK-BR-3 cells, suggesting this occurrence may be generalized to numerous cell types.

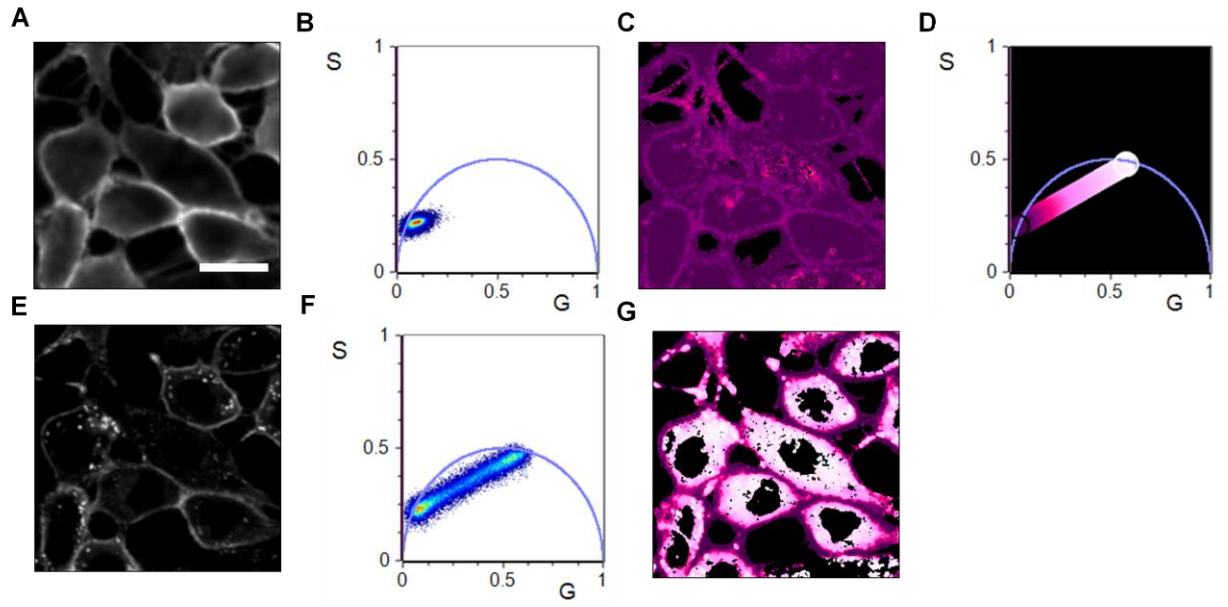

Figure 4.7 Live NCI-H1650 cells targeted with anti-EpCAM-QD585 immunoconjugates. NCI-H1650 cells targeted for cell surface EpCAM with a QD585 probe were excited at 470 nm (A-C) or 534 nm (E-G). Intensity images (A, E) and corresponding phasor plots (B, F) of labeled cells. (C, G) FLIM images painted according to relative fractional contribution of QD585 and short lifetime species, where the line from purple-to-white (D) corresponds to 100% QD585 (purple), 100% short lifetime species (white), and all possible mixtures in between. Scale bar = 20 µm. Laser frequency is 20 MHz.

To ensure that this short lifetime species was not related to the specific quantum dot used, we also measured lifetime after targeting with a different quantum dot probe, which displays similar emission characteristics but has a shorter lifetime. The different lifetime properties of this quantum dot may be attributed to either differences in synthesis or coating shell thickness. While the true quantum dot lifetime and shorter lifetime species shifted, the overall trend was consistent with measurements obtained from the original QD585 probe (Figure 4.8).

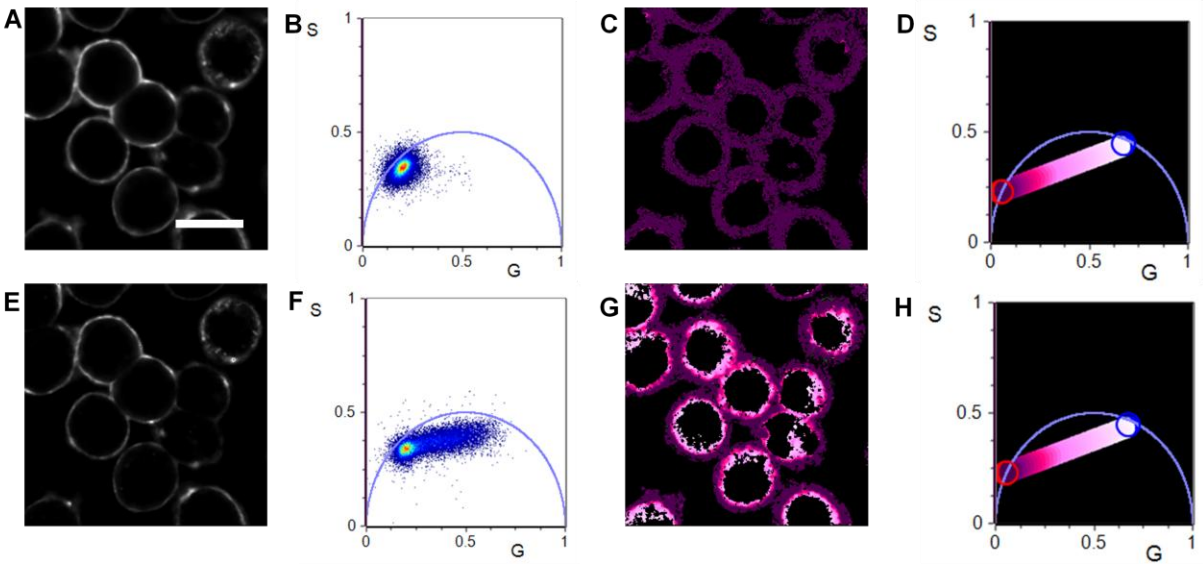

Figure 4.8 Live SK-BR-3 cells targeted with anti-EpCAM-QD580 immunoconjugates from Ocean Nanotech. SK-BR-3 cells targeted for cell surface EpCAM with a QD585 probe were excited at 470 nm (A-C) or 534 nm (E-G). Intensity images (A, E) and corresponding phasor plots (B, F) of labeled cells. (C, G) FLIM images painted according to relative fractional contribution of QD580 and short lifetime species, where the line from purple-to-white (D) corresponds to 100% QD580 (purple), 100% short lifetime species (white), and all possible mixtures in between. Scale bar = 20 μm. Laser frequency is 20 MHz.

It is possible that quantum dot immunoconjugates emitting between 575-610 nm interact with endogenous fluorescent species when internalized into cells, potentially in a FRET scenario where the internalized immunoconjugates acts as a donor to excite an intrinsic fluorescent species in close proximity. To further study this possibility, we utilized quantum dots with an emission peak at 525 nm, QD525, to create an antiEpCAM immunoconjugate and targeted these probes to live SK-BR-3 cells. (Figure 4.9) Both emission and lifetime properties of quantum dots can be tuned with size.[142] Consequently, we expected the lifetime of green-emitting quantum dot immunoconjugates to be slightly shorter than their red-emitting counterparts. Indeed, when cells are excited at 470 nm, the resultant lifetime cluster of QD525 targeted to the surface of cells was slightly shorter than when targeted with QD585 (Figure 4.9 A-B). Importantly, we still observed pixels with contribution from shorter lifetime species that mapped to intracellular regions of cells

(Figure 4.9). Interestingly, the lifetime location of the shorter species also shifts slightly with QD525 compared to QD585. Moreover, the intensity-weighted fractional contribution of the shorter lifetime species increased as we shifted to further red detection windows.

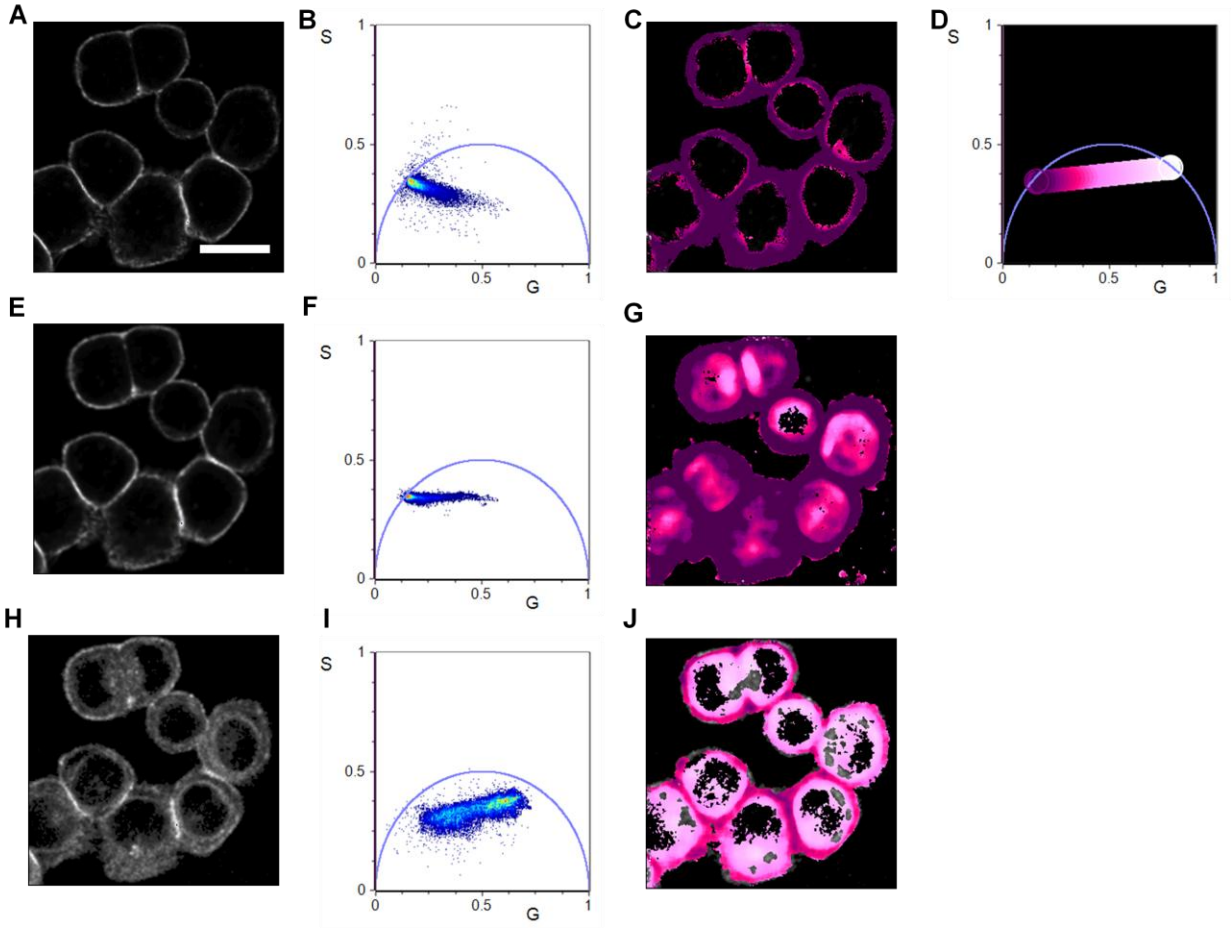

Figure 4.9 Live SK-BR-3 cells targeted with anti-EpCAM-QD525 immunoconjugates. SK-BR-3 cells targeted for cell surface EpCAM with a QD525 probe were excited at 470 nm, and emission was collected between 500-525 nm (A-C), 505-605 nm (E-G), and 560-660 (H-J) Intensity images (A, E, H) and corresponding phasor plots (B, F, I) of labeled cells. (C, G, J) FLIM images painted according to relative fractional contribution of QD525 and short lifetime species, where the line from purple-to-white (D) corresponds to 100% QD525 (purple), 100% short lifetime species (white), and all possible mixtures in between. Scale bar = 20 μm. Laser frequency is 20 MHz.

From this information, we speculated that this phenomenon is likely due to quantum dot-quantum dot homeFRETing. Since particle size dictates emission, even small a size dispersity in a population of quantum dots can cause homoFRETing. Additionally the degree of quenching that occurs varies with the degree of quantum dot clustering. In fact,

the variation in quenching has been exploited to observe the assembly of nanostructures.[143] Differing degrees of quantum dot quenching can also explain why the phasor location of the quenched lifetime shifts slightly for regions inside the cell compared to quenching at the surface. We also observed that quenched species was red-shifted (Figure 4.9) which is a characteristic feature of quenching.

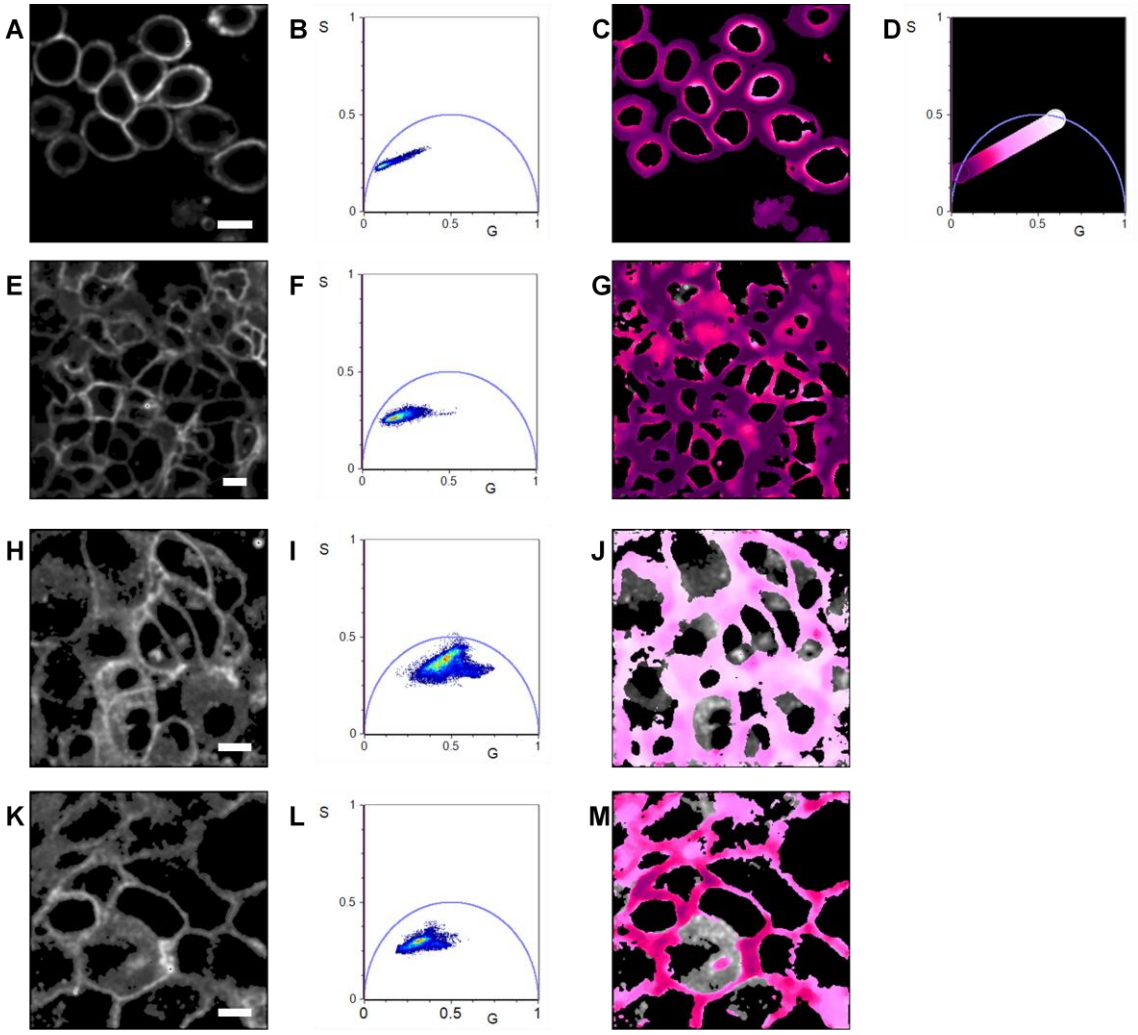

Figure 4.10 anti-EpCAM-QD585 immunoconjugates targeted to several fixed cell lines. SK-BR-3 (A-C), NCI-H1650 (E-G), PANC1 (H-J), and A431 (K-M) cells targeted for cell surface EpCAM with a QD585 probe were excited at 534 nm. Intensity images (A, E, H,K) and corresponding phasor plots (B, F, I, L) of labeled cells. (C, G, J, M) FLIM images painted according to relative fractional contribution of QD585 and short lifetime species, where the line from purple-to-white (D) corresponds to 100% QD585 (purple), 100% short lifetime species (white), and all possible mixtures in between. Scale bar = 20 μm. Laser frequency is 20 MHz.

Finally, we fixed several cell lines, without intentional permeabilization, to prevent quantum dot immunoconjugates from internalizing upon EpCAM targeting. For SK-BR-3 and NCI-H1650 cells (Figure 4.10A-G) the location of the phasor was mostly dominated by longer lifetime species. While for A431 and PANC-1 cells, the relative fractional contribution of quenched species was much higher, despite still being localized to the surface of cells. This could potentially be attributed to the varying amount of EpCAM surface receptor expression or degree of clustering between cell lines.

4.4 Discussion

We explored the lifetime properties of quantum dots targeted onto cells in an effort to take advantage of their unique features for multiplexed molecular profiling. We uncovered that internalization of quantum dots leads to a unique short lifetime species that is clearly observed by phasor analysis. It is possible that the presence of this short lifetime is related to quantum dot-quantum dot homoquenching. The intensity-weighted fractional contribution of quenched particles is more apparent at longer excitations. We believe this could arise because quantum dots are less optimally excited at longer wavelengths (Figure 4.1B). Thus, at shorter wavelengths quantum dot emission may still be dominated by direct excitation, but this balance shifts with less optimal wavelengths. Future work will discern the exact mechanism for excitation wavelength dependency.

There are two perspectives with which to look at this homoquenching phenomenon. The first is to explore strategies that mitigate this effect for time-resolved fluorescence multiplexing. Staining cold to reduce active internalization could lessen the amount of quenched species present. Additionally, the multivalent nature of quantum dot immunoconjugates drives internalization rates by inducing receptor clustering. Thus,

quantum dot targeting in a two-step approach, where antibodies first bind to target molecules followed by quantum dot attachment, could also reduce the degree of clustering, and therefore homoquenching. Two-step targeting techniques can also amplify signal of low-level expression markers (Chapter 2), which would be an added benefit to this technique. Secondly, we can potentially exploit quantum dot homoquenching to internalization and clustering behavior of cells. For example, future work will study whether subtle lifetime changes exist between quantum dots sequestered in different intracellular compartments. This could also be leveraged as a tool to study activation-induced clustering in immune cells.

Chapter 5

Multiplexed molecular profiling using the phasor approach to FLIM

5.1 Introduction

Tumors are heterogeneous and complex, consisting of ecosystems of diverse cell types with spatiotemporal dynamics[6] This disease complexity drives tumor progression; therefore, characterizing the heterogeneity is necessary to enhance diagnostics and therapeutic treatment of cancer. Indeed, genomic and transcriptomic interrogation of tumors enabled insights into the considerable tumor diversity. These strategies uncovered several distinct molecular subtypes of tumors within the same tissue of origin, each with unique phenotype and prognosis that expanded on classical subtypes[33,144–146] Recent advancements in single cell genomics techniques[34–37,147] further tease apart individual cell contribution to overall disease state, including the contribution of rare subpopulations to tumor evolution and metastasis.[39,42,43,148–150] The implications of characterizing heterogeneity in cancer are profound: it provides a more thorough understanding of tumor development and reveals gene signatures that can be leveraged for predictive outcomes and improved therapeutic design.

While genetic analysis is useful, it is incomplete without spatial context and profiling of functional molecules, such as proteins. Spatial information and phenotypic analysis can capture distinct neighborhoods of tumor and stromal cells in their microenvironment,[45,151] whose dynamic and reciprocal communication likely influence disease states.[152–155] Capturing this interplay has diagnostic value, as unique cellular organizations and interactions may be affiliated with tumor grade.[156] Thus, single cell analysis that exploits

spatial information while acquiring molecular features will be critical to understanding tumor heterogeneity.

This type of comprehensive molecular profiling will require a high degree of multiplexing capability to complement the analysis achieved in omics strategies. While immunofluorescence acquires cellular morphology and microenvironment features, [48,49] this technique cannot fully characterize the complexity of the tumor due to multiplexing limitations. The use of narrow emission quantum dots[50,51,82] and hyperspectral imaging strategies[44,52,157] offer only modest gains in multiplicity for immunofluorescence. Recent advancements such as cyclic immunofluorescence,[24,53,54] and mass spectrometry-based techniques overcome this multiplexing barrier[40,55], enabling resolution of over 32 species in some instances, but require either expensive instrumentation, large time costs, or both.

In this work, we propose a fluorescence lifetime-based approach that dimensionally increases the parallel detection feasible with immunofluorescence with limited additional instrumentation and time requirements. Fluorescence lifetime is the duration of fluorescence emission following excitation. Provided that the fluorescent probes have distinct lifetimes, this property can be exploited to distinguish several probes within the same spectral window, multiplicatively increasing the number of species that can be resolved. With advancements in instrumentation,[63] performing lifetime analysis is a simple, inexpensive addition to conventional laser scanning microscopes. Moreover, this technique could be performed in concert with cycling immunofluorescence and hyperspectral imaging protocols for extreme multiplexing capabilities.

Attempts at time-resolved fluorescence imaging previously required complex fitting strategies, pattern matching techniques, or were dependent on the addition of spectral

information to unmix fluorescent probes.[69,158]The phasor approach to fluorescence lifetime imaging (FLIM) greatly simplifies lifetime analysis. Fluorescence decay at each pixel of an image undergoes a Fourier transform, and the resultant sine and cosine transforms are plotted on the phasor plot, such that distinct fluorescence lifetimes have unique locations on the phasor plot. This simple graphical representation makes it feasible to distinguish numerous fluorescence lifetimes visually, without fit or *a priori* information.[66,70] For multi-component fluorescence images, simple geometric analysis can be used to determine the relative probe content at each pixel of an image. Together with total signal, intensity from each fluorescent species at every pixel can be retrieved, thus enabling lifetime-based multiplexed analysis. The utility of this approach hinges on fluorescent probes displaying unique lifetime values. Most organic fluorophores exhibit short lifetimes, less than 5 nanoseconds, without much diversity. The use of nanomaterial probes like quantum dots are well-suited for time-resolved fluorescence. Not only do quantum dots display narrow emission bands for facile spectral imaging, they exhibit long, tunable lifetimes that can be readily distinguished from the lifetime of organic fluorophores.

In this work, we demonstrate that the phasor approach to FLIM can be used for highly multiplexed, single cell imaging. We show that three spectrally-matched probes display distinct lifetimes when mapped on the phasor plot. The lifetime values of these fluorescent probes are reproducible when probes are subject to the cellular environment. Moreover, when all three probes are targeted to spatially distinct subcellular regions, fluorescent contribution from each species is trivial to discriminate. Owing to the linear properties of the phasor approach, spatially overlapping regions that contain two or three fluorescent species simultaneously are simple to deconstruct on lifetime properties alone.

We utilize this powerful technique to target three surface markers simultaneously, and extract expression levels for each marker. Furthermore, by utilizing calibration solutions of each fluorescent probe, this technique has the capacity to transform the unmixed intensity into absolute concentration measurements. The added dimensionality that phasor FLIM offers has the potential to extend multiplexing of conventional immunofluorescence to greater than 20 probes concurrently.

5.2 Methods

5.2.1 Preparation of fluorophore-antibody conjugates

Anti-Ki67 (IgG_1, clone B56, BD Biosciences), anti-TfR (IgG_1, clone 29806, R&D Systems), anti-Cytokeratin (IgG_1, clone C-11, Biolegend), anti-E-Cadherin (IgG_1, clone 67A4, Biolegend) and nonbinding control antibodies (mouse IgG1, clone MOPC-21, Biolegend) were buffer-exchanged into PBS using Zeba spin desalting columns (Thermo Fisher Scientific) prior to modification. Fluorophore-antibody conjugates were prepared by reacting 200 μg of antibody with 10 equivalents of NHS–Bodipy-TMR (Thermo Fisher Scientific) or 100 equivalents of NHS-Rhodamine (Thermo Fisher Scientific). The reaction took place in 0.5 mL PBS containing 10% DMF and 0.1 M $NaHCO_3$ (pH 8.5) for 3 hours at room temperature. Fluorophore-modified antibodies were purified using Zeba spin desalting columns. Antibody and dye concentration were determined by absorption measurements recorded on a Thermo Scientific NanoDrop 2000 spectrophotometer. Degree of labeling, measured by absorption, was approximately 1-3 dyes/antibody for each conjugate.

5.2.2 Preparation of quantum dot immunoconjugates

Amine-terminated quantum dots (Thermo Fisher Scientific) were modified with NHS–tetrazine (Click Chemistry Tools) as described previously in Chapter 2. Briefly, quantum dots were first buffer-exchanged into PBS using Amicon Ultra-4 centrifugal devices. The reaction was performed using 0.8 nmoles of quantum dots and 500 equivalents of NHS–tetrazine in PBS containing 5% DMF and 0.01 M $NaHCO_3$ for 3 hours at room temperature. Tetrazine–quantum dots were purified into PBS using centrifugal filters. To prepare quantum dot immunoconjugates, 200 µg of anti-EpCAM (IgG_{2B}, clone 9C4, Biolegend) antibody was first modified with 30 equivalents of amine-reactive *trans*-cyclooctene (TCO), in 0.5 mL PBS containing 10% DMF and 0.01 M $NaHCO_3$, buffer-exchanged using a Zeba spin desalting column, and reacted with 0.15 nmoles of tetrazine–quantum dots in 1 mL of PBS with 1 mg/mL BSA (PBS+) for 3 hours at room temperature. Quantum dot immunoconjugates were purified with Sephacryl S-400 (GE Healthcare) in PBS using an AKTA Pure FPLC (GE Healthcare). Final concentrations were determined by absorption measurements using the quantum dot stock solution for calibration.

5.2.3 Cell culture

Human lung cancer cell line NCI-H1650 cells were obtained from ATCC. Cells were cultured in flasks at 37 °C with 5% CO_2. NCI-H1650 cells were grown in RPMI-1640 media containing 10% fetal bovine serum, 5% penicillin/streptomycin, and 5% L-glutamine and subcultured after reaching confluency by treatment with trypsin–EDTA.

5.2.4 Characterization of fluorescence properties

Spectroscopic and lifetime characteristics of each fluorescent probe were measured in solution at an approximate concentration of 100 nM. Emission spectra for each

fluorescent species was obtained using a FluoroMax-4 Spectrofluormeter. To determine the phasor position of the pure fluorescent species, FLIM images of calibration solutions were captured with a laser scanning confocal microscope (FV1000, Olympus) at 20.0 μs/pixel acquisition speed, excited at 534 nm. Emission between 550 nm and 660 nm was collected, and FLIM data was acquired using A320 FastFLIM FLIMbox. For calibrating the system, Rhodamine 110, with known lifetime of 4ns, was measured. The lifetime decay was transformed into phasor space using SimFCS software.

5.2.5 Kinetic analysis of antibody conjugates

The kinetic analysis of antibody conjugates was performed to determine saturating concentrations to use for subsequent cell imaging procedures. The lowest saturating concentration is desired to efficiently target all biomarkers, yet minimize background signal. NCI-H1650 cells (250,000 cells/sample) were labeled with antibody conjugates or nonbinding conjugate controls at concentrations ranging from 0.01 to 50 nM in 100 μl PBS+ for 30 minutes at room temperature. Cells were washed 3 times by centrifugation with ice-cold PBS+. Fluorescence signal was assessed using an Attune NxT cytometer (Thermo Fisher Scientific) and analyzed using Flowjo software.

5.2.6 Cell staining

Prior to imaging experiments, NCI-H1650 cells were seeded in Lab-Tek slide chambers and grown to 90% confluency. Targeted fluorescent probes were used at saturating concentrations (as determined by kinetic analysis).

To stain cells with both surface and intracellular markers, cells were first targeted for surface markers in PBS+ for 30 minutes, on ice to prevent nanoparticles internalization. Samples were washed three times with PBS, fixed and permeabilized using a 1:1 mixture of

PBS and Fix Buffer 1 (BD Biosciences) and incubated at room temperature for 20 minutes. Cells were washed three times with Perm/Wash buffer containing 1% BSA (PW+, BD Bioscience), and subsequently stained for intracellular markers for 15 minutes in PW+. Finally, cells were washed three times with PW+. Saponin-based permeabilization was then reversed with use of PBS not containing saponin.

Cells stained for surface markers only were first fixed with 4% paraformaldehyde incubated at room temperature for 20 minutes. After three washes with PBS, cells were targeted with antibody conjugates, incubated for 30 minutes on ice, and washed three more times with PBS+.

5.2.7 Confocal and FLIM imaging

NCI-H1650 cells were stained as described above. Fluorescence signal and lifetime images were obtained using a laser scanning confocal microscope with a 60x water immersion objective lens and 20 MHz Fianium laser, at a 20.0 μs/pixel acquisition speed, exciting at 534 nm Emission was collected between 550 nm and 660 nm. For fluorescent species that emit in the green spectral window, sample was excited at 470 nm, and emission was collected between 505 nm and 605 nm. Fluorescence images were captured using Fluoview software. FLIM data was acquired using A320 FastFLIM FLIMbox. For each image, 50 frames were collected for FLIM analysis. Rhodamine 110, with known lifetime of 4 ns, was measured to calibrate the FLIM system. The lifetime decay was transformed into phasor space and analyzed using SimFCS software and ImageJ.

5.3 Results

We first demonstrated that the lifetime values of spectrally- matched probes could be resolved in phasor space. As illustrated in Figure 5.1A, the quantum dot, QD585, and

organic fluorophores Bodipy-TMR and Rhodamine in aqueous solution, emit fluorescence between 575-610 nm. These 3 probes also have distinct fluorescence lifetimes, ranging from just a few nanoseconds to tens of nanoseconds. Though decay curves for each probe individually likely can be distinguished, mixtures of these probes will be difficult to resolve, especially given quantum dots exhibits multi-exponential decays. The phasor representation surmounts this challenge by avoiding exponential assignment altogether, and simply relying on the location of the phasor cluster when plotted in phasor space. Fortunately, the fluorescence lifetime of these three probes can be easily resolved using phasor analysis. Each of these probes has a unique location on the phasor plot (Figure 5.1B).

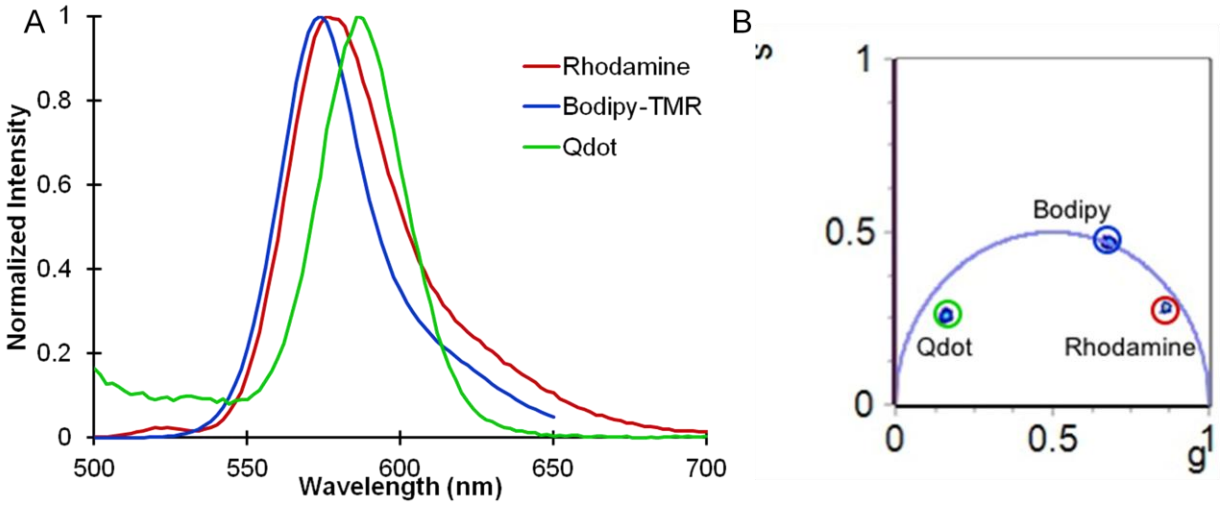

Figure 5.1 Spectroscopic and lifetime characteristics of 3 probe fluorescent panel. Rhodamine, Bodipy-TMR, and QDot585 fluorescent probes in aqueous solution emit within the same spectral window, 575-610 nm, (A), but display unique fluorescence lifetimes whose values can be easily separated on the phasor plot (B). Laser frequency is 20 MHz.

The binding kinetics of quantum dot immunoconjugates were studied to determine the optimal labeling concentration for FLIM studies. This is especially relevant for antibody-nanoparticle conjugates, since the bioconjugation of antibodies to nanoparticles

is frequently plagued with low efficiencies.[84] The use of bioorthogonal chemistries created efficiently labeled quantum dot immunoconjugates, illustrated by their saturate binding at less than 30 nM (Figure 5.2), which resembles the binding kinetics of the antibody alone. For future FLIM studies, quantum dot immunoconjugates were used at 30 nM. Fluorophore-modified antibodies also displayed kinetics similar to the antibody alone, which is expected since previous work suggests that low-level modifications of fluorophores to antibodies do not significantly disrupt binding kinetics. Consequently, fluorophore-antibody conjugates were used at 10 μg/ml for FLIM studies.

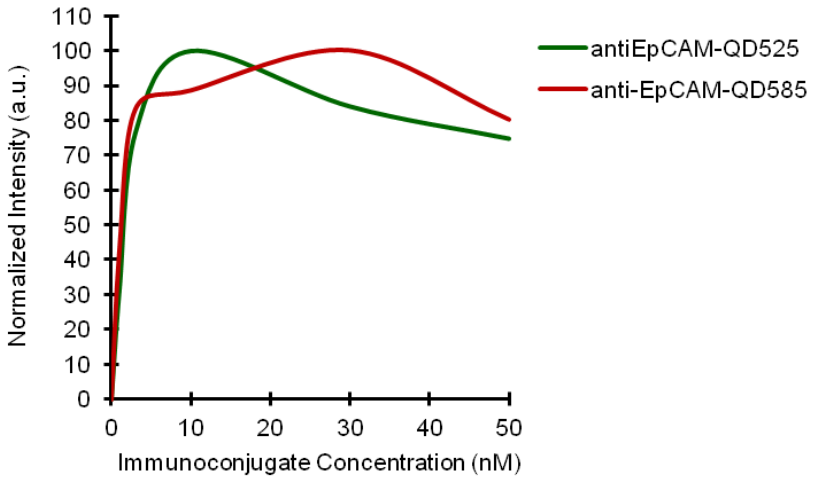

Figure 5.2 Kinetic analysis of antibody-quantum dot immunoconjugates. TCO-modified antiEpCAM antibodies coupled to tetrazine-modified quantum dots yielded efficient quantum dot immunoconjugates that display good binding kinetics, demonstrated by saturating signal at 10-30 nM

Once optimal labeling concentrations for each probe were obtained, we sought to establish spatially-resolved multi-target fluorescence imaging with our time-resolved three probe panel. In these experiments, we used antiEpCAM-QD585 immunoconjugates to target the surface membrane of cells, anti-Ki67-Rhodmine conjugate to target nuclear Ki67, and pan-cytokeratin antibody modified with Bodipy-TMR to target cytokeratin within the intracellular space. Prior to simultaneous labeling, we targeted probes individually to

cells. This single-target labeling served two goals. First, it is necessary to identify the phasor location of the fluorescent probes when conjugated to antibodies. Fluorescent probes are prone to quenching when conjugated to biomolecules,[69] and consequentially may exhibit altered lifetime characteristics after antibody conjugation. Moreover, the degree of quenching depends of the specific antibody used. Secondly, the cellular environment of the antibody-conjugate may also influence lifetime properties, such as when conjugates accumulate in endosomes. (Chapter 4) To mitigate the effects of nanoparticle internalization, such as altered fluorescence lifetime, surface markers were stained on live cells over ice. Thus, to observe the phasor location of each antibody conjugate, we labeled each probe separately. (Figure 5.3) Importantly, antibody conjugates specifically labeled their target marker. While the fluorescent probes exhibited lifetimes that closely match the solution-based measurements, indicating that lifetime-based resolution is still feasible, subtle shifts in phasor location of each probe were noted. Consequently, we utilized the phasor locations from cells individually labeled with each probe to identify the phasor in future analysis.

Next, we performed FLIM imaging with two of the three fluorescent probes to illustrate how spatially-separated probes could be simply resolved. Cells simultaneously targeted for EpCAM and Ki67 produced a unique phasor map (Figure 5.4B) Since probes are separated in space, the majority of pixels have a lifetime value of either the antiEpCAM-quantum dot probe or antiKi67-Rhodamine probe, with a minimal number of pixels that contain some contribution of both. Leveraging the linear properties of the phasor plot, we can generate a map depicting the relative fractional contribution of each probe (Figure 5.4D), and can then paint the image according to this map (Figure 5.4C). Utilizing the

fractional amount of both probes at each pixel, we can separate total intensity for each probe. (Figure 5.4E-F) The precise discrimination of intensity based on lifetime is apparent.

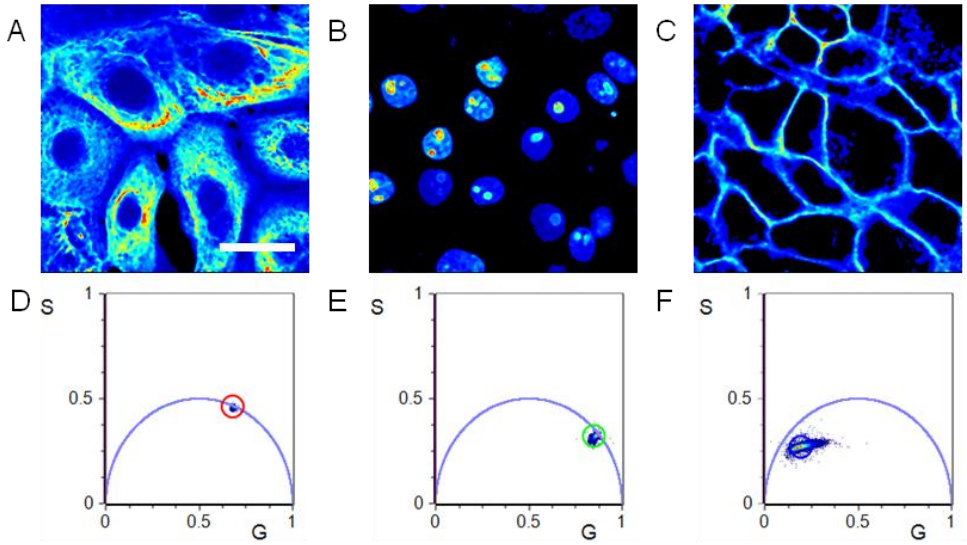

Figure 5.3 Fluorescence intensity and lifetime of individually-targeted probes. Intensity heat maps of NCI-H1650 cells labeled with anti-Cytokeratin-Bodipy TMR (A), anti-Ki67-Rhodamine (B), and anti-EpCAM-QD585 (C), and the corresponding phasor maps (D-F). Scale bar, 20 µm. Laser frequency is 20 MHz.

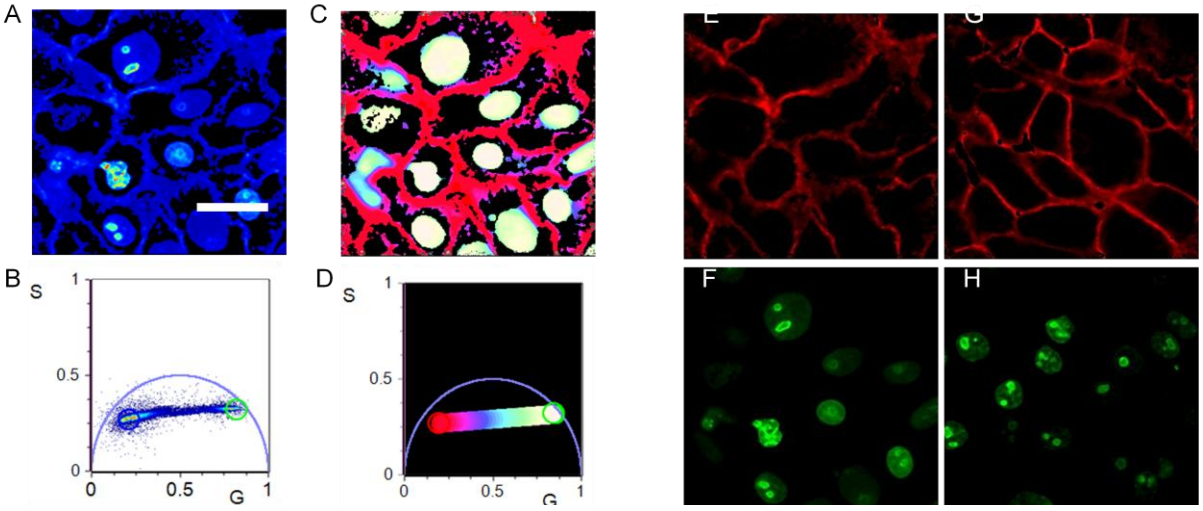

Figure 5.4 Simultaneous multi-target imaging of EpCAM and Ki67. Total intensity heat map of NCI-H1650 cells labeled with antiEpCAM-QDot585 immunoconjugate and antiKi67-Rhodamine (A) and corresponding phasor (B). FLIM image painted according to fractional contribution of both probes (C), where the line corresponds to 100% fractional contribution from QD585 immunoconjugate (red), 100% fractional contribution from Rhodamine-antibody conjugate (white) and all possible combinations fall in-between (D). Intensity images of labeled EpCAM (E) and Ki67 (F) extracted from total intensity (A) based on lifetime properties., closely match intensity images of EpCAM (G) and Ki67 (H) when targeted individually. Scale bar, 20 µm. Laser frequency is 20 MHz.

For increasingly complex analysis, we performed two-component targeting, labeling Ki67 and cytokeratin (Figure 5.5) or EpCAM and cytokeratin (Figure 5.6) in parallel. While these dual targets are still somewhat separated in space, they contain overlapping regions; therefore, numerous pixels include both fluorescent species and require unmixing. Additionally, Rhodamine and Bodipy-TMR have lifetime values that are closer in phasor space. The concurrent targeting, as is the case for labeling Ki67 and cytokeratin, could potentially be challenging for separation of mixtures. In total intensity images from both dual targeting scenarios (Figure 5.5A and Figure 5.6A), it is difficult to distinguish specific features from either target. However, mapping the FLIM image according to fractional distribution (Figure 5.5B and 5.6B) clearly depicts the correct spatial localization for each probe, and this information is used to segregate intensity contribution from each probe to reconstruct cytokeratin and Ki67 stain (Figure 5.5E and 5.5F) or cytokeratin and cell surface EpCAM stain (Figure 5.6E and Figure 5.6F).

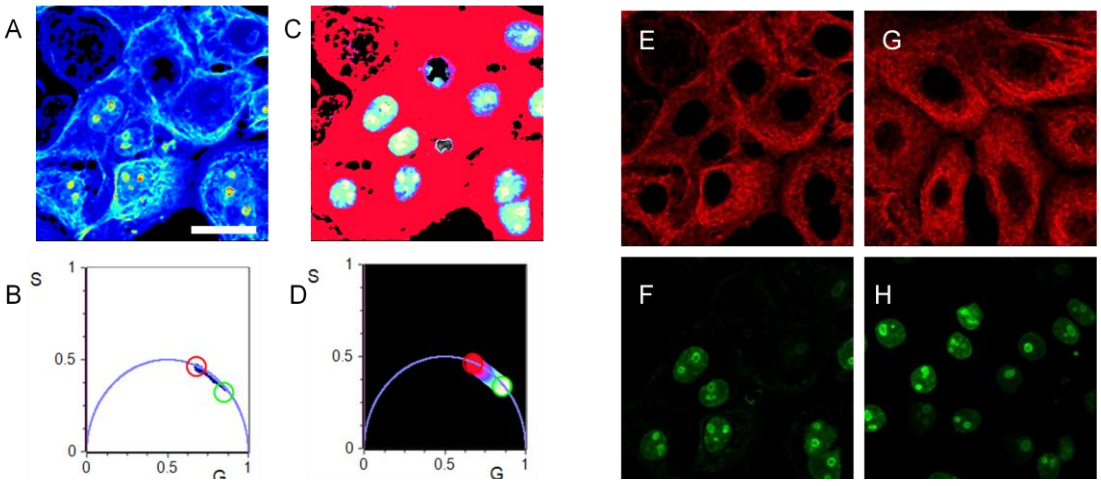

Figure 5.5 Simultaneous multi-target imaging of Cytokeratin and Ki67. Total intensity heat map of NCI-H1650 cells labeled with antiCytokeratin-BodipyTMR and antiKi67-Rhodamine (A) and phasor (B). FLIM image painted according to fractional contribution of both probes (C), where the line corresponds to 100% fractional contribution from BodipyTMR-antibody conjugate (red), 100% fractional contribution from Rhodamine-antibody conjugate (white) and all possible combinations fall in-between (D). Intensity images of labeled Cytokeratin (E) and Ki67 (F) extracted from total intensity (A) based on lifetime properties, closely match intensity images of Cytokeratin (G) and Ki67 (H) when targeted individually.

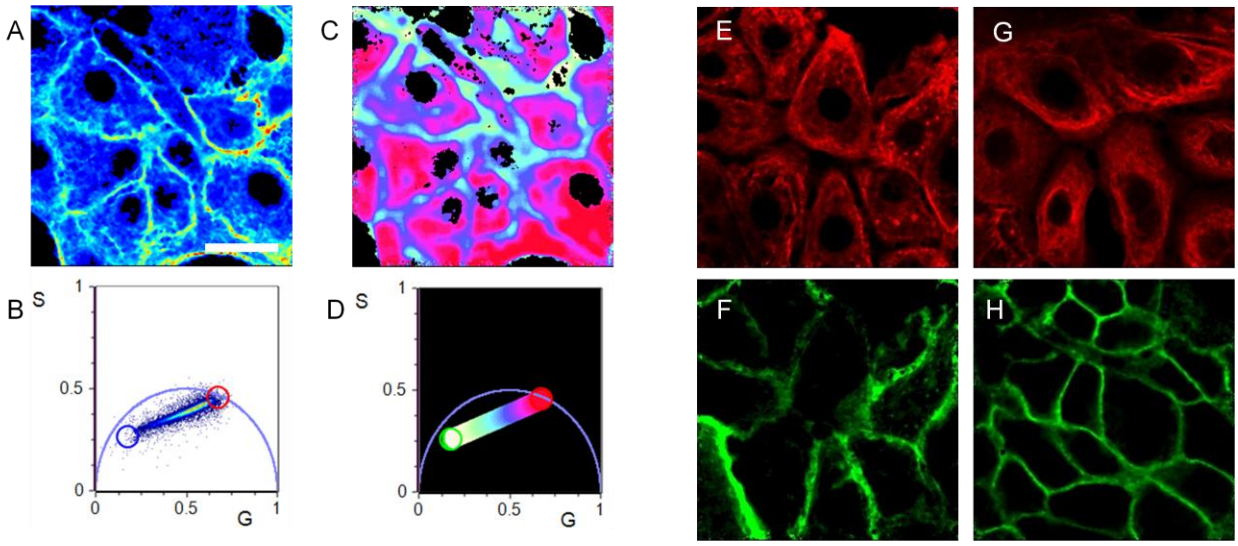

Figure 5.6 Simultaneous multi-target imaging of Cytokeratin and EpCAM. Total intensity heat map of NCI-H1650 cells labeled with antiCytokeratin-BodipyTMR and antiEpCAM-QD585 immunoconjugate (A) and corresponding phasor (B). FLIM image painted according to fractional contribution of both probes (C), where the line corresponds to 100% fractional contribution from BodipyTMR-antibody conjugate (red), 100% fractional contribution from QD585 immunoconjugate (white) and all possible combinations fall in-between (D). Intensity images of labeled Cytokeratin (E) and EpCAM (F) extracted from total intensity (A) based on lifetime properties, closely match intensity images of Cytokeratin (G) and EpCAM (H) when targeted individually. Scale bar, 20 μm. Laser frequency is 20 MHz.

We then performed three probe multi-target imaging. In the intensity heat map of triple-labeled cells (Figure 5.7A), it is difficult to discern specific cellular features. Painting this image according to the relative fractional amount of each probe clearly reconstructs the subcellular regions where each probe is localized. (Figure 5.7C) The extracted intensity images (Figure 5.7E-G) reveal the cellular structures targeted, capturing the features obtained with single-stain images (Figures 5.7 H-J).

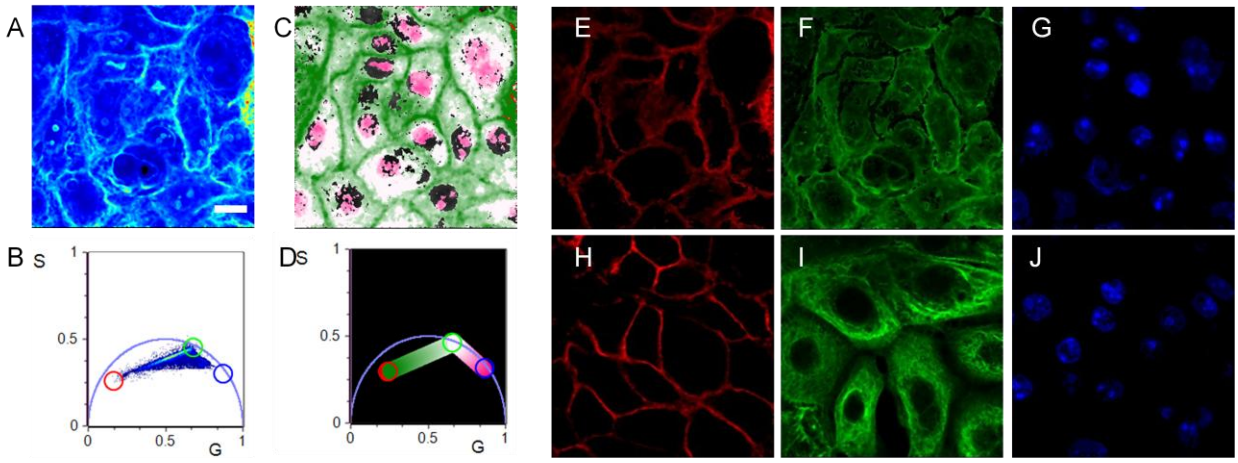

Figure 5.7 Simultaneous multi-target imaging of Cytokeratin , Ki67, and EpCAM. Total intensity heat map of NCI-H1650 cells labeled with antiCytokeratin-BodipyTMR, antiKi67-Rhodamine, antiEpCAM-QD585 immunoconjugate (A) and corresponding phasor (B). FLIM image painted according to fractional contribution of three probes (C, D) Intensity images of labeled EpCAM (E) Cytokeratin (F), and Ki67(G) extracted from total intensity (A) based on lifetime properties, closely match intensity images of EpCAM (H), Cytokeratin (I), and Ki67 (J) when targeted individually. Scale bar, 20 μm. Laser frequency is 20 MHz.

To illustrate the multidimensionality of this approach, we performed the same multi-target imaging utilizing probes that emit in the green spectral window. Oregon-Green 488, Bodipy-FL, and QD525 fluorescent probes were used to label Ki67, cytokeratin, and EpCAM, respectively. Once again, phasor locations were first ascertained by labeling antibody-conjugates to cells individually (Figure 5.8), followed by labeling cells with all three targets in parallel. The successful identification of each fluorescent signal (Figure 5.9) highlights this technique's capacity to resolve numerous probes within each spectral window.

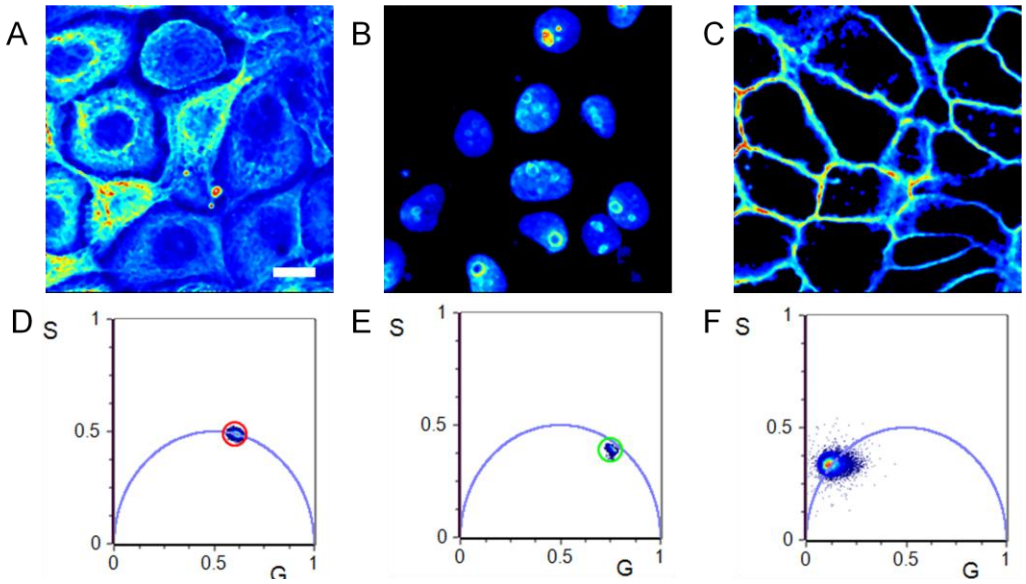

Figure 5.8 Fluorescence intensity and lifetime of individually-targeted probes. Intensity heat maps of NCI-H1650 cells labeled with anti-Cytokeratin-Bodipy FL (A), anti-Ki67-Oregon Green (B), and anti-EpCAM-QD525 (C), and the corresponding phasor maps (D-F). Scale bar, 20 µm. Laser frequency is 20 MHz.

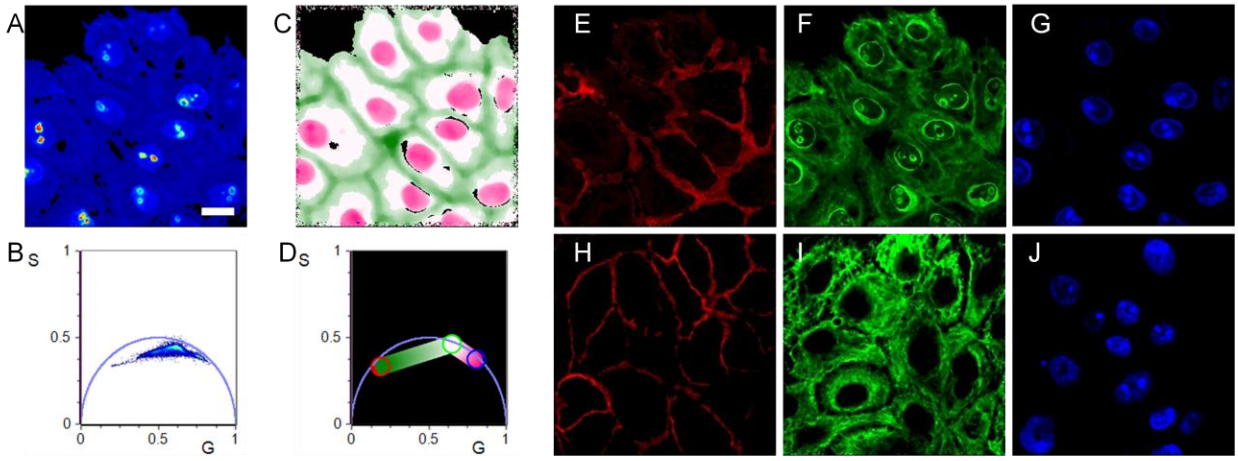

Figure 5.9 Simultaneous multi-target imaging of Cytokeratin , Ki67, and EpCAM in green emission window. Total intensity heat map of NCI-H1650 cells labeled with antiCytokeratin-BodipyFL, antiKi67-Oregon Green 488, antiEpCAM-QD525 immunoconjugate (A) and corresponding phasor (B). FLIM image painted according to fractional contribution of three probes (C, D) Intensity images of labeled EpCAM (E) Cytokeratin (F), and Ki67(G) extracted from total intensity (A) based on lifetime properties, closely match intensity images of EpCAM (H), Cytokeratin (I), and Ki67 (J) when targeted individually. Scale bar, 20 µm. Laser frequency is 20 MHz.

The spatial discrimination achieved by targeting different subcellular regions facilitated resolution of three probes simultaneously. However, to demonstrate the power of the phasor approach, we performed multi-targeted imaging with three surface markers. We used the following three probes: antiEpCAM-QD585 immunoconjugate, antiTfR-Rhodamine antibody conjugate, and antiE-Cadherin-Bodipy TMR (Figure 5.10).

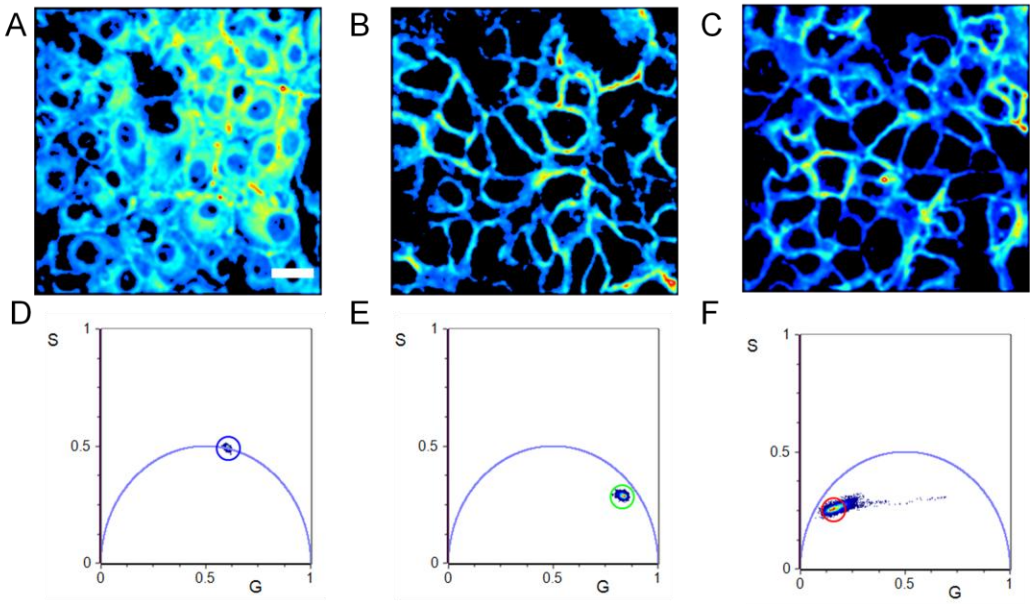

Figure 5.10 Fluorescence intensity and lifetime of individually-targeted surface marker probes. Intensity heat maps of NCI-H1650 cells labeled with anti-E-Cadherin-Bodipy TMR (A), anti-TfR-Rhodamine(B), and anti-EpCAM-QD585 (C), and the corresponding phasor maps (D-F). Scale bar, 40 µm. Laser frequency is 20 MHz.

These surface markers were chosen based on their relevancy in identifying tumor populations; however this approach could generally be applied to identity cell subtypes based on surface marker expression. First, cells were labeled in combinations of two. (Figure 5.11A-F) Since all targets are localized to the same cellular region, most pixels in the dual-targeted image contain some amount of both probes. Consequently, the entire phasor cluster falls along the line joining the lifetime of the two individual probes. The phasor cluster moved within phasor space depending on the two probes used. Targeting all

three surface markers simultaneously resulted in a phasor cluster located within the triangle whose vertices are the lifetime locations of each probe. Notably, this phasor was distinct from the phasors obtained with any combination of two probes. Thus, the phasor approach would be a straightforward visual tool to identify the presence or absence of several surface markers. Moreover, the extracted intensity obtained for each surface marker was similar to the intensity acquired from single stains. We did calculate high false positive signal of rhodamine when cells were only labeled for E-Cadherin using a Bodipy-TMR probe. This error can be attributed to the close proximity of the lifetime clusters for rhodamine and Bodipy-TMR, and the relative brightness of both probes. To address this error, phasor plots calculated at the second harmonic of the laser repetition rate can be used, which would provide better discrimination between short lifetime species.

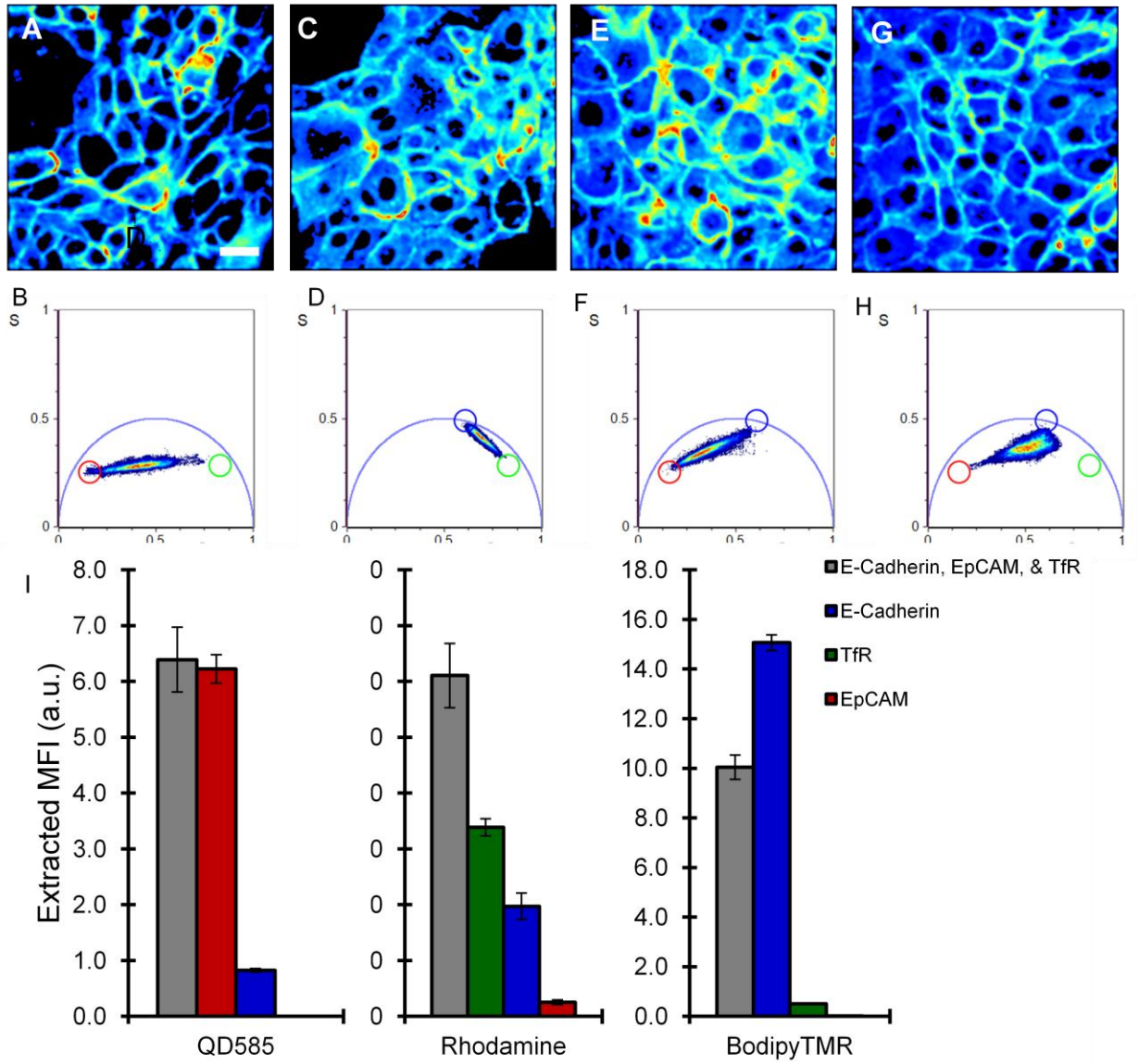

Figure 5.11 Simultaneous multi-target imaging of three surface markers. Total intensity heat map of NCI-H1650 cells labeled for EpCAM and TfR (A), E-Cadherin and TfR (C), E-Cadherin and EpCAM (E), or all three (G), and corresponding phasor plots (B,D,F,H). Mean extracted intensity of each probe from multi-target image (gray) compared to extracted intensity of each probe from single-stain images (I) Scale bar, 40 µm. Laser frequency is 20 MHz.

5.4 Discussion

In this work, we reported a technique for highly multiplexed fluorescence imaging. The phasor approach to FLIM dimensionally increases the number of probes that can be resolved simultaneously. By incorporating quantum dots, that display long fluorescence lifetimes, three spectrally-similar fluorescent species could easily be resolved. Fluorescence lifetime of quantum dots are tunable, thus it is feasible to generate even more probes that exhibit distinct lifetimes. Additionally, this technique did not rely on spectral content to discern species; however the addition of this information could enable discrimination of even more probes. This technique is likely also compatible with cyclic staining methods for numerous rounds of multi-target imaging. The degree of multiplexing achieved, paired with morphological features, is powerful for characterizing heterogeneous tissues. The reciprocal nature of the phasor approach enables visualization of cells or subcellular regions of the tissue that exhibit unique lifetimes, and thus unique phenotypes. This feature could be exploited to uncover spatial relationships between different cell types. Moreover, this approach requires minimal additional instrumentation, computation, or time compared to conventional fluorescence imaging. Owing to these features, this approach has the power to make highly multiplexed molecular profiling more ubiquitous, and can be coupled with downstream analysis techniques like SPADE or viSNE[159,160] for systems-level pathology to better understand and diagnose disease.

Chapter 6

Conclusions and future directions

The speed and small footprint of bioorthogonal reactions have enabled efficient, multivalent coupling of nanomaterial probes to affinity molecules, which can be exploited for diagnostic and therapeutic potential. These chemistries can also provide signal enhancement in molecular targeting scenarios, permitting the attachment of numerous nanoparticles to an antibody *in situ.* However, we uncovered substantial hydrophobic burying of bioorthogonal reactants when conjugated to antibodies. To unmask bioorthogonal moieties, we employed a two-step dual bioorthogonal modification strategy where antibodies first modified with azide were subsequently coupled to DBCO-PEG-TCO linkers. Introducing TCO in this manner fully preserved its reactivity when conjugated to antibodies, and resulted in greater than 5-fold signal enhancement in molecular targeting. We attempted to restore reactivity in a one-step modification approach, utilizing either PEG or alkyl chain linkers distal to the TCO. While neither approach enabled full reactivity of total modifications, reactivity was drastically improved to 70%, depending on length of linker. Interestingly, the two-step dual bioorthogonal method did not depend on linker length; both short and long PEG chains preserved reactivity equally well. It is unclear how the different components of the two-step system interplay to unmask bioorthogonal conjugations, but it is evidently complex. Future work will extend successful one-step modification techniques to other bioorthogonal reactants beyond TCO to determine whether gains in reactivity are broadly applicable.

In addition to offering signal enhancement, bioorthogonal pretargeting may also be a useful technique for lessening nanoparticle internalization. Nanoparticle-antibody direct

immunoconjugates are multivalent, and therefore drive internalization when targeted to cells. We uncovered that internalization likely influences quantum dot fluorescence lifetime, potentially from homoquenching. Future work will employ spectral imaging to better characterize internalized fluorescent species and determine if the presence of endogenous fluorescent species is also influencing the unique lifetime. While this phenomenon could be a useful tool to study internalization and clustering dynamics, predictable fluorescence lifetime from quantum dots could also enable lifetime-based multiplexed fluorescence imaging.

Quantum dots display long fluorescence lifetimes, distinct from the much shorter lifetime or organic fluorophores. We have demonstrated that this distinction can be leveraged for multiplexed analysis using the phasor approach to FLIM. We found that with this approach, resolving spatially-separated cellular targets was simple. Additionally, we demonstrated that this technique could be employed for cell subtyping. The graphical analysis of the phasor approach enables straightforward identification of pixels containing two species, which are visually distinguishable from pixels containing three species. Therefore, this feature can enable identification of cells based on multiple surface receptor markers utilizing probes that emit in the same spectral window, and could be extended to different spectral windows for multidimensional multiplexing. In some scenarios, false positive signals were detected, particularly when the lifetime clusters where close in phasor space. We suspect that, when converting signal intensity to absolute concentration, these false positive signals will amount to low concentrations. However, utilizing the phasor generated from the second harmonic of the laser repletion frequency will also help to better resolve probes with similar lifetimes. Future work will also extend multiplexing

capacity to 4 probes in one emission window. Quantum dots with different core, shell, or synthesis properties exhibit distinct lifetimes, which can be leveraged for a fourth probe. Additionally, encapsulating quantum dots in silica shells can serve as both a physical barrier from environmental factors that influence lifetime, as well as an avenue for further lifetime manipulation.

The increased signal sensitivity accomplished with bioorthogonal coupling of nanoparticles paired with the high multiplexing achieved with nanoparticles are together beneficial tools for improved cancer diagnostics, namely examining tumor heterogeneity. Increased signal sensitivity can enable identification of low-level expression markers. Mutually orthogonal bioorthogonal chemistries can be employed in tandem for enhancement of several molecular targets of interest. Moreover, multi-target imaging can be further extended with the use of lifetime-based multiplexing, which enables comprehensive characterization of tumors. These tools can be utilized to study cell-cell interactions and spatial organization for enhanced cancer diagnostics. While this approach can be improved with the addition of hyperspectral content, and does not possess the impressive dynamic range of mass spectrometry techniques; it does not require expensive instrumentation or large time investments relative to current approaches, and is not computationally extensive. As a consequence, sensitive, multiplexed molecular profiling with this approach can become a ubiquitous technique with widespread translation.

References

1. Burrell, R. a, McGranahan, N., Bartek, J. & Swanton, C. The causes and consequences of genetic heterogeneity in cancer evolution. *Nature* **501,** 338–45 (2013).
2. Marusyk, A., Almendro, V. & Polyak, K. Intra-tumour heterogeneity: a looking glass for cancer? *Nat. Rev. Cancer* **12,** 323–34 (2012).
3. Navin, N. *et al.* Inferring tumor progression from genomic heterogeneity. *Genome Res.* **20,** 68–80 (2010).
4. Meacham, C. E. & Morrison, S. J. Tumour heterogeneity and cancer cell plasticity. *Nature* **501,** 328–37 (2013).
5. Shackleton, M., Quintana, E., Fearon, E. R. & Morrison, S. J. Heterogeneity in Cancer: Cancer Stem Cells versus Clonal Evolution. *Cell* **138,** 822–829 (2009).
6. Hanahan, D. & Weinberg, R. a. Hallmarks of cancer: the next generation. *Cell* **144,** 646–74 (2011).
7. Bedard, P. L., Hansen, A. R., Ratain, M. J. & Siu, L. L. Tumour heterogeneity in the clinic. *Nature* **501,** 355–64 (2013).
8. Cohen, R. L. & Settleman, J. From Cancer Genomics to Precision Oncology—Tissue's Still an Issue. *Cell* **157,** 1509–1514 (2014).
9. McGranahan, N. & Swanton, C. Clonal Heterogeneity and Tumor Evolution: Past, Present, and the Future. *Cell* **168,** 613–628 (2017).
10. Hanahan, D. & Coussens, L. M. Accessories to the crime: functions of cells recruited to the tumor microenvironment. *Cancer Cell* **21,** 309–22 (2012).
11. Wörmann, S. M., Diakopoulos, K. N., Lesina, M. & Algül, H. The immune network in

pancreatic cancer development and progression. *Oncogene* 1–12 (2013). doi:10.1038/onc.2013.257

12. Ruffell, B., Affara, N. I. & Coussens, L. M. Differential macrophage programming in the tumor microenvironment. *Trends Immunol.* **33,** 119–26 (2012).
13. Bissell, M. J. & Radisky, D. Putting tumours in context. *Nat. Rev. Cancer* **1,** 46–54 (2001).
14. Nguyen-Ngoc, K.-V. *et al.* ECM microenvironment regulates collective migration and local dissemination in normal and malignant mammary epithelium. *Proc. Natl. Acad. Sci. U. S. A.* **109,** E2595-604 (2012).
15. Junttila, M. R. & de Sauvage, F. J. Influence of tumour micro-environment heterogeneity on therapeutic response. *Nature* **501,** 346–54 (2013).
16. Slamon, D. J. *et al.* Use of chemotherapy plus a monoclonal antibody against HER2 for metastaic breast cancer that overexpresses HER2. *N. Engl. J. Med.* **344,** 783–792 (2001).
17. Mok, T. S. *et al.* Gefitinib or Carboplatin-Paclitaxel in Pulmonary Adenocarcinoma. *N. Engl. J. Med.* **361,** 947–957 (2009).
18. Karapetis, C. S. *et al.* K-ras mutations and benefit from Cetuximab in advanced colorectal cancer. *N. Engl. J. Med.* **359,** 1757–1765 (2008).
19. Chapman, P. B. *et al.* Improved survival with vemurafenib in melanoma with BRAF V600E mutation. *N. Engl. J. Med.* **364,** 2507–16 (2011).
20. Sorlie, T. *et al.* Gene expression patterns of breast carcinomas distinguish tumor subclasses with clinical implications. *Proc. Natl. Acad. Sci. U. S. A.* **98,** 10869–10874 (2001).

21. Maley, C. C. *et al.* Genetic clonal diversity predicts progression to esophageal adenocarcinoma. *Nat. Genet.* **38,** 468–73 (2006).

22. Park, S. Y. *et al.* Heterogeneity for stem cell-related markers according to tumor subtype and histologic stage in breast cancer. *Clin. Cancer Res.* **16,** 876–887 (2010).

23. Ignatiadis, M. & Sotiriou, C. Understanding the molecular basis of histologic grade. *Pathobiology* **75,** 104–111 (2008).

24. Zrazhevskiy, P., True, L. D. & Gao, X. Multicolor multicycle molecular profiling with quantum dots for single-cell analysis. *Nat. Protoc.* **8,** 1852–69 (2013).

25. Russo, G., Zegar, C. & Giordano, A. Advantages and limitations of microarray technology in human cancer. *Oncogene* **22,** 6497–507 (2003).

26. van 't Veer, L. J. *et al.* Gene expression profiling predicts clinical outcome of breast cancer. *Nature* **415,** 530–536 (2002).

27. Wang, Y. *et al.* Gene-expression profiles to predict distant metastasis of lymph-node-negative primary breast cancer. *Lancet* **365,** 671–679 (2005).

28. Garber, M. E. *et al.* Diversity of gene expression in adenocarcinoma of the lung. *Proc. Natl. Acad. Sci. U. S. A.* **98,** 13784–13789 (2001).

29. Eschrich, S. *et al.* Molecular staging for survival prediction of colorectal cancer patients. *J. Clin. Oncol.* **23,** 3526–3535 (2005).

30. Leary, R. J. *et al.* Development of personalized tumor biomarkers using massively paparallel sequencing. *Sci Transl Med.* **2,** 1–15 (2010).

31. Monzon, F. A. *et al.* Multicenter validation of a 1,550-gene expression profile for identification of tumor tissue of origin. *J. Clin. Oncol.* **27,** 2503–2508 (2009).

32. Ley, T. J., Miller, C. & Li, D. Genomic and Epigenomic Landscapes of Adult De Novo

Acute Myeloid Leukemia The Cancer Genome Atlas Research Network. *N. Engl. J. Med.* **368,** 2059–74 (2013).

33. Hoadley, K. A. *et al.* Multiplatform analysis of 12 cancer types reveals molecular classification within and across tissues of origin. *Cell* **158,** 929–944 (2014).
34. Tang, F. *et al.* mRNA-Seq whole-transcriptome analysis of a single cell. *Nat. Methods* **6,** 377–382 (2009).
35. Ramskold, D. *et al.* Full-length mRNA-Seq from single cell levels of RNA and individual CTCs. *Nat. Biotechnol.* **30,** 777–782 (2012).
36. Picelli, S. *et al.* Full-length RNA-seq from single cells using Smart-seq2. *Nat. Protoc.* **9,** 171–81 (2014).
37. Macosko, E. Z. *et al.* Highly parallel genome-wide expression profiling of individual cells using nanoliter droplets. *Cell* **161,** 1202–1214 (2015).
38. Gawad, C., Koh, W. & Quake, S. R. Single-cell genome sequencing: current state of the science. *Nat. Rev. Genet.* **17,** 175–188 (2016).
39. Dalerba, P. *et al.* Single-cell dissection of transcriptional heterogeneity in human colon tumors. *Nat. Biotechnol.* **29,** 1120–1127 (2011).
40. Giesen, C. *et al.* Highly multiplexed imaging of tumor tissues with subcellular resolution by mass cytometry. *Nat. Methods* **11,** 417–22 (2014).
41. Tirosh, I. *et al.* Dissecting the multicellular ecosystem of metastatic melanoma by single-cell RNA-seq. *Science (80-.).* **352,** 189–196 (2016).
42. Patel, A. P. *et al.* Single-cell RNA-seq highlights intratumoral heterogeneity in primary glioblastoma. *Science (80-.).* **344,** 1396–1401 (2014).
43. Lawson, D. A. *et al.* Single-cell analysis reveals a stem-cell program in human

metastatic breast cancer cells. *Nature* **526,** 131–5 (2015).

44. Bodenmiller, B. Multiplexed Epitope-Based Tissue Imaging for Discovery and Healthcare Applications. *Cell Syst.* **2,** 225–238 (2016).

45. Beck, A. H., Sangoi, A. R., Leung, S., Marinelli, R. J. & Nielsen, T. O. Systematic Analysis of Breast Cancer Morphology Uncovers Stromal Features Associated with Survival. *Sci. Transl. Med.* **113,** 108ra113 (2011).

46. Jones, T. R. *et al.* CellProfiler Analyst: data exploration and analysis software for complex image-based screens. *BMC Bioinformatics* **9,** (2008).

47. Irish, Jonathan M; Kotecha, Nikesh; Nolan, G. P. Mapping normal and cancer cell signaling networks: towards single-cell proteomics. *Nat. Rev. Cancer* **6,** 146–155 (2006).

48. Lichtman, J. W. & Conchello, J. Fluorescence microscopy. **2,** 1–60 (2009).

49. Weissleder, R. & Pittet, M. J. Imaging in the era of molecular oncology. *Nature* **452,** 580–9 (2008).

50. Resch-Genger, U., Grabolle, M., Cavaliere-Jaricot, S., Nitschke, R. & Nann, T. Quantum dots versus organic dyes as fluorescent labels. *Nat. Methods* **5,** 763–775 (2008).

51. Liu, J. *et al.* Molecular Mapping of Tumor Heterogeneity on Clinical Tissue Dots. *ASC Nano* **4,** 2755–2765 (2010).

52. Lu, G. & Fei, B. Medical hyperspectral imaging: a review. *J. Biomed. Opt.* **19,** 10901 (2014).

53. Lin, J.-R., Fallahi-Sichani, M. & Sorger, P. K. Highly multiplexed imaging of single cells using a high-throughput cyclic immunofluorescence method. *Nat. Commun.* **6,** 8390 (2015).

54. Chen, K. H., Boettiger, A. N., Moffitt, J. R., Wang, S. & Zhuang, X. RNA imaging. Spatially resolved, highly multiplexed RNA profiling in single cells. *Science* **348,** aaa6090 (2015).

55. Angelo, M. *et al.* Multiplexed ion beam imaging of human breast tumors. *Nat. Med.* **20,** 436–42 (2014).

56. Elson, D. S., Marcu, L. & French, P. M. W. Overview of fluorescence lifetime imaging and metrology. (2006).

57. Lakowicz, J. R., Jayaweera, R., Szmacinski, H. & Wiczk, W. Resolution of multicomponent fluorescence emission using frequency-dependent phase angle and modulation spectra. *Anal. Chem.* **62,** 2005–2012 (1990).

58. Grabolle, M. *et al.* Fluorescence lifetime multiplexing with nanocrystals and organic labels. *Anal. Chem.* **81,** 7807–7813 (2009).

59. Lakowicz, J. R. Time-Domain Lifetime Measurements. *Princ. Fluoresc. Spectrosc.* **1,** 97–155 (2006).

60. Becker, W. *et al.* Fluorescence Lifetime Imaging by Time-Correlated Single-Photon Counting. *Microsc. Res. Tech.* **63,** 58–66 (2004).

61. Gratton, E. Measurements of fluorescence decay time by the frequency domain method. *Springer Ser. Fluoresc.* (2016). doi:10.1007/4243

62. Lakowicz, J. R. Frequency-Domain Lifetime Measurements. *Princ. Fluoresc. Spectrosc.* 157–204 (2010). doi:10.1016/0925-4005(96)80051-7

63. Colyer, R. A., Lee, C. & Gratton, E. A novel fluorescence lifetime imaging system that optimizes photon efficiency. *Microsc. Res. Tech.* **71,** 201–213 (2008).

64. Grinvald, A. & Steinberg, I. Z. On the analysis of fluorescence decay kinetics by the

method of least-squares. *Anal. Biochem.* **59,** 583–598 (1974).

65. Gafni, A., Modlin, R. L. & Brand, L. Analysis of fluorescence decay curves by means of the Laplace transformation. *Biophys. J.* **15,** 263–80 (1975).

66. Digman, M. a, Caiolfa, V. R., Zamai, M. & Gratton, E. The phasor approach to fluorescence lifetime imaging analysis. *Biophys. J.* **94,** L14–L16 (2008).

67. James, D. R. & Ware, W. R. A fallacy in the interpretation of fluorescence decay parameters. *Chem. Phys. Lett.* **120,** 455–459 (1985).

68. Lee, K. C. *et al.* Application of the stretched exponential function to fluorescence lifetime imaging. *Biophys. J.* **81,** 1265–1274 (2001).

69. Niehörster, T. *et al.* Multi-target spectrally resolved fluorescence lifetime imaging microscopy. *Nat. Methods* **13,** 257–262 (2016).

70. Stringari, C. *et al.* Phasor approach to fluorescence lifetime microscopy distinguishes different metabolic states of germ cells in a live tissue. *Nat Acad Sci Proc* **108,** 13582–13587 (2011).

71. Ma, N., Digman, M. A., Malacrida, L. & Gratton, E. Measurements of absolute concentrations of NADH in cells using the phasor FLIM method. *Biomed. Opt. Express* **7,** 2441–52 (2016).

72. Nothdurft, R., Sarder, P., Bloch, S., Culver, J. & Achilefu, S. Fluorescence lifetime imaging microscopy using near-infrared contrast agents. *J. Microsc.* **247,** 202–7 (2012).

73. Suhling, K. *et al.* Fluorescence lifetime imaging (FLIM): Basic concepts and some recent developments. *Med. Photonics* **27,** 3–40 (2015).

74. Schlegel, G., Bohnenberger, J., Potapova, I. & Mews, A. Fluorescence decay time of

single semiconductor nanocrystals. *Phys. Rev. Lett.* **88,** 137401 (2002).

75. Wu, X. *et al.* Immunofluorescent labeling of cancer marker Her2 and other cellular targets with semiconductor quantum dots. *Nat. Biotechnol.* **21,** 41–46 (2003).

76. Dabbousi, B. O. *et al.* (CdSe)ZnS Core - Shell Quantum Dots : Synthesis and Characterization of a Size Series of Highly Luminescent Nanocrystallites. *J. Phys. Chem. B* **101,** 9463–9475 (1997).

77. Nimmo, M. T. *et al.* Visible to near-infrared sensitization of silicon substrates via energy transfer from proximal nanocrystals: Further insights for hybrid photovoltaics. *ACS Nano* **7,** 3236–3245 (2013).

78. Bruchez Jr., M., Moronne, M., Gin, P., Weiss, S. & Alivisatos, A. P. Semiconductor Nanocrystals as Fluorescent Biological Labels. *Science (80-.).* **281,** 2013–2016 (1998).

79. Gao, X., Cui, Y., Levenson, R. M., Chung, L. W. K. & Nie, S. In vivo cancer targeting and imaging with semiconductor quantum dots. *Nat. Biotechnol.* **22,** 969–976 (2004).

80. Yezhelyev, M. V. *et al.* In situ molecular profiling of breast cancer biomarkers with multicolor quantum dots. *Adv. Mater.* **19,** 3146–3151 (2007).

81. Liu, J., Lau, S. K., Varma, V. A., Kairdolf, B. A. & Nie, S. Multiplexed detection and characterization of rare tumor cells in Hodgkin's lymphoma with multicolor quantum dots. *Anal. Chem* **82,** 6237–6243 (2010).

82. Zrazhevskiy, P. & Gao, X. Quantum dot imaging platform for single-cell molecular profiling. *Nat. Commun.* **4,** 1619 (2013).

83. Algar, W. R. *et al.* The controlled display of biomolecules on nanoparticles: a challenge suited to bioorthogonal chemistry. *Bioconjug. Chem.* **22,** 825–58 (2011).

84. Thorek, D. L. J., Elias, D. R. & Tsourkas, A. Comparative Analysis of Nanoparticle-Antibody Conjugations : Carbodiimide versus Click Chemistry. **8,** 221–229 (2009).

85. Haun, J. B., Devaraj, N. K., Hilderbrand, S. A., Lee, H. & Weissleder, R. Bioorthogonal chemistry amplifies nanoparticle binding and enhances the sensitivity of cell detection. **5,** 660–665 (2010).

86. Haun, J. B. *et al.* Micro-NMR for rapid molecular analysis of human tumor samples. *Sci. Transl. Med.* **3,** 71ra16 (2011).

87. Han, H.-S. *et al.* Development of a bioorthogonal and highly efficient conjugation method for quantum dots using tetrazine-norbornene cycloaddition. *J. Am. Chem. Soc.* **132,** 7838–9 (2010).

88. Devaraj, N. K. & Weissleder, R. Biomedical applications of tetrazine cycloadditions. *Acc. Chem. Res.* **44,** 816–27 (2011).

89. Sletten, E. M. & Bertozzi, C. R. From mechanism to mouse: A tale of two bioorthogonal reactions. *Acc. Chem. Res.* **44,** 666–676 (2011).

90. Seckute, J., Yang, J. & Devaraj, N. K. Rapid oligonucleotide-templated fluorogenic tetrazine ligations. *Nucleic Acids Res.* 1–9 (2013). doi:10.1093/nar/gkt540

91. Selvaraj, R. & Fox, J. M. Trans-Cyclooctene-a stable, voracious dienophile for bioorthogonal labeling. *Curr. Opin. Chem. Biol.* **17,** 753–760 (2013).

92. Rossin, R. & Robillard, M. S. Pretargeted imaging using bioorthogonal chemistry in mice. *Curr. Opin. Chem. Biol.* **21,** 161–169 (2014).

93. Carroll, L., Evans, H. L., Aboagye, E. O. & Spivey, A. C. Bioorthogonal chemistry for pre-targeted molecular imaging--progress and prospects. *Org. Biomol. Chem.* **11,** 5772–81 (2013).

94. Rossin, R. *et al.* In vivo chemistry for pretargeted tumor imaging in live mice. *Angew. Chemie - Int. Ed.* **49,** 3375–3378 (2010).

95. Devaraj, N. K., Thurber, G. M., Keliher, E. J., Marinelli, B. & Weissleder, R. Reactive polymer enables efficient in vivo bioorthogonal chemistry. *Instrumentation* **109,** 4762–4767 (2012).

96. Zeglis, B. M. *et al.* A Pretargeted PET Imaging Strategy Based on Bioorthogonal Diels – Alder Click Chemistry. *J. Nucl. Med.* **54,** 1389–1396 (2013).

97. Emmetiere, F. *et al.* 18F-labeled-bioorthogonal liposomes for in vivo targeting. *Bioconjug. Chem.* **24,** 1784–1789 (2013).

98. Rossin, R., Läppchen, T., Van Den Bosch, S. M., Laforest, R. & Robillard, M. S. Diels–Alder Reaction for Tumor Pretargeting: In Vivo Chemistry Can Boost Tumor Radiation Dose Compared with Directly Labeled Antibody. *J Nucl Med* **54,** 1989–1995 (2013).

99. Rossin, R., Van Duijnhoven, S. M. J., Läppchen, T., Van Den Bosch, S. M. & Robillard, M. S. Trans-cyclooctene tag with improved properties for tumor pretargeting with the Diels-Alder reaction. *Mol. Pharm.* **11,** 3090–3096 (2014).

100. Liong, M. *et al.* Specific pathogen detection using bioorthogonal chemistry and diagnostic magnetic resonance. *Bioconjug. Chem.* **22,** 2390–4 (2011).

101. Chung, H. J. *et al.* Ubiquitous Detection of Gram-Positive Bacteria with Bioorthogonal Magneto fl uorescent Nanoparticles. 8834–8841 (2011).

102. Issadore, D. *et al.* Ultrasensitive clinical enumeration of rare cells ex vivo using a micro-hall detector. *Sci. Transl. Med.* **4,** 141ra92 (2012).

103. Ghazani, A. a, Castro, C. M., Gorbatov, R., Lee, H. & Weissleder, R. Sensitive and direct

detection of circulating tumor cells by multimarker μ-nuclear magnetic resonance. *Neoplasia* **14,** 388–95 (2012).

104. Shao, H. *et al.* Protein typing of circulating microvesicles allows real-time monitoring of glioblastoma therapy. *Nat. Med.* **18,** 1835–40 (2012).
105. Blackman, M. L., Royzen, M. & Fox, J. M. Tetrazine Ligation : Fast Bioconjugation Based on Inverse-Electron-Demand Diels - Alder Reactivity. 13518–13519 (2008).
106. Devaraj, N. K., Upadhyay, R., Haun, J. B., Hilderbrand, S. A. & Weissleder, R. Fast and sensitive pretargeted labeling of cancer cells via tetrazine/trans-cyclooctene cycloaddition. *Angew. Chem. Int. Ed. Engl.* **48,** 7013–7016 (2009).
107. Devaraj, N. K., Weissleder, R. & Hilderbrand, S. a. Tetrazine-based cycloadditions: application to pretargeted live cell imaging. *Bioconjug. Chem.* **19,** 2297–9 (2008).
108. Yang, J., Karver, M. R., Li, W., Sahu, S. & Devaraj, N. K. Metal-catalyzed one-pot synthesis of tetrazines directly from aliphatic nitriles and hydrazine. *Angew. Chem. Int. Ed. Engl.* **51,** 5222–5 (2012).
109. Patterson, D. M., Nazarova, L. A., Xie, B., Kamber, D. N. & Prescher, J. A. Functionalized cyclopropenes as bioorthogonal chemical reporters. *J. Am. Chem. Soc.* **134,** 18638–18643 (2012).
110. Rossin, R. *et al.* Highly reactive trans-cyclooctene tags with improved stability for diels-alder chemistry in living systems. *Bioconjug. Chem.* **24,** 1210–1217 (2013).
111. Yang, J., Liang, Y., Sekut, J., Houk, K. N. & Devaraj, N. K. Synthesis and reactivity comparisons of 1-methyl-3-substituted cyclopropene mini-tags for tetrazine bioothogonal reactions. *Chemistry (Easton).* **20,** 3365–3375 (2014).
112. Chapman, A. P. PEGylated antibodies and antibody fragments for improved therapy:

A review. *Adv. Drug Deliv. Rev.* **54,** 531–545 (2002).

113. Sano, K. *et al.* Short PEG-linkers improve the performance of targeted, activatable monoclonal antibody-indocyanine green optical imaging probes. *Bioconjug. Chem.* **24,** 811–816 (2013).

114. Villaraza, A. J. L., Milenic, D. E. & Brechbiel, M. W. Improved speciation characteristics of PEGylated indocyanine green-labeled panitumumab: Revisiting the solution and spectroscopic properties of a near-infrared emitting anti-HER1 antibody for optical imaging of cancer. *Bioconjug. Chem.* **21,** 2305–2312 (2010).

115. Marshall, D. *et al.* Polyethylene glycol modification of a galactosylated streptavidin clearing agent: effects on immunogenicity and clearance of a biotinylated anti-tumour antibody. *Br. J. Cancer* **73,** 565–72 (1996).

116. Hapuarachchige, S., Zhu, W., Kato, Y. & Artemov, D. Bioorthogonal, two-component delivery systems based on antibody and drug-loaded nanocarriers for enhanced internalization of nanotherapeutics. *Biomaterials* **35,** 2346–2354 (2014).

117. Karver, M. R., Weissleder, R. & Hilderbrand, S. a. Bioorthogonal reaction pairs enable simultaneous, selective, multi-target imaging. *Angew. Chem. Int. Ed. Engl.* **51,** 920–2 (2012).

118. Devaraj, N. K., Hilderbrand, S., Upadhyay, R., Mazitschek, R. & Weissleder, R. Bioorthogonal turn-on probes for imaging small molecules inside living cells. *Angew. Chemie - Int. Ed.* **49,** 2869–2872 (2010).

119. Carlson, J. C. T., Meimetis, L. G., Hilderbrand, S. A. & Weissleder, R. BODIPY-tetrazine derivatives as superbright bioorthogonal turn-on probes. *Angew. Chemie - Int. Ed.* **52,** 6917–6920 (2013).

120. Meimetis, L. G., Carlson, J. C. T., Giedt, R. J., Kohler, R. H. & Weissleder, R. Ultrafluorogenic coumarin-tetrazine probes for real-time biological imaging. *Angew. Chemie - Int. Ed.* **53,** 7531–7534 (2014).

121. Darko, A., Wallace, S., Dmitrenko, O., Machovina, M. M. & Ryan, A. Conformationally Strained trans -cyclooctene with Improved Stability and Excellent Reactivity in Tetrazine Ligation. *Chems Sci* **5,** 3770–3776 (2014).

122. Taylor, M. T., Blackman, M. L., Dmitrenko, O. & Fox, J. M. Design and synthesis of highly reactive dienophiles for the tetrazine-trans-cyclooctene ligation. *J. Am. Chem. Soc.* **133,** 9646–9649 (2011).

123. Nikič, I. *et al.* Minimal tags for rapid dual-color live-cell labeling and super-resolution microscopy. *Angew. Chemie - Int. Ed.* **53,** 2245–2249 (2014).

124. Lang, K. *et al.* Genetically encoded norbornene directs site-specific cellular protein labelling via a rapid bioorthogonal reaction. *Nat. Chem.* **4,** 298–304 (2012).

125. Lang, K. *et al.* Genetic encoding of bicyclononynes and trans-cyclooctenes for site-specific protein labeling in vitro and in live mammalian cells via rapid fluorogenic diels-alder reactions. *J. Am. Chem. Soc.* **134,** 10317–10320 (2012).

126. Hapuarachchige, S., Kato, Y. & Artemov, D. Bioorthogonal two-component drug delivery in HER2(+) breast cancer mouse models. *Sci. Rep.* **6,** 24298 (2016).

127. Peterson, V. M., Castro, C. M., Lee, H. & Weissleder, R. Orthogonal Ampli fi cation of Nanoparticles for Improved Diagnostic Sensing. 3506–3513 (2012).

128. Koo, H. *et al.* Bioorthogonal copper-free click chemistry inVivo for tumor-targeted delivery of nanoparticles. *Angew. Chemie - Int. Ed.* **51,** 11836–11840 (2012).

129. Patterson, D. M., Nazarova, L. A. & Prescher, J. A. Finding the right (bioorthogonal)

chemistry. *ACS Chem. Biol.* **9,** 592–605 (2014).

130. Liang, Y., MacKey, J. L., Lopez, S. A., Liu, F. & Houk, K. N. Control and design of mutual orthogonality in bioorthogonal cycloadditions. *J. Am. Chem. Soc.* **134,** 17904–17907 (2012).

131. Ghose, A. K., Viswanadhan, V. N. & Wendoloski, J. J. Prediction of Hydrophobic (Lipophilic) Properties of Small Organic Molecules Using Fragmental Methods: An Analysis of ALOGP and CLOGP Methods. *J. Phys. Chem. A* **102,** 3762–3772 (1998).

132. Xing, Y. *et al.* Bioconjugated quantum dots for multiplexed and quantitative immunohistochemistry. *Nat. Protoc.* **2,** 1152–65 (2007).

133. Wang, F. & Liu, X. Upconversion multicolor fine-tuning: visible to near-infrared emission from lanthanide-doped NaYF4 nanoparticles. *J. Am. Chem. Soc.* **130,** 5642–3 (2008).

134. Kairdolf, B. A. *et al.* Semiconductor quantum dots for bioimaging and biodiagnostic applications. *Ann Rev Anal Chem* **6,** 143–162 (2013).

135. Peng, C. W. *et al.* Patterns of cancer invasion revealed by QDs-based quantitative multiplexed imaging of tumor microenvironment. *Biomaterials* **32,** 2907–2917 (2011).

136. Fountaine, T. J., Wincovitch, S. M., Geho, D. H., Garfield, S. H. & Pittaluga, S. Multispectral imaging of clinically relevant cellular targets in tonsil and lymphoid tissue using semiconductor quantum dots. *Mod. Pathol.* **193800628,** 1181–1191 (2006).

137. Hemdana, I., Mahdouani, M. & Bourguiga, R. Investigation of the radiative lifetime in core-shell CdSe/ZnS and CdSe/ZnSe quantum dots. *Phys. B Condens. Matter* **407,**

3313–3319 (2012).

138. Zhang, S., Gao, H. & Bao, G. Physical Principles of Nanoparticle Cellular Endocytosis. *ACS Nano* **9,** 8655–8671 (2015).

139. Bhattacharyya, S., Bhattacharya, R., Curley, S., McNiven, M. A. & Mukherjee, P. Nanoconjugation modulates the trafficking and mechanism of antibody induced receptor endocytosis. *Proc Natl Acad Sci U S A* **107,** 14541–14546 (2010).

140. Barroso, M. M. Quantum dots in cell biology. *J. Histochem. Cytochem.* **59,** 237–251 (2011).

141. Kelf, T. a *et al.* Non-specific cellular uptake of surface-functionalized quantum dots. *Nanotechnology* **21,** 285105 (2010).

142. Chou, K. & Dennis, A. F{{}{ö}{}}rster Resonance Energy Transfer between Quantum Dot Donors and Quantum Dot Acceptors. *Sensors* **15,** 13288–13325 (2015).

143. Achermann, M., Jeong, S., Balet, L., Montano, G. A. & Hollingsworth, J. A. Efficient quantum dot-quantum dot and quantum dot-dye energy transfer in biotemplated assemblies. *ACS Nano* **5,** 1761–1768 (2011).

144. The Cancer Genome Atlas Network. Integrated Genomic Analyses of Ovarian Carcinoma. *Nature* **474,** 609–615 (2011).

145. Network, T. C. G. A. R. Comprehensive genomic characterization of squamous cell lung cancers. *Nature* **489,** 519–525 (2014).

146. Verhaak, R. G. W. *et al.* Integrated Genomic Analysis Identifies Clinically Relevant Subtypes of Glioblastoma Characterized by Abnormalities in PDGFRA, IDH1, EGFR, and NF1. *Cancer Cell* **17,** 98–110 (2010).

147. Hashimshony, T., Wagner, F., Sher, N. & Yanai, I. CEL-Seq: Single-Cell RNA-Seq by

Multiplexed Linear Amplification. *Cell Rep.* **2,** 666–673 (2012).

148. Gawad, C., Koh, W. & Quake, S. R. Dissecting the clonal origins of childhood acute lymphoblastic leukemia by single-cell genomics. *Proc. Natl. Acad. Sci. U. S. A.* **111,** 17947–52 (2014).

149. Wang, Y. *et al.* Clonal evolution in breast cancer revealed by single nucleus genome sequencing. *Nature* **512,** 1–15 (2014).

150. Tirosh, I. *et al.* Single-cell RNA-seq supports a developmental hierarchy in human oligodendroglioma. *Nature* **539,** 309–313 (2016).

151. Jones, S. *et al.* Comparative lesion sequencing provides insights into tumor evolution. *Proc. Natl. Acad. Sci. U. S. A.* **105,** 4283–4288 (2008).

152. Zhang, M. *et al.* Intratumoral heterogeneity in a p53 null mouse model of human breast cancer. *Cancer Discov.* **5,** 520–533 (2015).

153. Marusyk, A. *et al.* Non-cell-autonomous driving of tumour growth supports sub-clonal heterogeneity. *Nature* **514,** 54–58 (2015).

154. Calbo, J. *et al.* A Functional Role for Tumor Cell Heterogeneity in a Mouse Model of Small Cell Lung Cancer. *Cancer Cell* **19,** 244–256 (2011).

155. Tabassum, D. P. & Polyak, K. Tumorigenesis: it takes a village. *Nat. Rev. Cancer* 1–11 (2015). doi:10.1038/nrc3971

156. Schapiro, D. *et al.* histoCAT: analysis of cell phenotypes and interactions in multiplex image cytometry data. *Nat. Methods* (2017). doi:10.1038/nmeth.4391

157. Tsurui, H. *et al.* Seven-color fluorescence imaging of tissue samples based on Fourier spectroscopy and singular value decomposition. *J. Histochem. Cytochem.* **48,** 653–662 (2000).

158. Hanley, Q. S. Spectrally resolved fluorescent lifetime imaging. *J. R. Soc. Interface* **6,** S83–S92 (2009).

159. Qiu, P. *et al.* Extracting a cellular hierarchy from high-dimensional cytometry data with SPADE. *Nat. Biotechnol.* **29,** 886–891 (2011).

160. Amir, E. D. *et al.* viSNE enables visualization of high dimensional single-cell data and reveals phenotypic heterogeneity of leukemia. *Nat. Biotechnol.* **31,** 545–552 (2013).